

Production of exotic, short lived carbon isotopes in ISOL-type facilities.

Inauguraldissertation
der Philosophisch-naturwissenschaftlichen Fakultät
der Universität Bern

vorgelegt von

Hanna Frånberg

von Frösön, Schweden

Leiter der Arbeit:

Prof. Dr. Heinz W. Gäggeler

Departement für Chemie und Biochemie

CERN-THESIS-2008-084
27/10/2008



Production of exotic, short lived carbon isotopes in ISOL-type facilities.

Inauguraldissertation
der Philosophisch-naturwissenschaftlichen Fakultät
der Universität Bern

vorgelegt von

Hanna Frånberg

von Frösön, Schweden

Leiter der Arbeit:

Prof. Dr. Heinz W. Gäggeler

Departement für Chemie und Biochemie

Von der Philosophisch-naturwissenschaftlichen Fakultät angenommen.

Bern, 27.10.2008

Der Dekan
Prof. Dr. Urs Feller

Abstract

The beam intensities of short-lived carbon isotopes at Isotope Separation On-Line (ISOL) facilities have been limited in the past for technical reasons. The production of radioactive ion beams of carbon isotopes is currently of high interest for fundamental nuclear physics research. To produce radioactive ions a target station consisting of a target in a container connected to an ion source via a transfer line is commonly used. The target is heated to vaporize the product for transport. Carbon in elementary form is a very reactive element and react strongly with hot metal surfaces. Due to the strong chemisorption interaction, in the target and ion source unit, the atoms undergo significant retention on their way from the target to the ion source. Due to this the short lived isotopes decays and are lost leading to low ion yields. A first approach to tackle these limitations consists of incorporating the carbon atoms into less reactive molecules and to use materials for the target housing and the transfer line that only weakly interact with these molecules. Therefore, the adsorption properties of carbon monoxide (CO) and carbon dioxide (CO₂) on a range of materials of interest were investigated in thermochromatography experiments at PSI (Switzerland) by using the carbon isotope ¹¹C. The adsorption enthalpy was retrieved for several materials. A second approach consists of the optimization of target materials and structure, both for the effusion and diffusion of the nuclides of interest. Corresponding on-line experiments were performed at GANIL (France). For the production, diffusion and ionization efficiencies out of different target materials on-line and off-line experiments with carbon and nitrogen isotopes were performed at ISOLDE (CERN). The work performed within this thesis shows that the use of a coated transfer line, fibre felt targets and an electron cyclotron resonance (ECR) ion source would strongly decrease the losses, and provide the experiments with up to 1000 times higher beam currents than today.

Zusammenfassung

Die Intensität von Strahlen von kurzlebigen Kohlenstoffisotopen, wie sie an einer Isotope Separation On-line (ISOL) Facility gewonnen werden können, war in der Vergangenheit durch technische Randbedingung stark begrenzt. Die Produktion von intensiveren radioaktiven Kohlenstoff-Strahlen ist von grossem Interesse in der nuklear physikalischen Grundlagenforschung. Der typische Aufbau zur Produktion solcher Strahlen beinhaltet ein Feststofftarget in einem Containment, das über ein Transferrohr mit einer Ionenquelle verbunden ist. Das Target selbst wird geheizt, um die Produktnuklide auszutreiben und in gasförmiger Form zur Ionenquelle zu transportieren. Kohlenstoff in elementarer Form ist chemisch sehr reaktiv und interagiert sehr stark mit heissen Metalloberflächen. Dies führt zu substantieller Retention auf dem Weg vom Target zur Ionenquelle, sodass kurzlebige Nuklide auf dem Weg dorthin zerfallen oder nur mit sehr geringem Yield in der Ionenquelle ankommen. Ein erster Ansatz zur Lösung dieser Problematik besteht darin, elementaren Kohlenstoff in weniger reaktive Moleküle einzubinden und andererseits im Target-Containment und im Transportrohr Materialien zu verwenden, auf denen diese Moleküle nur schwache Wechselwirkungen eingehen. Im Rahmen dieser Arbeit wurden deshalb die Adsorptionseigenschaften von Kohlenmonoxid (CO) und Kohlendioxid (CO₂) mittels Thermochromatographie unter Nutzung des Kohlenstoff-Isotopes ¹¹C am Paul Scherrer Institut untersucht. Die Adsorptionseenthalpie von CO und CO₂ wurde auf verschiedenen Materialien bestimmt, die für das Target-Containment und das Transportrohr in Frage kommen. Ein zweiter Ansatzpunkt besteht in der Optimierung von Zusammensetzung und Struktur des Targetmaterials, das die Effusion der Nuklide beeinflusst. Entsprechende Experimente wurden an GANIL (Frankreich) durchgeführt. Weitere Experimente zur Produktion, Diffusion und Ionisationseffizienz aus verschiedenen Targetmaterialien mit Kohlenstoff- und Stickstoffisotopen wurden an ISOLDE (CERN) durchgeführt. Die durchgeführten Arbeiten zeigen, dass durch das Verwenden des Targetmaterials in Form eines feinstrukturierten Filzes, einer Beschichtung des Transferrohrs mit einem auf das Molekül abgestimmten Material und der Verwendung einer Zyklotron Resonanz Ionenquelle die Verluste massiv beschränkt werden können. Dies erlaubt die Produktion von Kohlenstoff-Strahlen mit um Grössenordnungen höheren Intensitäten als bisher erreicht.

Acknowledgments

First of all I would like to thank **Prof. Heinz W. Gäggeler** for accepting me as a doctoral student in his group. **Markus Ammann** for supervising me and introducing me to the surface chemistry. Both of them to show me the beauty of randonee skiing in the Swiss mountains. **Robert and Bernt Eichler** for the discussions during the analysis of the chromatography experiments I also would like to thank **Prof. Silvio Decurtins** who accepted to be the examiner for my thesis.

Ulli Köster for introducing me to the work of ISOLDE as a summer student in 2002 and then accepting to supervise and encourage me during these five years of research. For his never ending pushing me to perform better and better and to do another measurement even though the sometimes late hours and long days and nights. For sharing his knowledge with me and showing me the beauty of research.

Prof. Göran Nyman at the University of Göteborg for proposing me to send an application to the CERN summer student program and to **Prof. Björn Jonson** for their support. **Mario Birrer, Thorsten Bartels-Rausch, Sascha Vlassenko** and **Olga Vesna** for the nice discussions and support during the time at PSI. All the coworkers at the Laboratory for Radiochemistry and Environmental Chemistry at the Paul Scherrer Institute for nice discussions over coffee. To my colleagues at ISOLDE for assistance during experiments.

Pascal Jardin, Jean-Charles Thomas, Marie-Genevieve Saint-Laurent, Gabriel Gaubert, Cyrille Eleon and many more for the discussions during the experiments and analysis at GANIL.

And **Elisa** who gave me a kicking and smiling support through out the last year. I also would like to express my gratitude to my family for the support and encouragements that you given me through the years.

This work was possible with the financial support from the EU-RTD project TARGISOL (HPRI-CT-2001-50033).

Contents

1	Introduction	1
1.1	Radioactive Ion Beams	1
1.1.1	In-flight separator	2
1.1.2	Isotope Separation On-Line (ISOL) method	2
1.2	The ISOLDE facility	3
1.3	The ISOL target	4
1.4	Carbon and nitrogen	6
1.5	Material selection	7
2	Thermochromatography experiments	13
2.1	Introduction	13
2.2	Set-up of the experiment	14
2.2.1	Thermochromatography oven	17
2.2.2	Preparation and handling of chromatographic columns.	18
2.2.3	Detector set-up.	19
2.2.4	Deposition temperatures	19
2.3	Results and discussion	19
2.4	Derivation of adsorption enthalpies	24
2.4.1	Analytical method.	24
2.4.2	Monte Carlo simulations	25
2.4.3	Comparison with available data	26
3	Thermochromatography studies on target unit materials	28
3.1	Target materials	28
3.1.1	MgO	29
3.1.2	CaO	29
3.1.3	ZrO ₂	32
3.1.4	HfO ₂	35
3.2	Transfer line and source coating	37
3.2.1	Low temperature experiments on SiO ₂	38
3.2.2	NO _x and CO _x adsorption on Al ₂ O ₃	39
3.2.3	Discussion for SiO ₂ and Al ₂ O ₃ experiment	40

4	On-line experiments	42
4.1	On-line experiment ISOLDE	43
4.2	Release time measurements	43
4.2.1	Release measurements at ISOLDE	44
4.2.2	Release calculations	46
4.3	Background measurements	47
4.3.1	Results and conclusion	49
4.4	On-Line experiments at GANIL	52
4.5	Experiment	53
4.5.1	Efficiencies	56
4.5.2	Results	56
4.6	Release measured with the GANIL targets	59
4.7	Discussion	60
5	Diffusion measurements	64
	Implantation method	65
5.1	Measurements	65
5.1.1	Results	68
6	Ion sources	70
6.1	1 ⁺ ion sources	71
6.1.1	Surface ionization source	71
6.1.2	Laser Ion Source	72
6.1.3	Plasma ion source	72
6.2	Electron Cyclotron Resonance Ion Source	72
6.3	Off-line experiments with the MiniMono ECR 1 ⁺ ion source.	74
6.3.1	Experiment	74
6.3.1.1	Source behavior	75
6.3.2	Results	75
6.4	Discussion	76
7	Summary and Outlook	78
8	Abbreviations	80
9	Appendix	83
9.1	Appendix Target production	83
9.1.1	Preparation of pressed powder pills	83
9.1.2	Cross-section tables	83
9.1.3	Release figures	84

List of Figures

1.1	The ISOLDE hall	3
1.2	ISOLDE target and ion source unit	4
1.3	Comparison between calculated and experimental yields	7
1.4	The production efficiency compared to the half-live of the carbon isotopes	8
1.5	Vapor pressure of metal oxides	9
1.6	Production cross sections vs. target mass	10
1.7	Comparison between the calculated production from EPAX and S and T theories	11
1.8	Comparison between two models for calculation of the cross section	12
2.1	PROTRAC gas target, converter and gas distribution	16
2.2	Experimental set-up	17
2.3	Temperature distribution in the experiments	18
2.4	The activity in the column over time	20
2.5	Chromatograms for TiO ₂	21
2.6	Decay distribution of the different peaks in the TiO ₂ column	22
2.7	Comparison between simulations and experimental values of the adsorption enthalpies	26
3.1	Chromatograms from the experiments MgO column	30
3.2	Chromatograms from experiments with different starting temperature in MgO columns	31
3.3	Chromatograms from the experiments CaO column	32
3.4	Chromatograms from the experiments CaO column	33
3.5	Activity in the chemical traps during the CaO experiment	33
3.6	Chromatograms from the experiments ZrO ₂ column	34
3.7	Chromatograms from experiments with different starting temperature in HfO ₂ columns	36
3.8	Chromatograms from the experiments HfO ₂ column	37
3.9	Chromatogram from SiO ₂	38
3.10	Chromatogram from Al ₂ O ₃ experiments	39
3.11	Temperature dependent retention times of carbon molecules on different metal oxides.	41
4.1	Release curve of ⁶ He	44
4.2	Release curve for ¹⁰ CO	45
4.3	Release curve for ¹¹ CO	46

4.4	Release measurements off-line and on-line by implanting a radioactive beam into a stable target	47
4.5	RaBIT implantations	48
4.6	GANIL release measurement method	48
4.7	$^{18}\text{N}^{14}\text{N}$ α -decay spectrum	49
4.8	Comparison between calculated and experimental yields from a MgO target . .	50
4.9	The accelerators and experimental areas at GANIL.	52
4.10	The standard target container used at GANIL	53
4.11	The GANIL target wheel	53
4.12	The GANIL target and ion source unit	54
4.13	The efficiency of the Ge-detector used at the tape station	57
4.14	The efficiency of the Ge-detector used at the tape station using a stopper plate that reduces the intensity of the beam onto the tape	57
4.15	Gamma spectrum from HfO ₂ target	59
4.16	Gamma-spectrum for ^{17}N from HfO ₂ target at 1500°C after 28 minutes measuring. The 871 keV gamma-line from ^{17}N are fitted	59
4.17	Decay spectrum from ^{15}C	61
4.18	The fitted half-live of ^{16}C with $T_{(1/2)} = 747$ ms, produced, ionized and transported as $^x\text{CO}^+$	62
4.19	Release structure over time from the fibre felt targets	62
4.20	Comparison between in-target production SIRa test and calculated yields from a upscaled GANIL full size target	63
5.1	Implantation depths and the ion distribution in MgO	66
5.2	Implantation depths and the ion distribution in the samples at 260 keV	67
5.3	Release through diffusion from MgO, TiO ₂ and HfO ₂	69
6.1	Periodic table with ionization potentials	71
6.2	MiniMono target and ion source setup	73
9.1	Release curves for CO molecules.	85
9.2	Release curve taken for N ₂ molecule.	88
9.3	Release curves taken for Ne isotopes.	89
9.4	Release curve for ^8He	90

List of Tables

2.1	Experimental data used for the thermodynamical calculations of the adsorption enthalpy on TiO ₂ surfaces.	27
3.1	Experimental data used for the thermodynamical calculations of the adsorption enthalpy on MgO surfaces.	30
3.2	The results of the adsorption enthalpy calculations on ZrO ₂ surfaces.	35
3.3	Experimental data used for the thermodynamical calculations of the adsorption enthalpy on HfO ₂ surfaces	36
3.4	Experimental adsorption enthalpies from the different experiments	40
4.1	The C, Ne and N production compared to the theoretical estimations.	50
4.2	Physical properties of the materials used during the on-line tests at GANIL	54
4.3	Characteristics of the pressed pills of HfO ₂ and MgO	55
4.4	Calculated stopping ranges for ²² Ne and ¹⁰ C in the fibre felt targets	56
4.5	Experimental production of carbon and nitrogen isotopes	58
4.6	Experimental production of sodium, neon and fluorine isotopes	60
4.7	Experimental production of krypton isotopes	60
5.1	Characteristics for the pressed pills and fibre targets used for the implantations	64
5.2	Temperature needed for 10 % of the fractional activity in the samples to remain.	68
6.1	Ionization potential for carbon and nitrogen.	70
6.2	The buffer gases used during the test with the MiniMono ion source	74
6.3	The isotopically enriched gases and their contaminations.	75
6.4	Ionization efficiencies	76
8.1	Explanation of abbreviations and symbols used in the chapter.	80
9.1	Calculated cross-sections with the EPAX and the Silberberg and Tsao method	83
9.2	Comparison between calculations and experiments of release at ISOLDE	84
9.3	Overview of the isotopes and molecules investigated during the experiments with the timing used	85
9.4	Decay mode of the carbon isotopes	86
9.5	Decay mode of the nitrogen isotopes	86

1

Introduction

1.1 Radioactive Ion Beams

There are currently 117 elements known in the periodic system, most of these are naturally abundant around us, others are formed through nuclear reactions. Most of these elements exist in the nature as stable or radioactive isotopes. For every element in the periodic system there are information we like to have, like building stones to understand our life on this planet and the universe. The atomic and nuclear physics experiments seek information about mass, radius, half-life, decay modes, reaction modes, cross sections, spin, magnetic and electric dipole moments and if there are excited states etc. The first studies about atoms were performed by the Greeks. 1896 was the year that H. Becquerel discovered the radioactivity during one of his experiments [1] following the discoveries of Röntgen. The discoveries by M. et P. Curie followed closely¹. Later in 1934, Fermi published the first article on production of radioactive nuclide².

To make studies on the new elements, chemical separations were performed. These isotopes were relatively long-lived and the time between the production and separation, before detection, was not an issue. When the production methods and separation methods became faster, new more short-lived isotopes were discovered: with half-lives down to hours and even minutes. With these, so called off-line methods, the discovery of short-lived isotopes is limited by the time between the production and the detection. To overcome their limitation ISOL (Isotope Separation On Line) systems were developed. In the ISOL method the production and the separation of the products are connected in a closed system. Radioactive nuclei can be produced through different nuclear reactions: fission, fusion, spallation, fragmentation, etc. To guide the beam through electro-magnetic separators and accelerators ions are needed.

¹H. Becquerel, P. and M. Curie shared the Nobel Prize in Physics 1903 for their discoveries of radioactivity.

²Fermi won the Nobel Prize in Physics in 1938 for demonstrating the production of radioactive elements through irradiations.

Thus the atoms produced in the target need to be ionized. The ground state properties (half-lives, mass and decay mode) of the nuclei can be studied directly after separation of a low-energy beam, but to gather additional information about the nuclei often a more energetic beam is needed. As more and more knowledge is gained, the "hunt" for more exotic nuclei with shorter and shorter half-lives is getting more intense, demanding faster, more efficient and purer separation methods. The two main methods for producing radioactive ion beams (RIB) are in-flight (IF) separation and the ISOL (Isotope Separation On Line) method [2, 3, 4]. Both types of facilities have their individual advantages and drawbacks.

1.1.1 In-flight separator

Usually an energetic ion beam (with energies ranging from few MeV/nucleon to GeV/nucleon and masses up to ^{238}U) is interacting with a thin target of a light element (e.g. Be, C or Al) (a few hundred $\mu\text{g}/\text{cm}^2$ up to several g/cm^2) target. When the ion beam passes through the target either fission, fusion or fragmentation will take place. The nuclei produced will be highly ionized with an energy determined by the incoming projectile energy, the reaction Q value and the energy loss in the target. Since the n^+ charged ions are easier to accelerate the in-flight method can provide ion beams with high energies and a large variety of isotopes. The acceleration of the ions to high energies are rather advantageous since the ion beam is highly charged or totally stripped after the production. The experiment performed with this type of separation method are typically any decay studies (with an implanted beam) or nuclear reaction studies at high energy. Some of the working In-Flight facilities are at GSI ³ in Germany, RIKEN ⁴ in Japan, SSI at GANIL ⁵ in France.

1.1.2 Isotope Separation On-Line (ISOL) method

The ISOL method is using a thick target of foils, fibers or powder of metals or refractory compounds. The target is irradiated with an intense beam of neutrons, protons, light or heavy ions leading to short-lived nuclei by nuclear reactions in the target. For efficient diffusion and effusion of the products the ISOL targets can sometimes be heated up to 2000 °C. Due to the thickness of the targets the ISOL method is providing far higher beam intensities than the in-flight method if the release losses are not excessive. After release the products are ionized in an ion source and then extracted with a precise determined energy for the experiments. The ISOL beams are suitable for post-acceleration for low- and medium-energy (0.1-25 MeV/nucleon) beam experiments ⁶, when this is needed. Due to the thick targets and the ionization process the method are limited due to high losses of short lived isotopes, the TIS (Target and Ion Source unit) has to be heated to temperatures where the product are volatile.

The two methods are complementary, but with the possibility of post-acceleration of an ISOL beam medium energy experiments can easily be performed for Coulomb excitation etc.

³<http://www.gsi.de>

⁴<http://www.riken.jp>

⁵<http://www.ganil.fr>

⁶Like at REX-ISOLDE

Slowing down an already high-energy beam leads to large growth of the beam according to the Liouville theorem [5] of conservation of the size in the phase space.

1.2 The ISOLDE facility

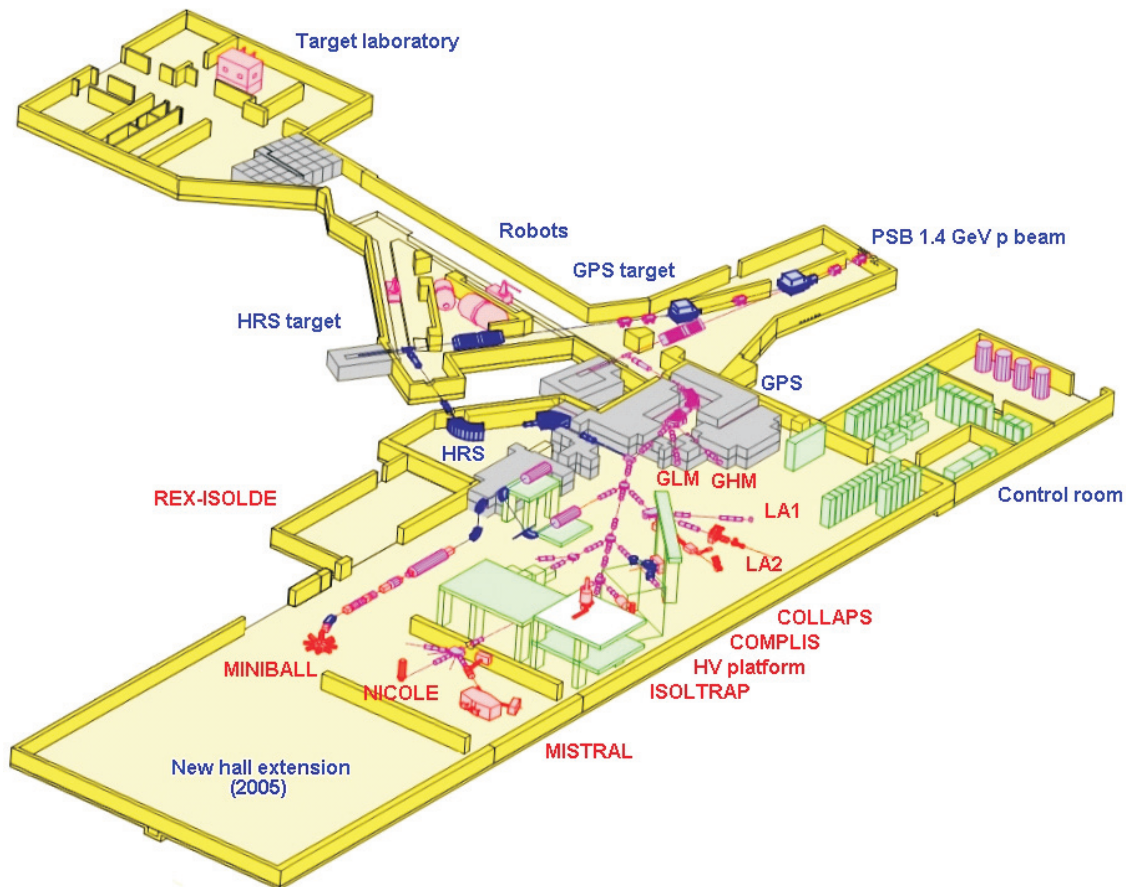


Figure 1.1: The ISOLDE hall. In blue are the proton beam lines, target stations and separator sections. In violet are the experimental beam lines and in red the different experimental set-ups.

ISOLDE stands for Isotope Separator On Line. As the name implies ISOLDE is an ISOL facility. An overview of the installation is given in Fig. 1.1, the facility is integrated into the CERN accelerator complex and is taking protons at an energy of 1.4 GeV from the PS Booster accelerator rings. There are two identical target stations at ISOLDE connected to different mass separators, the HRS (High Resolution Separator) which was designed for a mass resolving power of $\frac{M}{\Delta M} > 5\,000$ and the GPS (General Purpose Separator) which was designed for a mass resolving power of $\frac{M}{\Delta M} > 2400$. Both targets can take proton beams in parallel, meaning that the beam-line complex can deliver a beam up to three experiments at the same time, the different ion beams, coming from the TIS (Target and Ion source units) are directed with electromagnetic guiding out to the experiments. In the Fig. 1.1 the permanent experimental set-

ups are assigned, as WITCH, ASPIC, MISTRAL, ISOLTRAP and COLLAPS (for further detail and upgraded information see <http://isolde.web.cern.ch>). REX-ISOLDE is the post-accelerator used for low-energy beams up to 3.1 MeV/nucleon at present. There are also several possibilities for short-time⁷ experimental set-ups at different beam-lines depending on the requirement of the experiment. For an overview and updated information I recommend the ISOLDE home page at: <http://isolde.web.cern.ch>.

1.3 The ISOL target

A cartoon drawing of the ISOLDE target and ion source unit is shown in Fig. 1.2. The target is typically 20 cm long and the transfer-line is about 5 cm long. There are many requirements

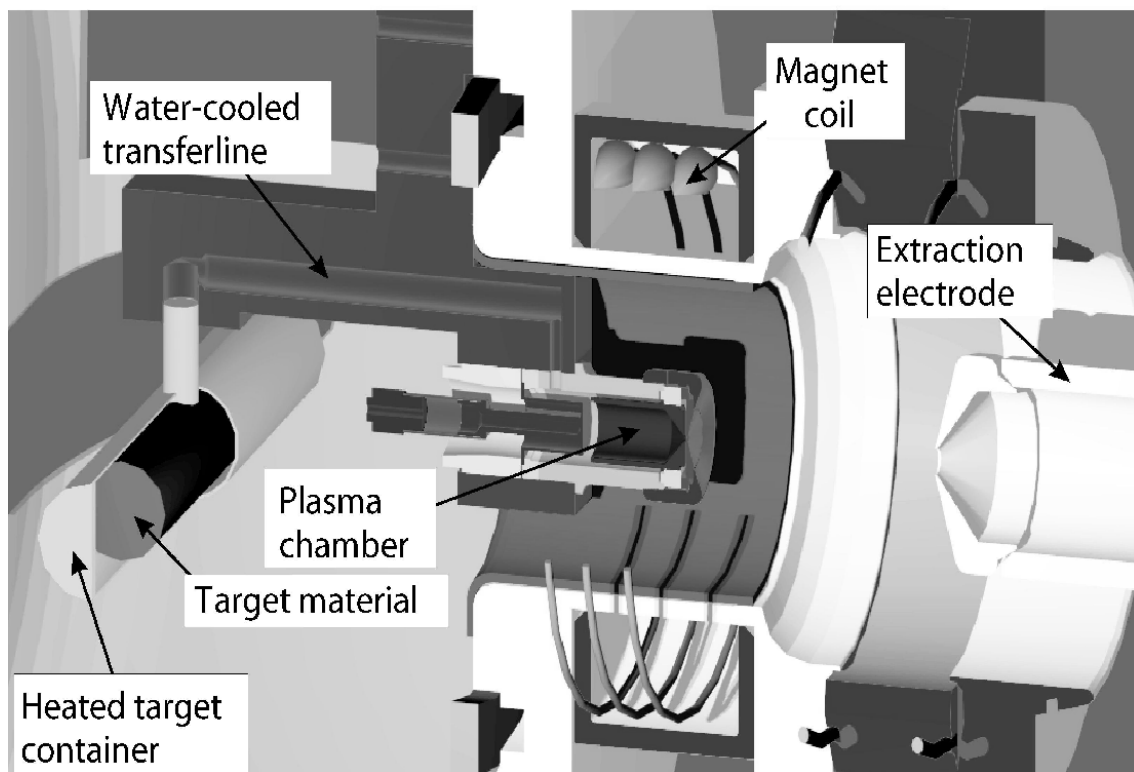


Figure 1.2: Cartoon drawing of the ISOL target and ion source unit. The target inside the target container (at the left) is connected to a FEBIAD plasma ion source through a water-cooled transfer line.

that have to be fulfilled for a TIS unit. Primarily the target has to be enclosed in a vacuum tight container so that no radioactive atoms produced can leave the area. The proton beam is coming into the target through the side of the target container. The beam power deposited in the container and the target from the proton beam is calculated to reach up to $3\text{-}4 \times Z$ MeV per mol/cm^2 target thickness [6] (where Z is the atomic number) which puts further constraints

⁷An ISOLDE experiment is usually dedicated 1-10 days of on-line beam time.

to the construction of the target unit when intense proton beams are used. For fast diffusion of the produced nuclei out from the target material, the target is heated. The materials in the target container also need to withstand reactions like oxidation and carbidization of the surface that in the worst case makes the container so brittle that it might break when handling the target during a target change. The chemical and physical processes going on when the produced atoms are diffusing out of the target material, transported to the ion source and ionized are discussed in the following chapters. Short life times of the isotopes are requiring efficient production, transport and ionization. Three main areas have to be studied for an efficient TIS unit:

1. Production efficiency in the target.
2. Diffusion out of the target.
3. Adsorption of the atoms/molecules on the surface of the target material, target container, transfer line and ion source.
4. Ionization efficiency.

The diffusion time out of the material is strongly dependent on the temperature as seen in the Arrhenius equation 1.1 and will be discussed further in chapter 5.

$$D(T) = D_0 \cdot \exp(-E_a/(R \cdot T)) \quad (1.1)$$

In Eq 1.1 $D(T)$ is the temperature dependent diffusion coefficient [m^2/s], D_0 is the maximum diffusion coefficient (at infinite temperature), E_a is the activation energy for diffusion [$\text{J}/(\text{mol})$], T is the temperature [K] and R is the gas constant [$8.314 \text{ J}/(\text{K mol})$]. The temperature of the target has to be set with consideration of the materials melting temperature and vapor pressure. Due to technical demands (separate heating of the target and ion source, standardized production of different target types and ion source types) a transfer line between the target and the ion source is needed. The transfer line can be used as a thermochromatographic column and separate elements with different adsorption properties. Variants varying from a water-cooled line for noble gases and other chemically inert molecules up to Ta transfer lines heated up to $2200 \text{ }^\circ\text{C}$ for the transmission of metallic elements are routinely used at ISOLDE. Also chemical retention (i.e. the retention of more reactive elements to purify the ion beam) of alkali elements by a quartz transfer line has been used. The effusion time from the target to the ion source is depending on the number of collisions and the surface residence time (t_r) on all surfaces involved. The surface residence time is the average time that a molecule actually "sticks" to a surface after each encounter. When the retention time is much longer than the average flight time between two collisions (typically of the order of μs) or if the adsorption is irreversible, it will contribute significantly to the total transport time or loss through the unit. The different ion sources used at ISOL facilities have to be efficient with short ionization times for a large variety of beams. Depending on the elements that are to be ionized various types of ion sources have therefore been developed. We can now conclude the important parts that have to be optimized for a maximum experimental yield:

- Production rate in the target. Discussed in chapter 4

- Diffusion efficiency out of the target material (ϵ_{dif}). Discussed in chapter 5.
- Transmission efficiency through the transfer line (ϵ_t). Discussed in chapter 2 and 3.
- Ionization efficiency (ϵ_i). Discussed in chapter 6.
- Detection efficiency (ϵ_d). Not discussed here.

At ISOLDE the expression "yield"⁸ describes the radioactive ion beam intensity (ions/s) of a given isotope after extraction from the ISOL target, ionization and mass separation that can be delivered to experiments, normalized to the (average) intensity of the primary proton beam hitting the target (in μA). It is given in units of ions/(s· μA)=ions/ μC where one μC of protons corresponds to $6.25 \cdot 10^{12}$ protons. The PSBooster delivers pulses of about $3.1 \cdot 10^{13}$ protons (= $5\mu\text{C}$) at a usual repetition time of 1.2 s. Generally every second proton pulse goes to ISOLDE, the other pulses are further accelerated by the PS for the high energy experiments at CERN. Occasionally more or less proton pulses are available for ISOLDE. When the number of proton pulses available for ISOLDE is known, the users can easily calculate the beam intensity from the product of the ion yield with the average proton current available (ranging from 1 to 4 $\mu\text{C/s}=\mu\text{A}$).

This ion yield is a product of the normalized in-target production rate P (given by the production cross-section times the target thickness in atoms/cm² corrected for "thick target effects" like additional production by secondary particles) and the subsequent efficiencies.

$$Y = P \cdot \epsilon_{\text{dif}} \cdot \epsilon_s \cdot \epsilon_t \cdot \epsilon_d \quad (1.2)$$

See ref. [7] for an illustration of this formula. Where Y is the measured yield, P is the theoretical production calculated with equation 4.1.

1.4 Carbon and nitrogen

Intense RIB's of carbon isotopes are of significant interest for different nuclear physics experiments [8, 9, 10, 11, 12, 13, 14, 15, 16, 17, 18] and maybe even for heavy ion radiation therapy [19, 20]. The three neutron deficient isotopes ^{9–11}C have half-lives of 126.5(9) ms, 19.29(1) s and 20.38(2) min respectively. The neutron rich isotopes ^{14–22}C have half-lives of 5730 a, 2.45(1) s, 747(8) ms, 193(5) ms, 92(2) ms, 49(2) ms, 14(3) ms, <30 ns and 6.2(14) ms [21], respectively. The extremely short half-life of ²¹C is due to the fact that it is neutron unbound. A similar interest, as for the carbon isotopes, exists in production of RIB's of nitrogen [22, 23]. For certain elements, for example when the element in elementary form is highly reactive with the surfaces around or has a high vaporization temperature, it is advantageous to use chemical evaporation, i.e. molecules instead of atoms for the transport out of the target and into the ion source, as is the case for carbon, nitrogen, oxygen, fluorine and chlorine. Carbon atoms may form strong bonds to the different materials used of the target, container and/or transfer line. O₂ is added or generated in-situ from the vapor pressure of oxide targets allowing CO, CO₂ and other molecules to be formed. Fig. 1.5 shows the vapor pressure vs. temperature

⁸In the following I will instead use the expression "ion yield" to avoid confusion with chemical "yields"

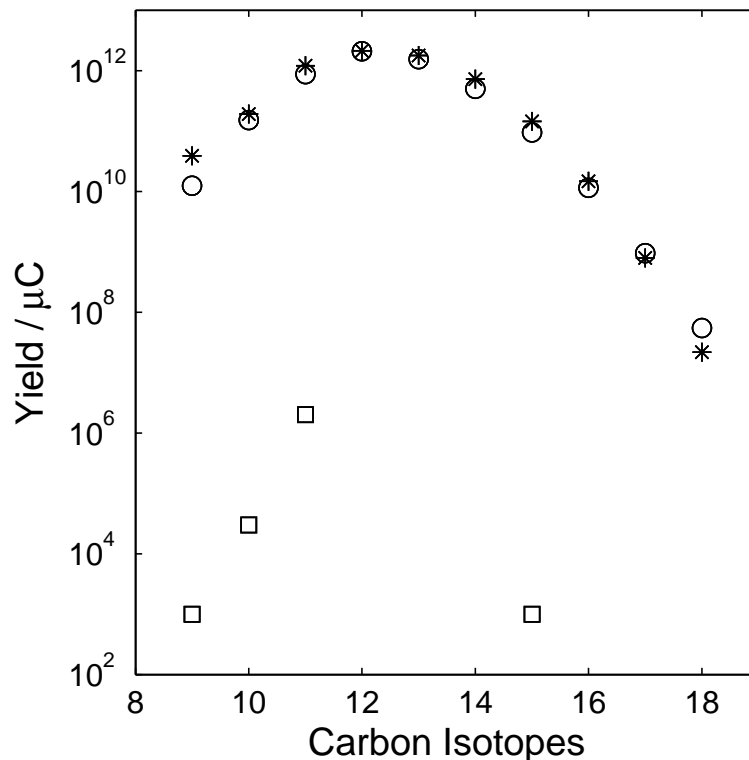


Figure 1.3: A comparison of the in-target production rate P calculated from semi-empirical cross sections and the experimental ion yields Y , in * and o, of carbon isotopes and the experimental yields, as □, from a on-line run with a MgO target, Ta transfer line and a FEBIAD ion source.

for different typical target materials. The target and ion source unit has typically a high surface to volume ratio and a pressures in the 10^{-4} mbar range. Given the partly very short half-lives mentioned above, and the fact that the individual molecules undergo some $>10^6$ collisions on their way to the ion source, it becomes clear that the adsorption properties, namely the surface residence times at each surface encounter, are crucial in determining the intensity of the resulting RIB [24, 7, 25].

1.5 Material selection

The selection of materials to be studied was chosen with regards to the performances and possibilities to construct an ISOLDE target. The first conclusion, to produce carbon in molecular form was done after considering the vapor pressure of carbon compared to the molecules. As seen in Fig. 1.5 many of the used target materials risks to be vaporized before the carbon in an elementary form would be released. Since CO and CO₂ has a higher vapor pressure it also provides a larger choice of materials for the target since the temperature can be kept at lower

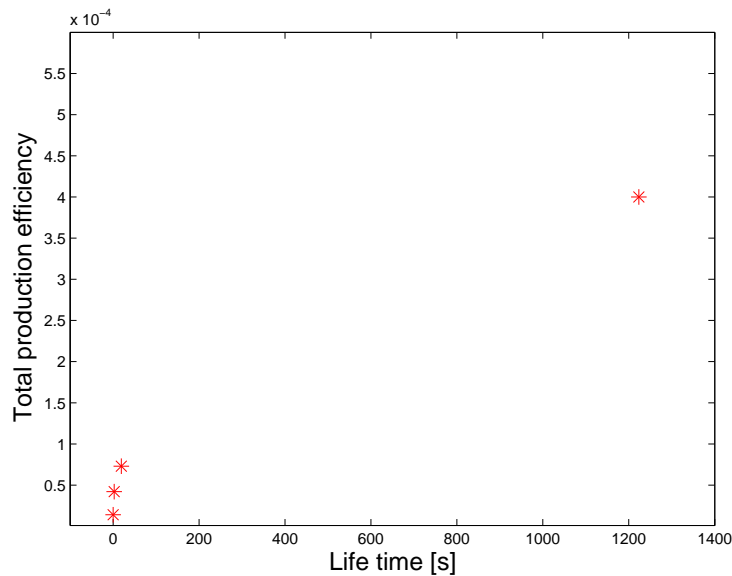


Figure 1.4: The production efficiency compared to the half-life of the carbon isotopes. A strong dependency on the half-life is detected.

temperatures. To form molecules we also need access to oxygen in the target. It is in principle possible to add oxygen in a controlled way to the target via a calibrated leak, but the usual metal targets would get big quantities of oxygen and change their properties after oxidation at the high temperatures needed for a rapid out diffusion of carbon. Therefore it is better to start with oxide target materials. For certain elements the oxides are thermally decomposed or reduced when heated in vacuum. The required oxygen can thus even be produced in-situ by a slow thermal decomposition or reduction of the target materials. The production cross section (σ), i.e. the probability that the incoming beam will produce the isotopes of interest while interacting with the target material can be calculated [26, 27] or measured. In Fig. 1.6 the cross section, retrieved experimentally [28, 29], for production of ^{16}C is plotted against the proton number (Z) of the target at different primary proton beam intensities. Among the light targets only isotopically enriched ^{18}O provides a high cross-section for production of the close-by ^{16}C (in (p,3p) reactions). Else it is favorable to use higher Z target materials and high primary beam energies. For the neutron deficient carbon isotopes the production cross section is high for ^{16}O that has a natural abundance of 99.757 %. Thus any metal oxide can be chosen as target material for neutron deficient carbon isotopes. Since both neutron deficient and neutron rich carbon isotopes is to be produced, calculations of the theoretical cross sections with two different models (EPAX model and the Silberberg and Tsao model, see chapter 4) (Fig. 1.7) was performed for a choice of possible metal oxides. Both models are validated (Fig. 1.8) with the comparison from experimentally retrieved cross sections [28, 30] and modeled cross sections at 1 GeV protons. From Fig. 1.7 the target material for the neutron deficient carbon and nitrogen molecules, MgO and CaO are good candidates while for the neutron rich isotopes it would be TiO_2 , HfO_2 or UO_x respectively.

To test the release parameters from the target (see chapter 4.2.2 and 5) on-line tests and

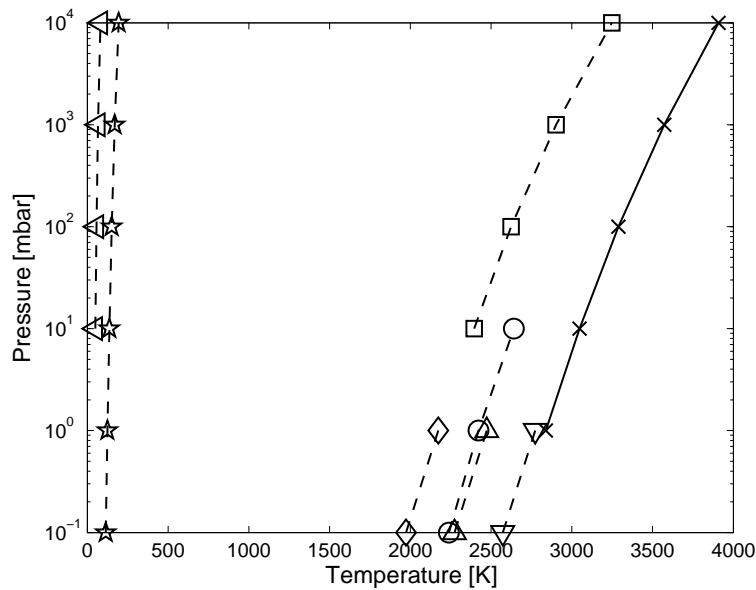


Figure 1.5: Vapor pressure of metal oxides compared to elemental carbon (\times), CO (\triangleleft) and CO_2 (\star). The metal oxides are displayed as follows: MgO (\square), Al_2O_3 (\diamond), SiO_2 (\circ), TiO_2 (\triangle) and HfO_2 (∇).

off-line measurements were performed. The diffusion time out of a liquid metal target will often be longer than out of a thin metal foil⁹. In a powder the diffusion time is rather short but slow effusion between the powder grains might instead produce a problem. Target tests for other isotopes with oxide fiber target materials [31] have been performed and show relatively short release times compared with metal oxide powder targets. During a run of one week or more the target material should not change its macro- or micro structure. Moreover excessive vapor pressure of the target material might disturb the functioning of the ion source. Chemical reactions between the target material and the target container also have to be considered, as mentioned above. When the elements are created there is no specific chemical separation in high-energy reactions, a cocktail of atoms with lower mass than the target material will be produced with a statistical distribution depending on the cross-sections is to be expected. The elements with a lower volatility than the target material will stay in the target and the others may effuse out, therefore the target temperature can be used as a first chemical separation of the products. Release tests were performed at GANIL with pressed powder pill targets of MgO and fibre felt targets of HfO_2 , TiO_2 and ZrO_2 .

Losses due to retentions or irreversible adsorption at the walls of the target unit was tested with a thermo chromatography method at the Paul Scherrer Institute. These experiments were performed using the beta plus decay from ^{11}C (and ^{13}N) as a tracer in a thermo chromatography column (see chapter 2). The adsorption enthalpy of CO, CO_2 and some nitrogen molecules were measured on MgO, Al_2O_3 , SiO_2 , CaO, TiO_2 , ZrO_2 and HfO_2 surfaces. ThO_2 and UO_x

⁹This is for a typical ISOL target where the diffusion path out of a liquid metal target is longer than out of a thin foil, it do not consider liquid drop targets or similar.

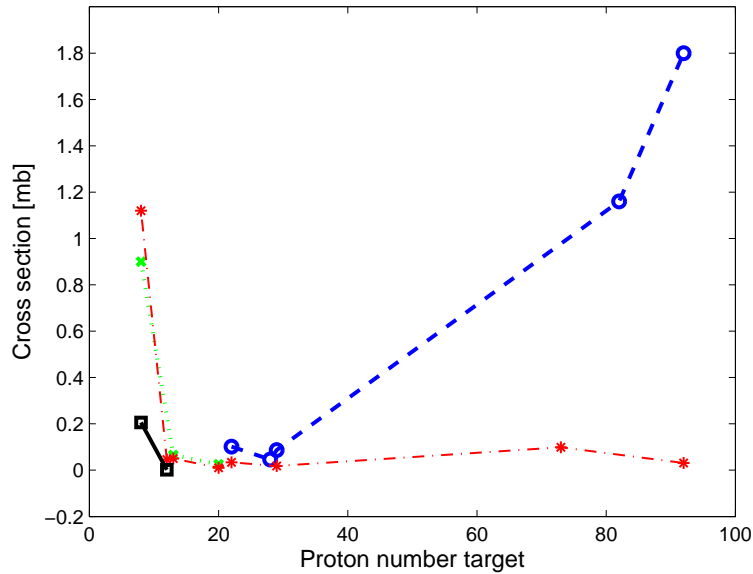


Figure 1.6: The cross sections for production of ^{16}C from different targets at different energies. In blue \circ are the production cross sections from Ti, Ni, Cu, Pb and U at 2.8 GeV, in green \times from O, Al and Ca at 1.2 GeV, in red $*$ from O, Mg, Al, Ca, Ti, Cu, Ta and U at 1 GeV and in black \square are the production cross sections from O and Mg at 156 MeV. The cross section for the production of carbon are high for oxygen (for this ^{18}O was used instead of ^{16}O), then drops down and goes slowly up for heavier nuclei and with higher energy of the incoming proton beam

represent also potential target materials. The adsorption enthalpies on these surfaces could not be measured with our method due to disturbing background from radioactive decay of the actinides. Above in section 1.1 the importance of ionization was explained for a relatively fast separation and steering of the beam, off-line tests (cf. chapter 6.3) were performed with a MiniMono ECR (Electron Cyclotron Resonance) ion source at ISOLDE. The MiniMono ion source tests (see chapter 6) and the on-line release tests at ISOLDE and GANIL (see chapter 4).

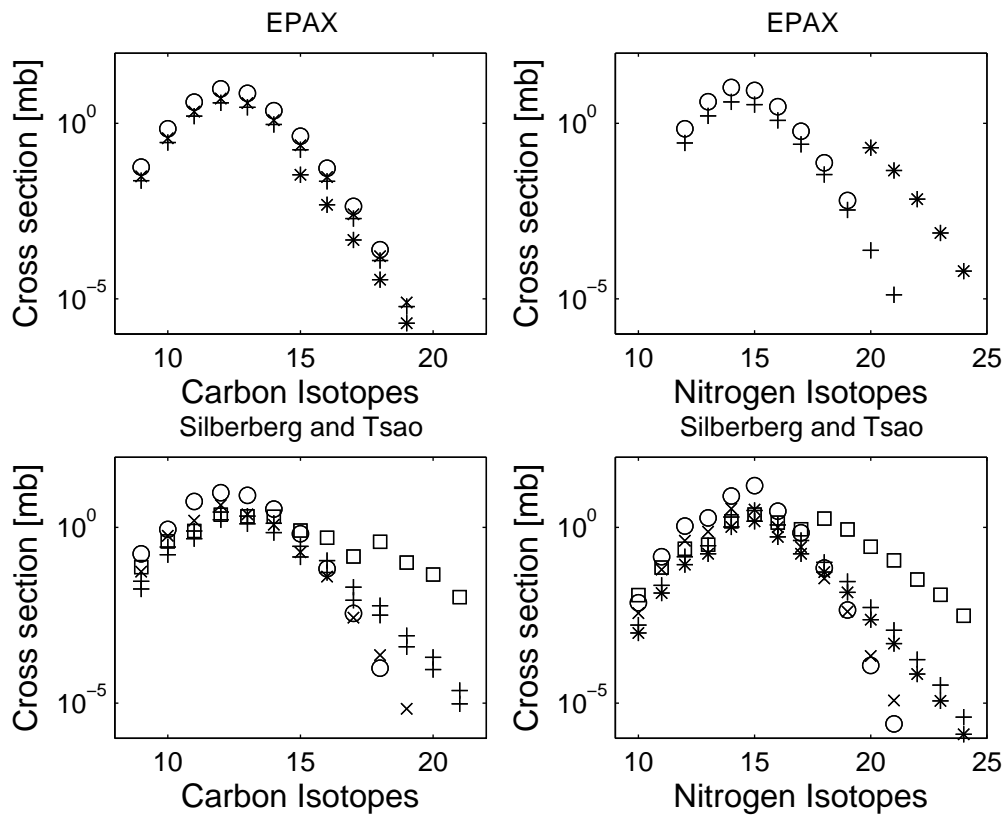


Figure 1.7: Production of carbon and nitrogen isotopes calculated with the cross sections from the EPAX (the two figures on the top) and the Silverberg and Tsao (the two lower figures) calculations. Production from MgO ○, CaO ×, TiO₂ +, HfO₂ * and UC_x □.

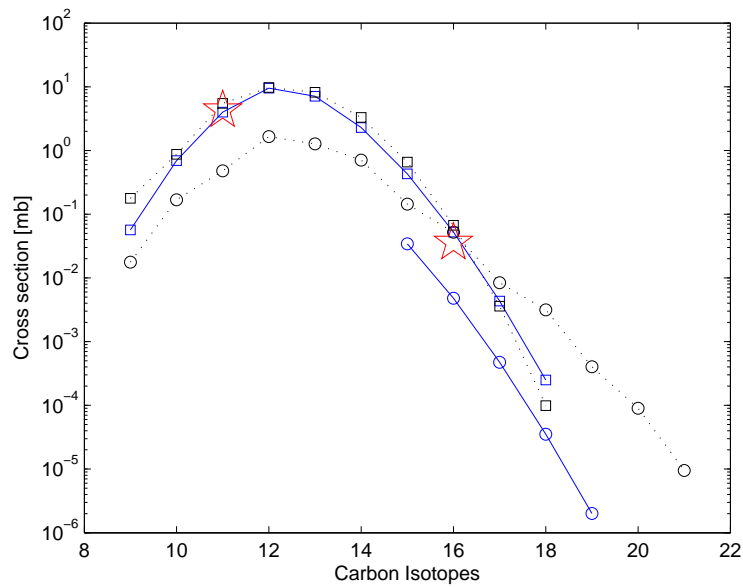


Figure 1.8: Comparison between two models for calculation of the cross section for production of carbon from a Mg \square target and a Hf \circ target. The calculations done with the EPAX code is seen in straight blue lines and with the Silberberg and Tsao code is seen in dashed black lines. The stars are representing experimentally retrieved cross section data for production of ^{11}C and ^{16}C from targets with similar properties, a ^{27}Al target and a Ta target.

2

Thermochromatography experiments

This chapter has been submitted in similar form to Radiochimica Acta: H. Frånberg, M. Ammann, H. W. Gäggeler and U. Köster, Thermochromatography study of ^{11}C and ^{13}N oxides on TiO_2 .

2.1 Introduction

Traditionally, adsorption properties of CO and CO₂ or of nitrogen oxides on solid oxides are of interest in a number of different fields, such as heterogeneous catalysis or basic surface science. CO is an important reactant for hydrogenation reactions on catalysts; CO₂ has often been used as a proxy for the adsorption of an acid molecule; both NO and NO₂ adsorption are important steps in catalytic NO_x reduction or gas sensing [32]. The specific motivation for this study is the fact that carbon molecules play a key role in the production of radioactive ion beams (RIB's) of very short-lived carbon isotopes via the ISOL method. Due to the thick targets used with the ISOL method, high beam intensities are provided if the release losses are not excessive. Unfortunately for carbon, this is presently not the case. Short-lived carbon atoms may form strong bonds to the target material or the housing surface. As mentioned in the introduction O₂ is added or generated in-situ from the vapor pressure of oxide targets allowing CO, CO₂ and other molecules to be formed. The transport out of the target and through the transfer line is a critical step in producing intense RIBs. While modern surface science provides many powerful tools to measure adsorption properties under well-defined conditions, the complex environment of the surfaces under study for the purpose of RIB production calls for a different method, in which realistic surface mimics can be exposed to the gases of interest. Thermochromatography (TC) is a method that has found widespread application in radiochemistry [33, 34, 35, 36, 37, 38, 39]. Radioactive nuclides are transported along a negative temperature gradient over the surface under study in a flow tube (chromatographic column) during a given period of time of the order of their radioactive half-life. After

this time, the position of the molecules in the temperature gradient is determined by scanning the radioactivity along the surface. While at sufficiently high temperature their transport along the surface is governed by the carrier gas flow rate, at lower temperature, the increasing surface residence times lead to progressively stronger retention, and the migration velocity slows down significantly. This process is specific for the adsorption properties of the molecule on the surface under investigation and leads to chromatographic separation of chemically different species. It can be described by the laws of linear gas chromatography [40] and has also been corroborated with Monte Carlo modeling of the explicit micro physical processes at the surface coupled to gas phase diffusion [41]. The quantity that is retrieved from such an experiment is either the gas surface equilibrium partitioning coefficient at the temperature at which the radioactive isotopes have been observed, which is also directly equivalent to a macroscopic retention time, or alternatively, the microscopic surface residence time, if the Monte Carlo model has been used to simulate the migration along the column. From both quantities, adsorption enthalpies can be derived under the assumption of an appropriate adsorption model. Therefore, this method allows retrieving straightforward information relevant to the problems around RIB production as stated above, but also allows comparing the adsorption properties observed to those provided by other basic surface science methods, such as temperature programmed desorption (TPD) experiments. In this study, we report on TC investigations of adsorption of ^{11}C -labeled CO and CO₂, as well as ^{13}N labeled nitrogen oxides on different oxide material. The first section will only discuss the TiO₂ surfaces. TiO₂ is one of the suitable materials for an ISOL target for the production of carbon isotopes. In the following sections we show the results and discuss other potentially suitable materials that are, for example; MgO, CaO, ZrO₂, HfO₂, CeO₂, ThO₂ and UO₂. The present more thorough study on TiO₂ is motivated by the fact that adsorption of the mentioned gases on TiO₂ is well documented due to the importance of TiO₂ in a wide range of applications, which allow comparison of our results to those from basic surface science studies. We use the positron emitting isotopes ^{11}C and ^{13}N with half-lives of 20.4 min and 10.0 min, respectively, which can be easily detected through their annihilation γ -lines with $E_{\gamma}=511$ keV. These nuclides are also easily obtained through (p, α) reactions at low proton energies. The use of ^{13}N in gas chemical and surface chemical studies has been established before by Ammann [42]. The other more short-lived isotopes of carbon and nitrogen would be much less suitable for such model studies.

2.2 Set-up of the experiment

The experiments have been performed at the Paul Scherrer Institute. ^{11}C and ^{13}N have been produced in the target setup shown in Fig. 2.1. This facility (PROTRAC) is a system based on an earlier gas target setup for the continuous on-line production of ^{13}N [42]. An 11 cm long on-line gas target $^{16}\text{O}/^4\text{He}$ (10-20% O₂ and 80-90% He, both with 99.9999% purity) is kept at 2.5 bar pressure in a quartz cone inside an aluminium housing. The target is irradiated with 10 μA 35 MeV protons from the Injector 2 cyclotron at Paul Scherrer Institute. The quartz cone has an aluminium (2 mm) - water (8 mm) - aluminium (0.7 mm) window at the entrance and a simple aluminium window at its exit. The water-cooled entrance window of the target reduces the proton energy, so that the gas is effectively irradiated with 15 MeV protons. ^{13}N is produced

via the reaction $^{16}\text{O}(p,\alpha)^{13}\text{N}$, while ^{11}C is produced through the reaction $^{14}\text{N}(p,\alpha)^{11}\text{C}$ with ^{14}N impurities and possibly also through the (n,2n) reaction of adventitious carbon on the surfaces of the target housing by neutrons produced in the entrance window. In the oxidative environment of the irradiated gas target, the primary ^{13}N and ^{11}C radicals are presumably rapidly oxidized to HNO_3 , CO , CO_2 or HCOOH , respectively, part of which would be lost to the walls of the tubes through which they are transported to the experiment. Therefore, a rapid conversion to the relatively inert NO and CO or CO_2 , respectively, was achieved by passing the gas through a TiC converter (25g powder from CERAC 99.5% purity T-1222) at 300-320°C immediately downstream of the target. Nitrogen and carbon impurities in the gas supplies or from the lines participate in radiation chemistry in the target. This leads to about 10 ppb NO and a few hundred ppb CO and CO_2 carried to the laboratory along with the labeled molecules. A 590 m long polyvinylidene fluoride (PVDF) tube transports the gas leaving the target and the converter to the laboratory. This tube was housed in a containment tube flushed with 3000 cm^3/min N_2 at a pressure of 50 mbar below ambient. To detect eventual leaks, this gas was constantly monitored with a radiation detector. While CO and CO_2 are chemically inert on the time scale of the transport to the laboratory, nitrogen monoxide is partly oxidized to NO_2 due to the presence of O_2 . Furthermore, in presence of traces of water, NO_2 can also be converted to HONO on all available surfaces. Therefore, labeled nitrogen oxides included the species NO , NO_2 and HONO . To quantitatively determine and monitor the concentration of the labeled molecules arriving at the laboratory, the transport tube was coiled around the head of a calibrated counting device in the laboratory [42]. By means of calibrated mass flow controllers (Brooks Instruments, The Netherlands), the gas could be distributed to three different experiments in the laboratory as seen in Fig. 2.1. A fourth mass flow controller was used to keep the total flow rate through the target and the gas transport tube constant. In the experiment described in this article, a constant flow rate of 100 cm^3/min of the gas coming from the target was mixed with 600 cm^3/min N_2 (6.0, Carbagas AG) as shown schematically in Fig. 2.2. The central part of the experiment is the thermochromatography (TC) oven, through which the labeled molecules are passed. All gas transport in the laboratory was through perfluoroalkoxy copolymer (PFA) 4 mm tubing held at room temperature. The experiment was performed at atmospheric pressure, and all flows were controlled by mass flow controllers (Brooks Instruments). To measure the concentration of (non-labeled) CO_2 in the flow system a CO_2 -analyzer (Thermo Environmental Instruments Inc. 41C CO_2 analyzer) was used at different positions along the experimental setup (see Fig. 2.2). To clearly define the chemical speciation of the ^{11}C isotope used for the following experiments the gas was passed through a CuO oven consisting of a quartz tube filled with CuO splinters (MERCK, 20% CuO covering the surface and 80% Cu_2O in the bulk) kept at 800°C for the chemical conversion of CO , HCOOH and possibly present hydrocarbons to CO_2 . For absorption of CO_2 in some characterization experiments a KOH trap was mounted before the TC column (e.g. to determine the amount of labeled and non-labeled CO_2 when switching in and out the CuO oven). KOH is a CO_2 absorber, through the reaction $2\text{KOH} + \text{CO}_2(\text{g}) \rightarrow \text{K}_2\text{CO}_3(\text{s}) + \text{H}_2\text{O}$. Two further chemical traps packed with activated carbon were placed parallel to and after the TC oven, to quantify the amount of all labeled molecules and the amount of those passing through the TC experiment, respectively. The gas flow rate through the TC oven of 50 cm^3/min was controlled by a separate mass flow controller connected to a pump, while the remaining flow

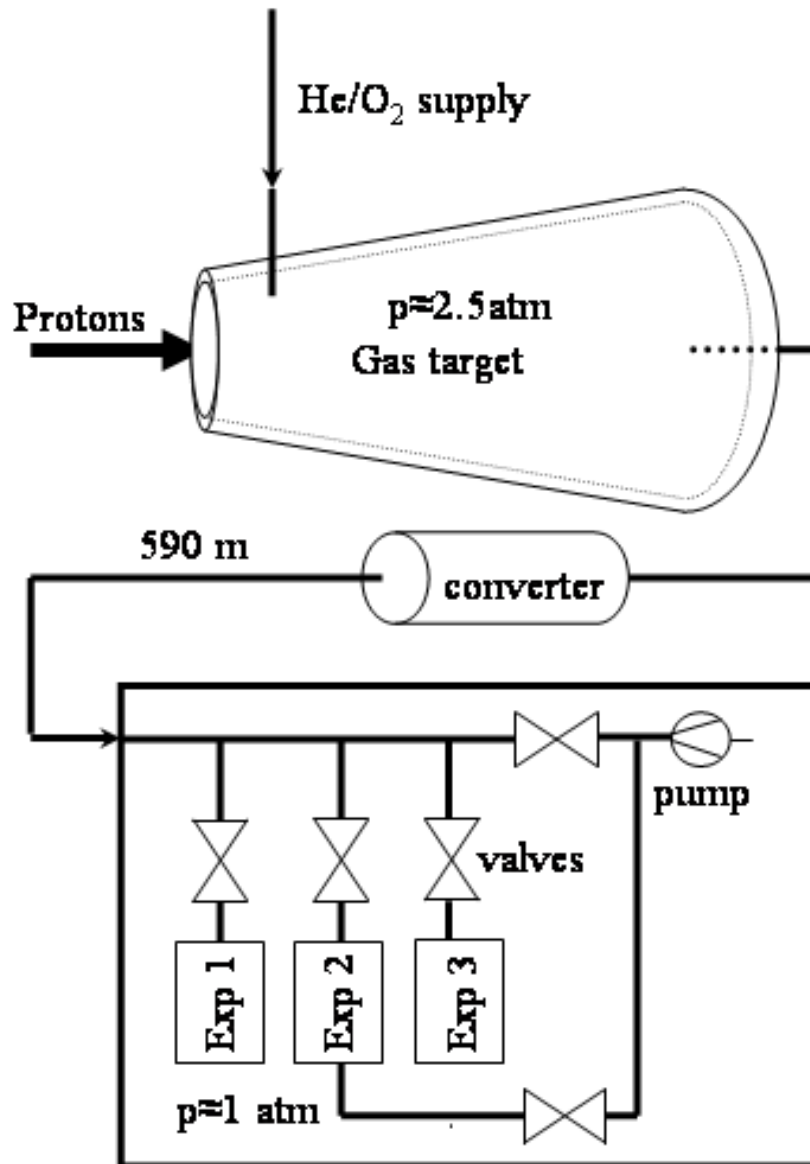


Figure 2.1: PROTRAC gas target, converter and gas distribution.

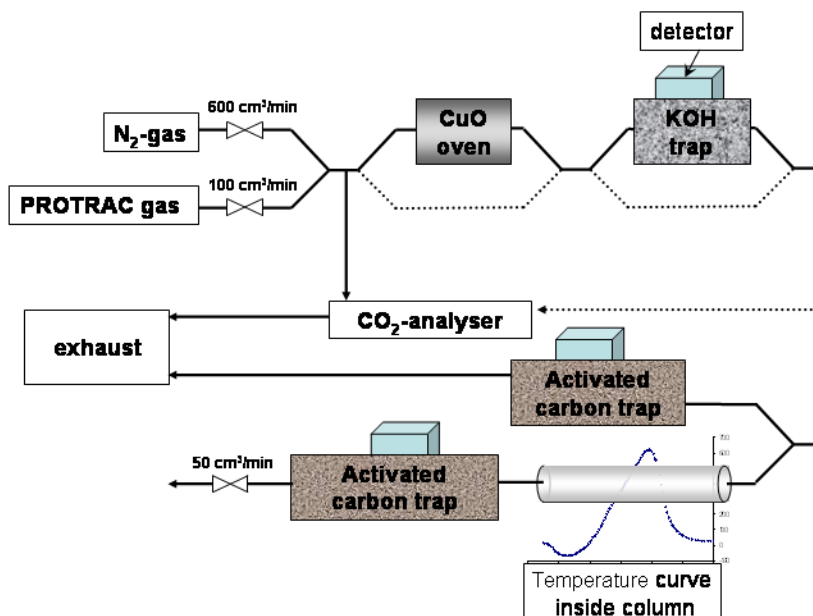


Figure 2.2: Experimental set-up of the thermochromatography experiments.

passed to an open end in a vented hood.

2.2.1 Thermochromatography oven

There are two ovens used for the experiments described below, a "cold" oven and a "warm" oven, the latter one is used for adsorption properties of the target materials and is therefore described here below, the cold oven is only used for two specific materials and is therefore described together with the analysis of these experiments.

The TC oven is constructed to provide a stable and reproducible temperature gradient. The 85 cm long oven contains an inner tube with 3 cm inner diameter consisting of Al_2O_3 . 20 cm from the entrance the tube is surrounded by heating filaments (W wires) to have a controlled heating of the tube. To achieve different heating power along the oven, the wires are most densely coiled around the warmest part (after 40 cm) then again less densely wired. For the protection of the heating wires the housing is constantly flushed with argon. The last 20 cm of the Al_2O_3 tube is immersed in liquid N_2 (LN_2) for stable cooling. The temperature measurement for controlling the heating power was performed by a thermocouple positioned at the warmest point. The maximum temperature T_{max} was varied for different experiments to achieve different temperature gradients, between -35 K/cm and -16.5 K/cm , with an error of $\pm 5 \text{ K/cm}$. Typical temperature gradients (see Fig. 2.3), show that the gradient was not perfectly constant over the full temperature range. The actual local gradients were considered in the analysis. The temperature gradient was continuously monitored inside the Al_2O_3 tube by four thermocouples (PtRh30-PtRh6) during the experiments. To have a control of the actual temperature within the chromatographic column as a function of the temperature readings

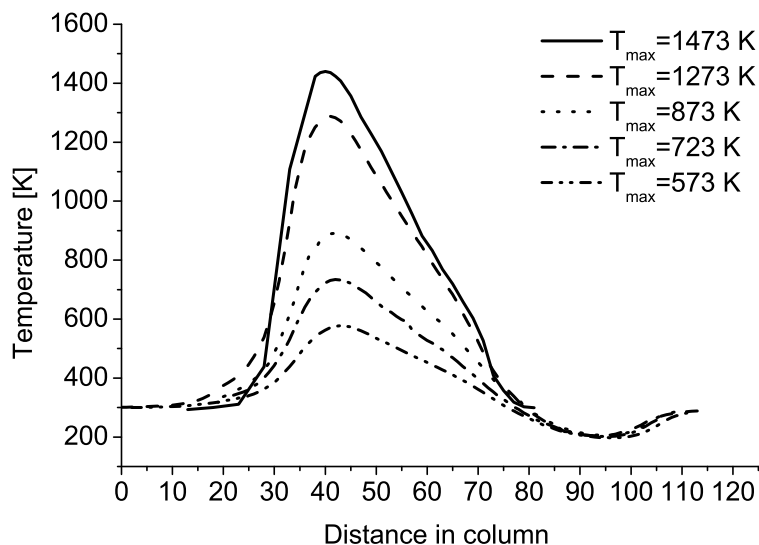


Figure 2.3: Measured temperature distribution in the experiments.

outside the column under flowing gas the gradient was measured with a thermocouple all along the column. Overall, the temperature profile was stable and reproducible.

2.2.2 Preparation and handling of chromatographic columns.

The TC column is a 115 cm long quartz (SiO_2) column with an inner diameter of 4 mm. The inner surface is sandblasted to facilitate the coating procedure. The metal oxide in this first example, TiO_2 powder and ethanol were mixed until a smooth slurry was achieved. The column was filled with the slurry up to 50 cm from the entrance of the column (the warmest point inside the TC oven). While slowly turning the column in an inclined position, the slurry was allowed to run out, leaving a thin coating on the walls. For a uniform drying of the column a small flow of O_2 was passed through the column. After drying, the surface was checked for irregularities to make sure that only visibly homogeneously coated columns were used. The column was then heated to temperatures between 450 and 550 K during a few hours in an oven under H_2 flow to remove traces of the alcohol and eventual hydrocarbons. Once the column was inserted into the TC oven, it was flushed for 40–60 min prior to the experiment with the N_2 carrier gas to allow the temperature gradient within the column to be established. 100 cm^3/min of the PROTRAC gas was thereafter added to the carrier gas. After 40 min, the normal experiment duration, the gas flow through the TC column was stopped, the column withdrawn from the oven, put into a bath of liquid nitrogen so that weakly adsorbed species in the low temperature area are not diffusing away. Finally, the detector system could scan along the column for the measurement of the distribution of the labeled species. This is the way that most of the TC column in this thesis was prepared, if nothing else is indicated.

2.2.3 Detector set-up.

Two BGO (bismuth germanate) crystals (3 cm in diameter), each coupled to a photomultiplier tube, were mounted face to face at 3.5 cm distance from each other and attached to a stepper motor for scanning along the TC column [42]. The activity and position of the deposited ^{11}C and ^{13}N were both measured through detection of the two 511 keV coincident annihilation gamma rays detected by the fast coincident counting electronics coupled to the photomultiplier tubes. The counter was read in intervals corresponding to 0.5 cm length resolution along the TC column. The radioactivity distribution along the column was scanned repeatedly with intervals of three minutes. A fit of the observed radioactivity decay associated with each position allows quantifying the contribution of ^{13}N and ^{11}C with half-lives of 10.0 and 20.4 min, respectively. CsI scintillation counters (Carroll and Ramsey, Model 105S-1 Single-channel high sensitivity radiation detector) were used to determine the amount of ^{11}C and ^{13}N in each chemical trap put into the flow system at other points as described above. By following the accumulation in the traps during the TC experiment (40 min) and the associated decay in the traps afterwards, the molecules present in each experiment were identified.

2.2.4 Deposition temperatures

Since the temperature gradient in the TC column is known, the so called deposition temperature (T_{dep}) defined as the temperature at which the maximum amount of activity of an individual species has been observed ("chromatographic peak"), can be determined from the scans of the radioactivity distribution. T_{dep} is characteristic for the adsorption properties of the molecule on the specific surface in the column.

2.3 Results and discussion

From the many studies available regarding CO and CO₂ adsorption on TiO₂, it is well established that both molecules can undergo weak physisorption as well as more strong dissociative chemisorption. These processes depend strongly on the nature of the surface, and specifically on the valency of the titanium sites [43]. Most of the reactive processes (both decomposition and oxidation) are induced by the presence of partially reduced surface titanium occurring at defects or after annealing in vacuum [44]. Note, though, that our experiments were performed under oxidizing conditions, where the appearance of reduced sites was most probably suppressed. Similar features apply to the surface chemistry of nitrogen oxides on TiO₂. NO undergoes only very weak physisorption with interaction energies beyond the reach of the method used here [45, 46]. Adsorbed nitrogen dioxide, on the other hand, can undergo dissociation and disproportionation leading to nitrites and nitrates. Similar to the inter conversion of nitrogen oxides species in the target gas mentioned in the experimental part, conversion of NO₂ to HONO and NO is also likely to occur on the TiO₂ surface. It is therefore reasonable that complex chromatograms are evolving when the labeled carbon and nitrogen oxides interact with TiO₂. Fig. 2.4 shows a typical distribution of activity from a TC experiment, where the gas from the target, diluted with N₂, was directly fed into the TC column. While the contribution of ^{13}N and ^{11}C can be obtained from analyzing the decay time from the repeated scans (see

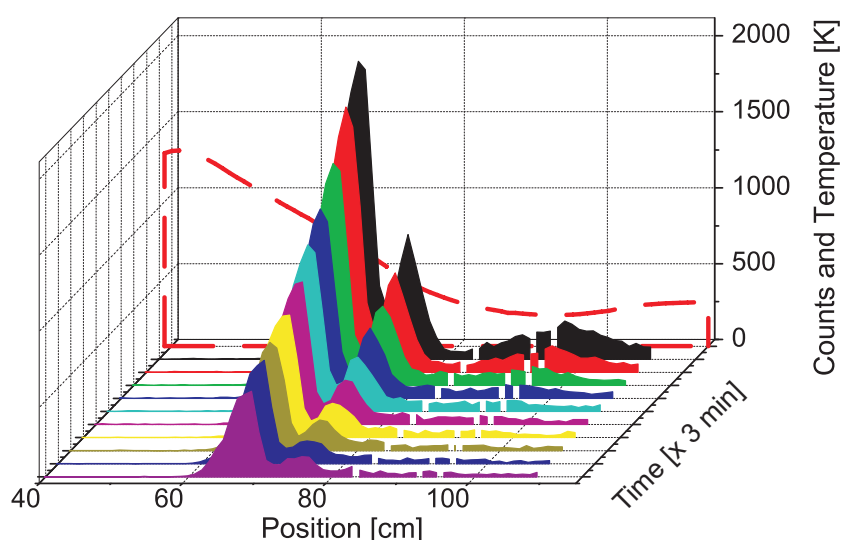


Figure 2.4: Observed distribution of radioactivity along a TiO_2 coated thermochromatography column. The repeated scans, one every third minute, allow to assign the peaks to ^{11}C and ^{13}N according to their half-lives. The temperature distribution in the column is shown by the red dashed line.

Fig. 2.4), the assignment of a peak to the proper chemical species is less straightforward. We also note that in case a slow decomposition reaction occurs at high temperature, the same species (e.g., CO_2) may lead to a peak at the deposition temperature of CO_2 , but also to a peak at lower temperature, where e.g. CO would adsorb. It was not possible to chemically separate the NO_x species entirely from the gas phase prior to the experiment without affecting too strongly the transmission of the ^{11}C -labeled CO_x species. Therefore, we have checked the peak assignment by performing a series of experiments, in which we switched in and out the CuO oven and the KOH trap (see Fig. 2.2) to change the chemical speciation of the labeled molecules before they are admitted into the TC column. The effectiveness of the oxidation was measured through analysis of non-labeled CO_2 with the CO_2 analyzer showing that the CO_2 concentration in this experiment increased by 80 ppb from 150 ppb to 230 ppb when the CuO oven was switched in. The gradient was also varied to see how the adsorption peaks moved with the temperature or to detect eventual temperature dependent reactions.

The first experiment A) was performed with the diluted, but untreated target gas, as described above. Further on, in experiment B) the diluted target gas was passed over the CuO oven for the oxidation of all CO to CO_2 , prior to the TC oven. In the third configuration C), CO_2 was removed from the oxidized gas with the KOH trap. Finally in D) the diluted, untreated gas as in A) was passed through the KOH trap. Fig. 2.5 shows the resulting four chromatograms of this series taken during the first scan of each column. The temperature gradient is represented by the dotted line. In Fig. 2.6 data from each repeated scan of the columns are represented with \blacksquare , \bullet , \blacktriangle or \blacktriangledown , respectively, for positions at which the corresponding peak contributes most of the activity. No background subtraction was made since it is insignificant due to coincident detection of 511 keV γ 's. The calculated decay curves expected for pure ^{11}C (blue - - -) and

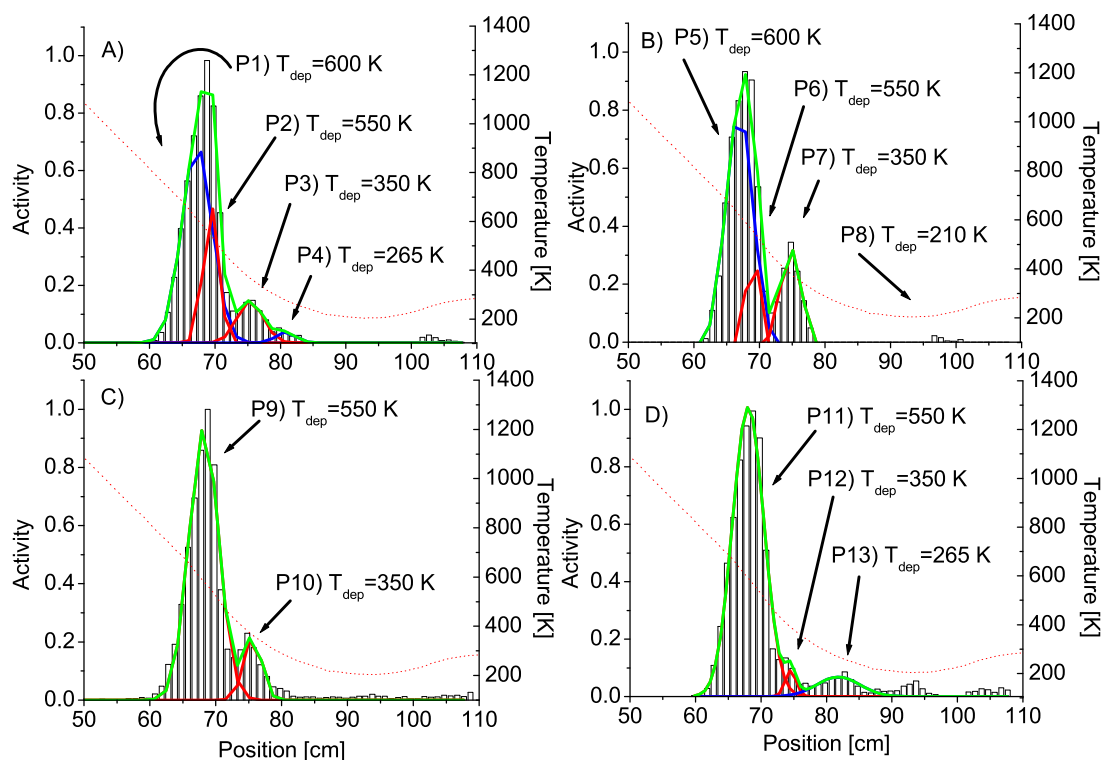


Figure 2.5: Chromatograms with fitted peaks resulting from a series of experiments. A) Mixture of ^{11}CO , $^{11}\text{CO}_2$, $^{13}\text{NO}_2$ and HO^{13}NO . B) Mixture of $^{11}\text{CO}_2$, $^{13}\text{NO}_2$ and HO^{13}NO . C) $^{13}\text{NO}_2$ and HO^{13}NO . D) Mixture of ^{11}CO , $^{13}\text{NO}_2$ and HO^{13}NO . For the assignments of P1) through P13) see text.

^{13}N (red - · · -) decays are also shown in Fig. 2.6.

Fig. 2.5 A) shows the normalized histogram resulting from the first experiment (A). Four partially overlapping peaks P1–P4 can be assigned, as shown with their corresponding Gaussian fits. The deposition temperatures are P1 at 600 K, P2 at 550 K, P3 at 350 K and P4 at 265 K respectively. Fig. 2.6 A) shows the activity decrease at the positions, where the corresponding peak contributes most to the measured activity. Comparison with the expected decay curves allows identifying the isotope contribution to each peak. Because the adsorption temperatures of some species are very close to each other and therefore the adsorption peaks overlap, this is not unambiguously possible everywhere. In those cases, removing some of the species by the traps upstream of the experiment leads to an isotopically pure deposition in the other experiments, see below. This procedure also allowed to clearly separate the first broad peak into its two contributions. Therefore P1 and P4 are due to ^{11}C (although P1 is overlapping some with P2), P3 due to ^{13}N and P2 is overlapping with P1 but clearly contributes ^{13}N activity at this temperature.

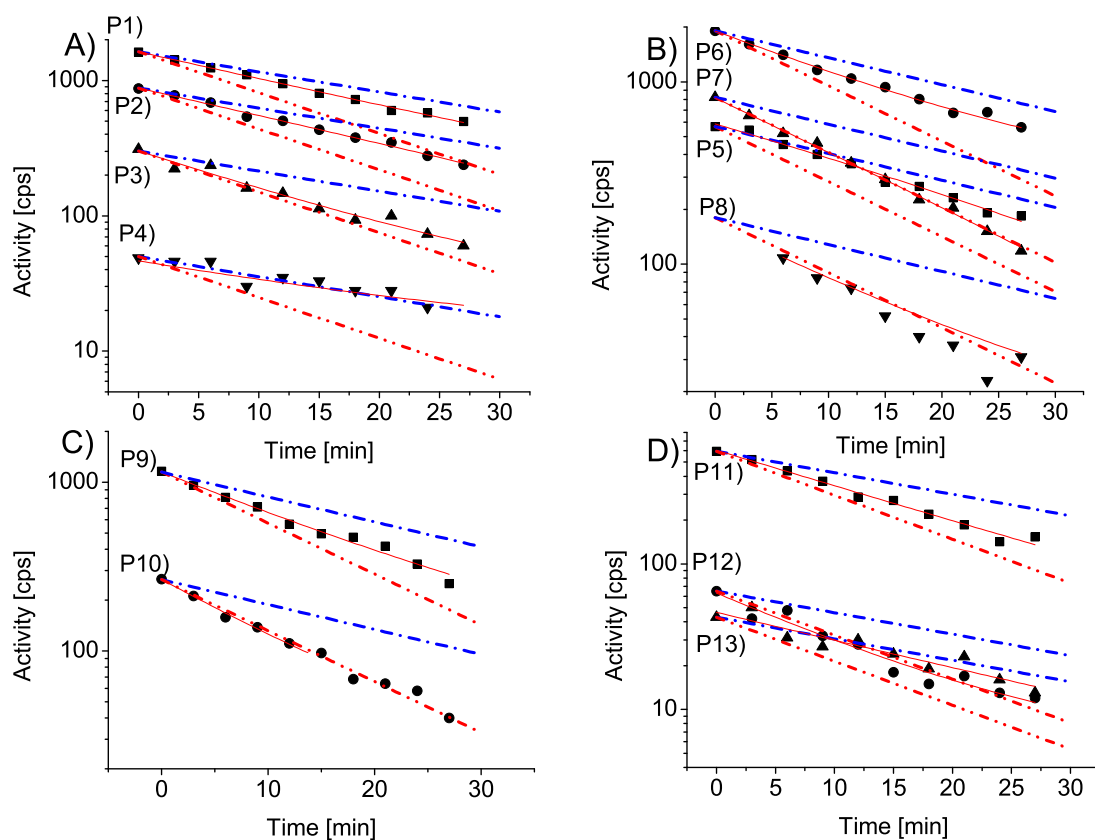


Figure 2.6: Individual half-lives associated with the positions, at which the corresponding peaks as fitted in the previous figure contribute mostly to the activity, can be seen in plots A-D. The experimental values are plotted with ■, ●, ▲ or ▼. The red and blue dash-dotted and dash-dash-dotted thick lines are the comparison with the half-lives of ^{11}C and ^{13}N , respectively. The solid red lines are the fitted decay of the experimental values.

For experiment B), the resulting chromatogram in Fig. 2.5 B), again four peaks P5–P8 can be assigned with corresponding Gaussian fits with T_{dep} as follows: P5 at 600 K, P6 at 550 K, P7 at 350 K and P8 at 210 K, respectively. From Fig. 2.6 B), the peaks are assigned as follows: The activity associated with P5 follows the ^{11}C decay, while P7 and P8 are attributed to ^{13}N , and P6 is ^{13}N following the rationale as in the previous experiment (the peak is overlapping strongly with P5 contributing to a decay in Fig. 2.6 B) that is not pure ^{13}N).

In Fig. 2.5 C) two Gaussian peaks, P9 and P10 have been fitted to the chromatogram with T_{dep} of P9 at 550 K and P10 at 350 K respectively. Fig. 2.6 C) shows that the activity in both peaks is dominated by ^{13}N , as expected after removal of CO and CO_2 (the removal is not 100 % leading to a slight mixture in the decay of P9). The three fitted peaks, P11, P12 and P13,

in the chromatogram seen in Fig. 2.5 D) have deposition temperatures of 550 K, 350 K and 265 K, respectively. P11 corresponds to P2, P5 and P9. P12 is ^{13}N as P3, P7 and P10 and P13 is due to ^{11}C like P4. The assignments for experiments C and D also clearly support the assignment of P2 and P6 as due to ^{13}N . The assignment of the ^{11}C peaks P1, P4, P5 and P13 are straightforward after the oxidation and separation steps. In experiment A, the target gas is presumably containing ^{11}C labeled CO and CO_2 , leading to P1 and P4. In experiment B, CO was oxidized to CO_2 , so that P5 and P1 are assigned to CO_2 (with consistent T_{dep} of 600 K). CO_2 is removed by the KOH trap and therefore mostly absent in experiment C. On the other hand P4 and P13, which have been removed from A to B by oxidation, are assigned to CO. Also in the case of CO, the deposition temperatures are consistent at 265 K. While in Fig. 2.5 all chromatograms are shown in normalized form, also the quantitative comparison clearly supports this picture. In terms of absolute numbers of counts, P5 (CO_2 in B) is slightly higher than P1 (CO_2 in A), because additional activity comes from oxidation of CO. Similarly, P13 and P4 (CO) have about the same peak areas. Since, NO does not significantly adsorb on these surfaces at the temperatures of this experiment we have always observed breakthrough of NO (i.e. ^{13}N derived activity) into the activated carbon trap at the outlet of the TC set-up. As mentioned above, the ^{13}N derived peaks are due to NO_2 and HONO. The situation for HONO is complicated because it can be formed from NO_2 in the TC column as well as on all other surfaces. Therefore, P2, P6, P9 and P11 are assigned to NO_2 , which is neither removed by the KOH trap from A to D, but slightly affected by thermal decomposition from B to C. The deposition temperatures for NO_2 are consistently at 550 K. On the other hand, the other ^{13}N derived peaks with adsorption temperature of 350 K (P3, P7, P10 and P12) are attributed to HONO. In experiment A) the HONO adsorption is due to HONO coming from the target gas together with the HONO formed in the TC column. Experiment B) contains the same contribution as in experiment A) and also the contribution from the production in the CuO oven and the further surfaces associated with the extension of the flow system. In experiment C) and D) the contribution of HONO is coming from the production directly in the TC column. Activity was also seen at the lower temperatures around 200 K. At this temperature, we expect that water (being present as impurity in our flow system with less than 200 ppm) is freezing on the TiO_2 surface. Such ice exhibits typically a very high surface to volume ratio, and might adsorb labeled NO. However, because the temperature gradient as well as the surface to volume ratio in this part of the column is not well characterized, no adsorption data have been deduced. The assignments of the molecules have been used to derive adsorption properties.

Table 2.1 shows a summary over the assignments of the peaks. Additional experiments have also been performed with different temperature gradients using the same method to assign the observed peaks. In an experiment done with T_{max} of 875 K and with a less steep temperature gradient, only one ^{11}C peak was detected with T_{dep} of 330 K, which was not affected by switching the CuO oven on/off but only by the KOH trap. A ^{13}N peak was identified with T_{dep} at 530 K. With a higher starting temperature, $T_{\text{max}} = 1475$ K and a steeper temperature gradient, again two peaks (^{11}C and a ^{13}N) were detected, identified as CO_2 at 670 K and as NO_2 with $T_{\text{dep}} = 603$ K. Activity was also seen at lower temperatures around 300 K, these peaks could not be identified due to the flattening temperature gradient. To summarize our observations, we note that all species CO, CO_2 , NO_2 and HONO have led to well defined peaks in the TC experiments (though with significant overlap of CO_2 and NO_2). The peaks

appear to be symmetric, which is an important prerequisite for the chromatographic analysis as explained below. We also note that with the exception of formation of HONO, we found no evidence of inter conversion among these species, as e.g. CO₂ to CO decomposition or CO to CO₂ oxidation. The determination of the deposition temperature (T_{dep}) in the column was determined to within a typical error of two σ (± 10 K) yielding an error ≤ 5 % for the adsorption enthalpy calculated with the mobile adsorption method.

2.4 Derivation of adsorption enthalpies

Two methods have been used to analyze the data summarized in Table 2.1. The first one is an analytical method based on classical linear gas chromatography, where the enthalpy is calculated with an iterative process. The second method is a Monte Carlo simulation of the processes governing migration of the molecules in the flow tube, i.e., transport and diffusion in laminar flow, adsorption on the surface and desorption from the surface. Both methods are described below.

2.4.1 Analytical method.

The analytical model is described in detail by Eichler and Zvára in [40]. The model is based on linear gas chromatography, assuming a reversible adsorption process and ideal behavior of the volatile species while they are transported along the surface. It assumes that equilibrium is established locally at every position, i.e., lateral diffusion is not influencing the process, and full partitioning between gas and adsorbed phase is established. The motion of the molecules in the column as a function of time can then be described with Eq. 2.1, where z is the distance, t time, u is the gas flow and k_i is the partitioning function.

$$\frac{dz}{dt} = \frac{u}{1 + k_i} \quad (2.1)$$

For an ideal gas, the temperature dependence of the carrier gas velocity is described by Eq. 2.2.

$$u(T) = \frac{u_0 \cdot T}{T_0} \quad (2.2)$$

Assuming a linear temperature profile along the column (which is a valid assumption for the region in the vicinity of the deposition temperature) and localized adsorption the following integral Eq. 2.3 is obtained that must be solved iteratively.

$$t = \frac{T_0}{gu_0} \ln \frac{T_{\text{dep}}}{T_S} - \frac{aT_0 \frac{V}{A} \exp\left(\frac{S_{\text{ads}}^0}{R}\right)}{vgu_0} \int_{T_S}^{T_{\text{dep}}} \frac{1}{T} \exp\left(\frac{-\Delta H_{\text{ads}}}{RT}\right) \quad (2.3)$$

Here t is the duration of the experiment, i.e. the time the gas with the radio labeled molecules was passing through the TC column. T_0 is the standard temperature (298 K), g the temperature gradient in the vicinity of the deposited molecules, u_0 is the linear gas velocity under

standard condition, T_{dep} is the experimental value of the deposition temperature, T_s the starting temperature of the local gradient, a is the surface area of the column under investigation, v is the open volume in the column. R is the ideal gas constant, A/V is the standard area to standard volume defined as $V/A=1$ cm [40], see also Table 8.1. To calculate the adsorption entropy ΔS_{ads} we assume a mobile adsorption model, i.e. three translational degrees of freedom in the gas phase and two translational and one vibrational degree of freedom (v_B) in the adsorbed state, (v_B) can be derived from the Lindemann [47] equation.

$$v_B = 2.8 \times 10^{12} \sqrt{\frac{T_m}{AV^{2/3}}} \quad (2.4)$$

The entropy of the ideal system can then be derived from Eq. 2.5 [40]:

$$\Delta S_{\text{a,mob}} = R \ln \left(\frac{A}{V} \frac{1}{v_B} \sqrt{\frac{k_B T_{\text{dep}}}{2\pi m}} \right) + \frac{R}{2} \quad (2.5)$$

k_B is the Boltzmann constant. All quantities other than ΔH_{ads} and ΔS_{ads} are known experimental parameters. The resulting ΔH_{ads} values are summarized in Table 2.1.

2.4.2 Monte Carlo simulations

Simulation of the chromatographic process with a Monte Carlo model has first been introduced by Zvara [41]. It tracks the path of an individual molecule along the chromatographic column by a series of subsequent randomized processes representing diffusion, adsorption and desorption, and radioactive decay. We have used the modified version of this approach as described in detail by Bartels-Rausch et al. [48]. The added value of the Monte Carlo method in the present context as compared to the analytical, static method explained above is that it can also reproduce peak shapes and takes into account diffusion in the gas phase. Lateral and axial diffusion in laminar flow are represented by a parameterized probability distribution of jump lengths between two wall encounters. This is determined by the flow velocity, the diffusion coefficient of the molecule in the carrier gas and its mean free path. Adsorption is described by the gas-kinetic collision rate with the wall (with an optional sticking probability), while desorption is represented by an activated desorption process. The latter is the central process determining the retention of the molecule. Its rate is related to the adsorption enthalpy by Eq. 2.6 [48].

$$t_r = \tau_0 \exp \left(\frac{-\Delta H_{\text{ads}}}{RT} \right) \quad (2.6)$$

τ_0 is the pre-exponential factor of the thermally activated desorption process. It is usually related to the vibrational frequency of the adsorbed molecule on the surface. This frequency is often assumed to be the same as the ground state phonon frequency of the solid substrate. We therefore chose $1.85 \cdot 10^{-13} \text{ s}^{-1}$ for TiO_2 . A simulation for an individual molecule is done by choosing random jump lengths, desorption lifetimes, and radioactive half-lives, and by repeating the series of adsorption and jumps until the duration of the experiment or the radioactive lifetime elapses. The position reached in the column is recorded and fed into a histogram representing the simulation for typically 10^6 molecules. The simulations were repeated with

different ΔH_{ads} until the histogram corresponded well with the experimental peak. In Fig. 2.7, we show the simulations for the peaks from the experiments explained above together with the chromatogram seen in Fig. 2.5 A. The ΔH_{ads} values estimated for the different molecules CO, CO₂, NO₂ and HONO from the Monte Carlo simulation compared well with those obtained by the static thermodynamic method, (see Table 2.1). The simulated peaks in Fig. 2.7 are 1.5 to

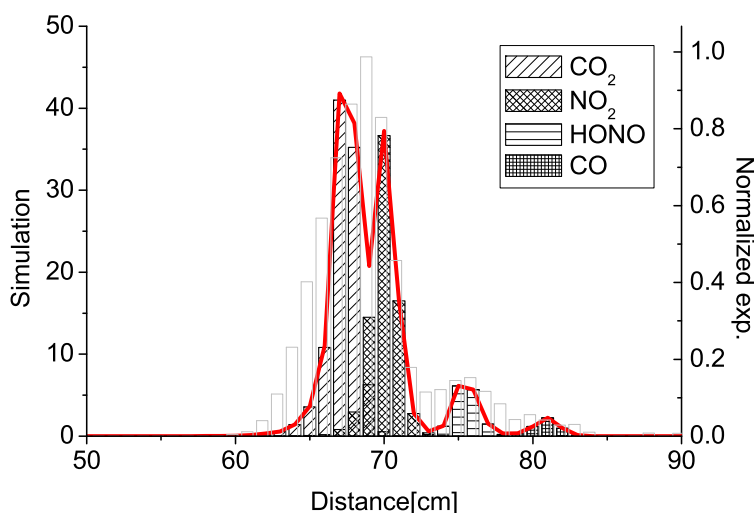


Figure 2.7: Simulation of the different peaks with ΔH_{ads} as shown in Table 2.1. CO₂ deposition with $\Delta H_{\text{ads}} = -142$ kJ/mol; NO₂ deposition with $\Delta H_{\text{ads}} = -130$ kJ/mol; HONO deposition with $\Delta H_{\text{ads}} = -82$ kJ/mol; CO deposition with $\Delta H_{\text{ads}} = -61$ kJ/mol. The amplitudes of the simulated distributions was scaled to the observed activity distribution which is shown as the grey histogram.

2.8 times narrower than the experimental peaks. The resolution of the detectors is probably the main reason for the broad peaks, caused by a ± 3 cm positioning error. Secondly, the simulation is assuming laminar flow and smooth surface conditions, while in reality the surface consisted of a powder coating that was not perfectly smooth. Moreover, because such a coating had a finite thickness, the molecules could have diffused to some degree into the powder film, which may have led to an additional broadening. When we performed the Monte Carlo simulations by assuming a distribution of adsorption sites varying by ± 5 kJ/mol, the observed peak widths could also be well reproduced. The slight tailing seen in Fig. 2.7 towards the higher temperatures is represented both in the experiments and the simulations and is due to the non-linearity of the temperature gradient.

2.4.3 Comparison with available data

So far, most experiments on the interaction of CO_x and NO_x with TiO₂ that were used to deduce interaction energies were Temperature Programmed Desorption (TPD) experiments. Also, a few theoretical studies are available. The reported experimental adsorption enthalpies

for CO are ranging from 25 to 117 kJ/mol [49, 50, 51, 52]. Those for CO₂ are ranging from 45 to 120 kJ/mol [51, 52, 53]; for NO₂ values from 53 up to 86 kJ/mol [54, 55] have been reported. The available theoretical values are between 71 and 146 kJ/mol for CO₂ [56] and 46 kJ/mol for CO [43], and between 100 and 160 kJ/mol for NO₂ [54], respectively. It becomes apparent that the enthalpies observed (or calculated) are strongly depending on the experimental procedure and conditions [57, 58]. Because the most useful catalytic activity of TiO₂ is evolving when Ti-sites are exposed at the surface of the TiO₂ (110) face in reduced valency, these adsorption studies were either done in presence of dopants or after annealing in vacuum or under reduced O₂ pressure. It is therefore clear that especially the weaker physisorbed states are different from those under our conditions, which were performed in presence of a significant partial pressure of O₂ pressure. We also note that in our experiment, we start from the high temperature side of the gradient system, so that the molecules end up in the adsorption states with the highest binding energy or activation energy of adsorption, which would be the most relevant one to determine retention in the high temperature environment of an ISOL target. Indications for this comes from the fact that CO was only observed as an adsorbed species with the two higher starting temperatures, while it passed through our setup at temperatures below 875 K, in which case the adsorption energy must have been below 70 kJ/mol. The same rationale applies for CO₂ that shows adsorption into the same adsorption state at the two higher temperature gradients, but in a state with a lower adsorption energy when starting at 875 K. On the other hand, the TPD experiments cited above typically start by first adsorbing the gas of interest at low temperatures (e.g. 100 K). The temperature is then gradually ramped up, while the adsorbed species start to desorb with the desorption rate at a given temperature determining the adsorption energy of the corresponding adsorbed state. Also, these TPD plots show a wide range of adsorption sites for the molecules discussed here. The range of reported adsorption energies as well as the range of energies reported here seem therefore consistent with each other and reflect the wide variety of possible adsorption sites and configurations on TiO₂.

Table 2.1: Experimental data used for the thermodynamical calculations of the adsorption enthalpy on TiO₂ surfaces.

Molecule	T _{max} K	T _{dep} K	Local grad. K/m	ΔS_{ads} $\frac{\text{J}}{\text{molK}}$	ΔH_{ads} $\frac{\text{kJ}}{\text{mol}}$	Comment
CO	1275	265(30)	-1150	-162	-61(8)	P4, P13
CO ₂	1275	600(80)	-2750	-161	-141(19)	P1, P5
NO ₂	1275	550(80)	-3000	-161	-130(20)	P2, P6, P9 and P11
HONO	1275	350(50)	-1800	-163	-82(12)	P3, P7, P10 and P12
(CO ₂)	875	330(65)	-1500	-161	-76(14)	Only seen in exp. A) & B)
NO ₂	875	530(65)	-1800	-161	-123(15)	
CO ₂	1475	670(200)	-3700	-160	-158(45)	
NO ₂	1475	603(200)	-3700	-160	-145(48)	

3

Thermochromatography studies on target unit materials

In the previous chapter the experimental and analysis methods to determine adsorption properties of relevant molecules under conditions relevant of an ISOL target (or similar), was described in detail. In this chapter results are described using the same methods for these molecules adsorbing on a range of materials considered for the target and the transfer line coating. Parts of this chapter has been published as: H. Frånberg, M. Ammann, H. W. Gäggeler and U. Köster, Chemical investigations of isotope separation on line target units for carbon and nitrogen beams, [59].

3.1 Target materials

The choice of materials to be studied was discussed in detail in the introduction chapter. For the target materials the basic alkaline earth metal oxides (BeO, MgO, CaO, SrO and BaO) were suggested. MgO and CaO are both materials used in the target for the production of different light radioactive ion beams as e.g. carbon and nitrogen. BeO is in principle also possible, but here only the spallation of oxygen would contribute to the production of carbon and nitrogen isotopes since beryllium has too low Z. SrO and BaO are being replaced by other metal oxides close in mass, where the chemical properties are more suitable, as will be discussed in the following chapters. The replacing metal oxide materials suitable for targets are Zr for Sr, Hf for Ba, U or Th. The calculated cross sections for carbon and nitrogen production (Fig. 1.7), suggest the use of MgO or CaO for the neutron deficient isotopes and heavier materials, such as TiO₂, HfO₂ or UO_x for the neutron rich isotopes. The chemical properties of the materials do have a large effect on the losses of the produced atoms (Chapter 1.5) on their way out of the target and through the transfer line.

3.1.1 MgO

The TC columns used for the MgO experiments were prepared in the same way as the TiO₂ TC columns described in section 2.2.2. MgO has a melting temperature of 3250 ± 20 K [60] which is well above the temperatures that the target would be operated at. The TC experiments were performed with different starting temperatures (from 570 K up to 1300 K) resulting in different temperature gradients (-8.55 K/cm up to -24.50 K/cm). The resulting chromatograms from the experiments performed with configuration A) to C) (explained in chapter 2.3) with T_{\max} of 570 K are represented in Fig. 3.1(a). Experiments were also performed with higher starting temperatures ($T_{\max}=873$ K and 1273 K respectively) with configuration A–D, shown in Fig. 3.2. Fig. 3.1(b) shows the decay of the different peaks from the chromatograms in Fig. 3.1(a). For the activity, from the radio-labeled molecules, adsorbed right at the entrance, higher temperatures would be needed to allow them to migrate, nevertheless twelve peaks were identified from Fig. 3.1 and the half-lives indicate a similar behavior of the adsorption properties as in the TiO₂ case. With the steeper temperature gradient (see Fig. 3.2) the adsorption peaks are moving down in the columns and are adsorbed at the same temperatures as with the weaker temperature gradient shown in Fig. 3.1; the adsorption sites are more concentrated in temperature resulting into visibly narrower peaks. The separation of the peaks is less evident in Fig. 3.2(a) and Fig. 3.2(b), therefore the assignment is still performed with the results seen in Fig. 3.1. The adsorption enthalpies are calculated as in section 2.4 and the assignment is summarized in Table 3.1. Using the same argument as in the previous chapter the identification of the peaks has been performed. P1, P2, P5 and P6 are following the ¹¹C decay, although P2 and P6 seems to have a contribution of ¹³N. P3, P4, P7-P12 are all following the decay of ¹³N. The first experiment A) was performed with the diluted, but untreated target gas, as described above. Further on, in experiment B) the diluted target gas was passed over the CuO oven for the oxidation of all CO to CO₂, prior to the TC oven. In the third configuration C), CO₂ was removed from the oxidized gas with the KOH trap. Finally in D) the diluted, untreated gas as in A) was passed through the KOH trap. Since there is no experiment D) shown in Fig. 3.1, the peak assigned as P1 adsorbed right in the beginning in Fig 3.1(a) is adsorbed at 800 K in Fig. 3.2(a) and Fig. 3.2(b), but is not seen in D) in respective chromatograms. The absolute activity in P5 is 30% higher than in P1, also P6 has a larger activity than P2 implying not only oxidation of CO to CO₂ but also an increased production of NO₂ coming from the CuO oven. This confirms a nomination of CO₂ to this peak. It is seen in C) that there is nothing left of the ¹¹C contribution. This shows that the oxidation of CO to CO₂ and retention of CO₂ is working. P2 and P6 might well be CO and NO₂. The quantity of the remaining ¹³N in P9 is less than a third of the activity measured in A and B. P4 and P12 are here being assigned to HONO.

3.1.2 CaO

This more basic alkaline earth oxide is expected to be a strong adsorbent of both CO and CO₂ molecules. For the TC experiments the columns were prepared in three different ways, firstly coated as in section 2.2.2. Secondly as the CaO targets are prepared in general at ISOLDE: from CaCO₃ that was mixed with ethanol and inserted into the column to form a smooth surface (Eq. 3.1). The entire column was then uniformly heated up to 1000 °C while

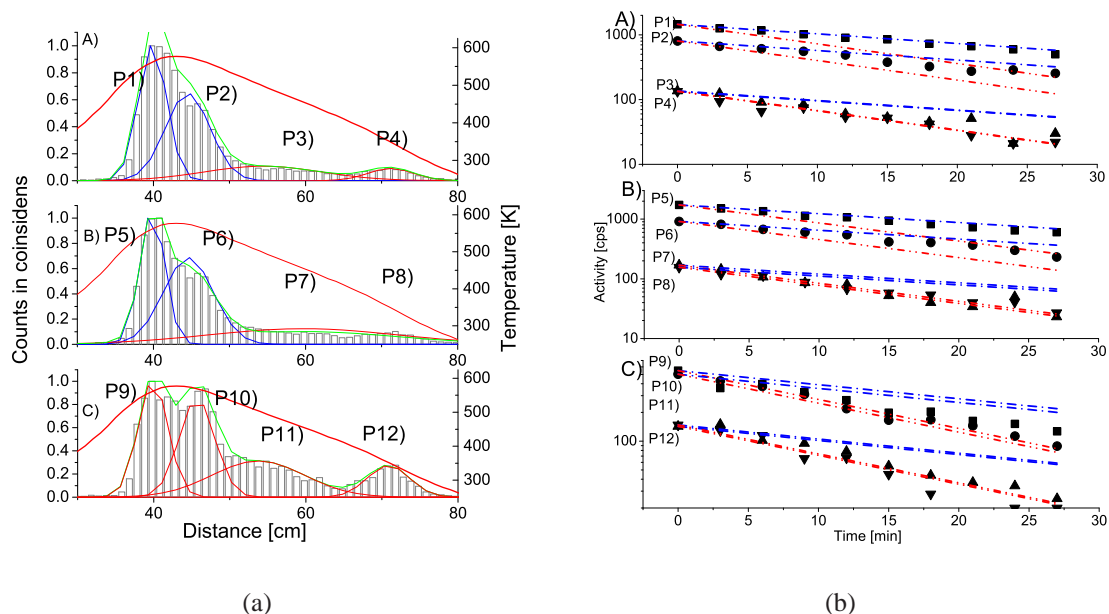


Figure 3.1: A), B) and C) for the figures corresponds to the same nomination as in the TiO_2 experiment, i.e. A) diluted gas experiment, B) is diluted gas after oxidation in a CuO oven and C) is the diluted, oxidised gas after removal of CO_2 in the KOH trap. The missing chromatogram D) is the diluted gas with the KOH trap. Figure a) shows the histograms of the TC experiments performed with T_{max} of 573 K. The temperature gradient is shown in red and is associated with the left y-axis. The Gaussian fits of the adsorption peaks are plotted in each chromatogram and have been numbered 1-12. Figure b) shows the individual half-lives associated with the positions, at which the corresponding peaks as fitted in the previous figure contribute mostly to the activity, can be seen in plots A-C. The experimental values are plotted with \blacksquare , \bullet , \blacktriangle or \blacktriangledown . The red and blue dash-dotted and dash-dash-dotted thick lines are the comparison with the half-lives of ^{11}C and ^{13}N , respectively.

Table 3.1: Experimental data used for the thermodynamical calculations of the adsorption enthalpy on MgO surfaces.

Molecule	T_{max} K	T_{dep} K	Local grad. K/cm	ΔS_{ads} $\frac{\text{J}}{\text{molK}}$	ΔH_{ads} $\frac{\text{kJ}}{\text{mol}}$	Comments
CO_2	900	770(20)	-21.5	-147	-164(5)	
CO	900	620(20)	-21.5	-146	-131(5)	
NO_2	900	620(20)	-21.5	-148	-132(5)	
HONO	573	350(20)	-21.5	-150	-76(4)	

a weak flow of N_2 gas was passing through the column. A CaO surface was obtained from

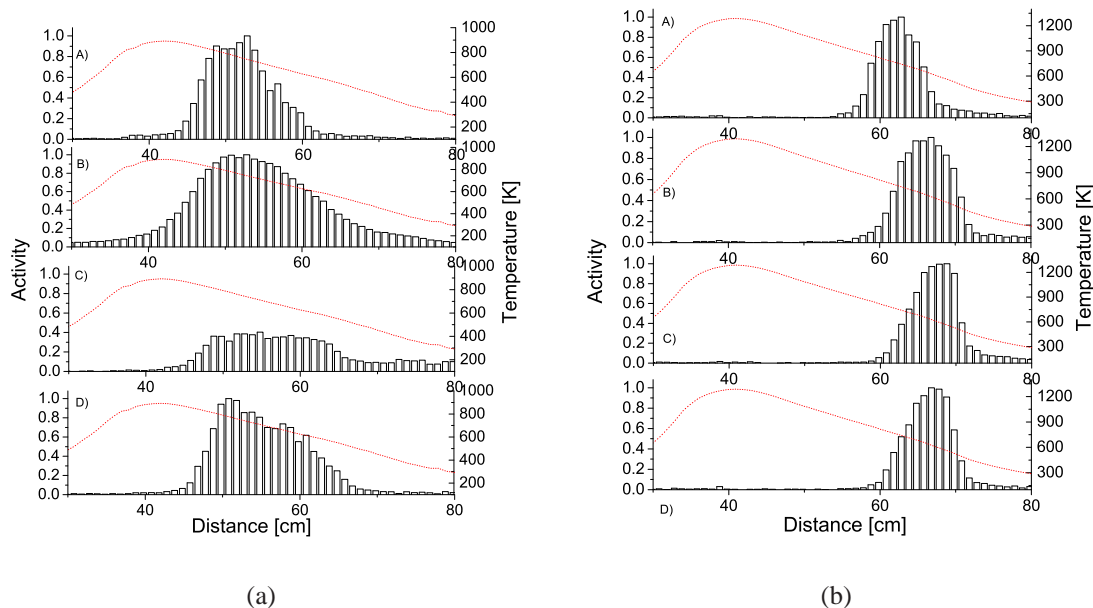


Figure 3.2: In the two figures with different starting temperature of $T_{\max}=873$ K in a) and $T_{\max}=1273$ K in b) the migration of the adsorption site in the column is obvious. The T_{ads} stays the same and therefore the peaks are also concentrated into a smaller surface area in the experiment with the higher starting temperature. In these chromatograms the labeling of the peaks is not shown due to the large uncertainty due to the small adsorption sites, making the fitting procedure very difficult. Although following the arguments for the experiment shown in Fig. 3.1 the nomination stays the same.

decomposition of the carbonate to the oxide and CO_2 ¹:



After the heating both ends of the tube were closed, inserted into the TC oven where again the tube was flushed with N_2 until the experimental gas was available. The third method consisted of CaO powder (commercial) mixed with SiO_2 bullets, with a diameter of 1-2 mm. The mixture was filled into the column and generated a larger surface ratio than the other two experiments. These three experiments led all to similar results, where the adsorption peaks are in the beginning of the column, the difference in the third experiment (not shown) with the narrower adsorption peaks is due to the larger surface to volume ratio. As soon as the carbon and nitrogen molecules come into contact with the CaO surface they were adsorbed to the surface. Unlike with the previous experiments on other substrates repeating this experiment with higher starting temperatures did not change the results. The purification of the column prior to the experiments was controlled by the ratio between the detected radio-labeled $^{11}\text{CO}_2$ and the non radio labeled $^{12,13}\text{CO}_2$ detected with the CO_2 analyzer before and after the column. Fig. 3.3(a) shows how the radio labeled molecules are adsorbed in the beginning of the column.

¹The melting temperature of CaO is at 3150 K.

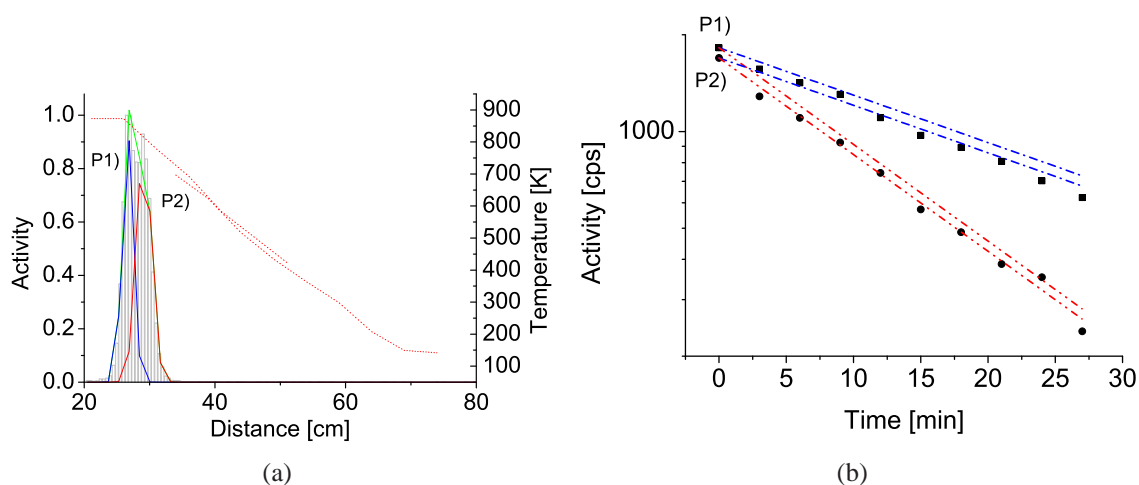


Figure 3.3: Chromatogram from the experiment performed with CaO coated quartz bullets in a quartz column. In a) the radio labeled molecules are all detected in the beginning of the experimental column, no signal is seen further down in the column. Two separate peaks are detected and shown as a red and blue line, the green line is the summary of the Gaussian peaks. The identification of the peaks is then confirmed in b). The experimental values are plotted with ■ and ●. The red and blue dash-dotted and dash-dash-dotted thick lines are the comparison with the half-lives of ^{11}C and ^{13}N , respectively.

There are two narrow peaks detected in the experiment with a maximum temperature of 873K. The first peak (P1) is from an ^{11}C -molecule, as seen in Fig. 3.3(b), and P2 is formed from a ^{13}N -molecule. Due to the peak positions only an upper absolute limit of 200 kJ/mol for the adsorption enthalpies could be calculated. The simulated values for adsorption for CO_2 and NO_2 with $\Delta H = -200\text{kJ/mol}$ are corresponding well with the peak positions as seen in Fig. 3.4. For the simulation a detailed temperature curve was used. Since the peaks are located in a range where the temperature curve flattens, the simulated peaks appear somewhat larger than the experimental ones. Following the signal from the detectors close to the chemical traps, parallel to and after the TC column, it is clear that no labeled molecules are coming through the column. The irreversible adsorption of NO_2 in the beginning of the column indicates that the formation of other NO_x molecules (see section 2.3) as observed on the other materials does not appear. This is also confirmed from the analysis of the activated carbon trap after the experiment where no activity is detected.

3.1.3 ZrO_2

Unlike the previously discussed oxides, zirconium is a metal of group four. It is used in the experiments as comparison to the alkali earth metal Sr. SrO has a higher base strength than CaO [61] and therefore zirconium oxide is more suitable as a target material for the release of nitrogen and the carbon molecules. A similar production from the cross section point of view is to be expected from the two materials. The increase of the CO_2 reactivity with the

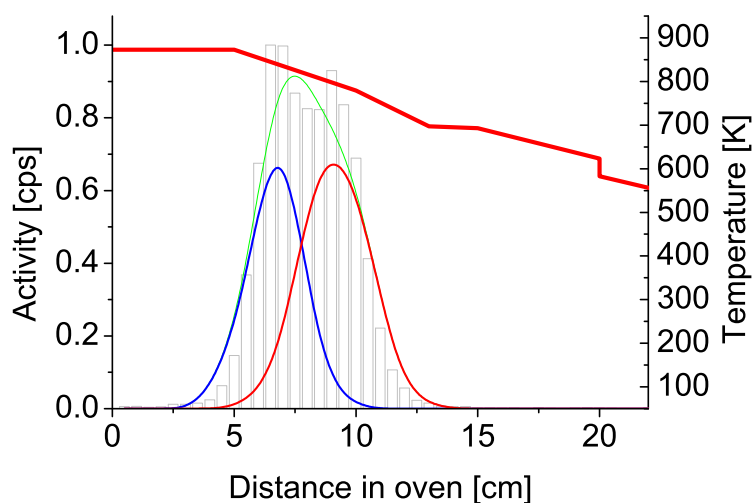


Figure 3.4: Chromatogram with CaO results from the TC experiment compared with a simulation of the adsorption peaks with $\Delta H \approx -200$ kJ/mol for the CO_2 (blue) and NO_2 (red) molecules. This corresponds well with the peak position analysis from Fig. 3.3(a).

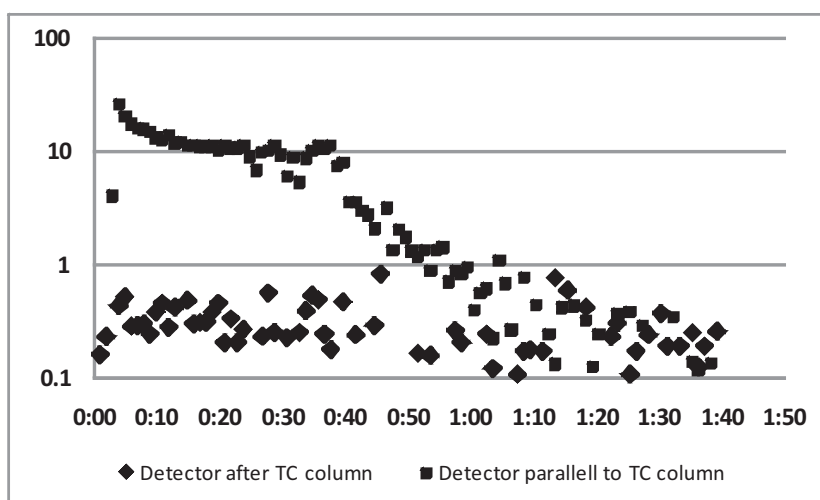


Figure 3.5: Activity in the chemical traps during the CaO experiment. \blacksquare denotes the detector signal from the trap parallel to the experimental column and \blacklozenge denotes the detector signal from the trap after the TC column. After 40 min. the experiment was stopped and no more gas was coming from PROTRAC.

alkaline earth oxide bases is expected and seen from the MgO and CaO experiments, and the heavier alkaline earth metals should be avoided. Zr most commonly occurs as ZrO_2 , with a melting point at 2950 K. With the ZrO_2 two different experiments were performed, one with a coated column, and one with fibre felt inserted into the column. When the fibre felt was used, the surface to volume ratio increased. In the experiment described here, the fibre felt

columns were used, as it led to narrower peaks used for the analysis. The chromatograms in

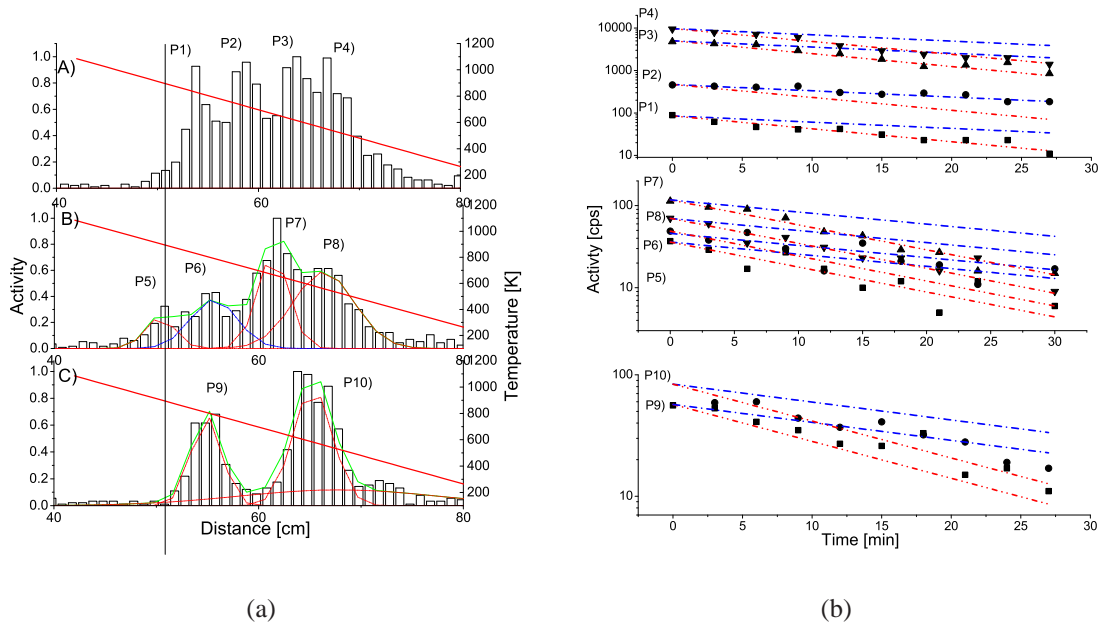


Figure 3.6: Chromatograms and decay of the individual peaks from the TC experiments performed with a ZrO_2 fiber felt inserted into a quartz column with $T_{\text{max}}=1073$ K. A) diluted gas experiment, B) is diluted gas after oxidation in a CuO oven and C) is the diluted, oxidized gas after removal of CO_2 in the KOH trap. In figure a) the temperature gradient is shown in red and is associated with the left y-axis. The Gaussian fits of the adsorption peaks are plotted in each chromatogram and have been numbered 1-10, in blue the peaks corresponding to ^{11}C -molecule and in red the peaks corresponding to a ^{13}N -molecule. b) shows the experimental values are plotted with \blacksquare , \bullet , \blacktriangle or \blacktriangledown . The red and blue dash-dotted and dash-dash-dotted thick lines are the comparison with the half-lives of ^{11}C and ^{13}N , respectively. In A) the peaks have the same relative intensity and therefore the decay spectrum has been weighted to be able to separate the different decays. The scaling of the peaks has been performed as $P1 \times 1$, $P2 \times 5$, $P3 \times 50$ and $P4 \times 100$.

Fig. 3.6(a) are from experiments with $T_{\text{max}}=1073$ K and with a temperature gradient of -19.0 K/cm. The three experiments A-C) are with the same configurations as in Section 2.3: The first experiment A) was performed with the diluted, but untreated target gas. Further on, in experiment B) the diluted target gas was passed over the CuO oven for the oxidation of all CO to CO_2 , prior to the TC oven. In the third configuration C), CO_2 was removed from the oxidized gas with the KOH trap. In Fig. 3.6(a) four peaks are observed in experiment A) and B), in C) only two peaks are observed, Fig. 3.6(b) shows the individual peak decays with time. The assignment of the peaks has been performed following the same arguments as in section 2.3, together with the results from Fig. 3.6(b). P1 and P4 show pure ^{13}N decay, P2 pure ^{11}C and P3 has a slow tail indicating it being a mixture of ^{11}C and ^{13}N . P5, P7 and P9 are pure ^{13}N while P6) consists mainly of ^{11}C . The two peaks P9 and P10 are dominated by

^{13}N activity as expected after removal of CO and CO_2 , although P10 seems to have a slow decaying tail and indicates therefore a contribution of ^{11}C . The assignment of the ^{11}C peaks is straightforward as in the previous sections, P2 is assigned to ^{11}CO at 725 K and when oxidized to $^{11}\text{CO}_2$ it deposits already at 800 K (P8). Both peaks are eliminated in Fig 3.6(a) C). In B) there is a ^{13}N peak seen at higher temperature, this can be due to a decomposition of the nitrogen compound within the CuO oven leading to a species adsorbing strongly in the ZrO_2 column. This species is then removed with the KOH trap, explaining that it is not detected in C). The NO_2 should be unchanged (not decomposed within the CuO-oven), this could also be the same activity as seen in A) before P1. The assignment of P1, P5 and P9 cannot be assigned to NO_2 since these peaks are not removed when the KOH trap that is switched in when changing from B to C. The remaining ^{13}N activities are therefore assigned to activity from HONO molecules generated from NO_2 via surface reaction. A temperature above 1000 K is recommended for the ISOL target to minimize the losses due to adsorption onto the ZrO_2 .

Table 3.2: The results of the adsorption enthalpy calculations on ZrO_2 surfaces.

Peak	Molecule	T_{max} K	T_{dep} K	Local grad. K/cm	ΔS_{ads} $\frac{\text{J}}{\text{molK}}$	ΔH_{ads} $\frac{\text{kJ}}{\text{mol}}$	Comments
P1	NO_2	1073	825	-21.6	-145	-174(5)	
P2	CO	1073	725(20)	-21.6	-145	-153(4)	
P5	N-(?)	1073	900(20)	-21.6	-146	-191(5)	
P6	CO_2	1073	800(20)	-21.6	-147	-170(5)	

3.1.4 HfO_2

Hafnium (Hf) belongs to the same group as Zr. There are five stable Hf isotopes ². Due to the large number of protons ($Z=72$) and neutrons Hf is suitable for the production of the neutron rich carbon isotopes. HfO_2 is the heaviest material that we have tested in our experiments. HfO_2 has a melting point of 3073 K. In the TC experiments with HfO_2 , the column was filled with a fibre felt material cut into thin strings as for the ZrO_2 experiments. The experiments were performed with different starting temperatures: $T_{\text{max}}=573$ K, 873 K and 1273 K. The resulting chromatograms (Fig. 3.7) show how the adsorption peaks move down in the column. In all three chromatograms a peak adsorbed at 400 K appears. In chromatogram B) and C) a peak adsorbed at 500-600 K appears, in A) this species is spread over a large temperature range. It is probably due to an activated chemisorption process that is triggered at temperatures above 500 K. For the higher starting temperature (as in C)) there is an increased decomposition of the species. This demonstrates clearly the importance of keeping the target at a temperature high enough not to have losses in the production target due to adsorption processes. Compared to the experiments on other substrates described above, the peaks appear narrower, possibly because of the very large surface to volume ratio of the felt material used for HfO_2 .

² $^{174,176,177g,178g,179g,180g}\text{Hf}$

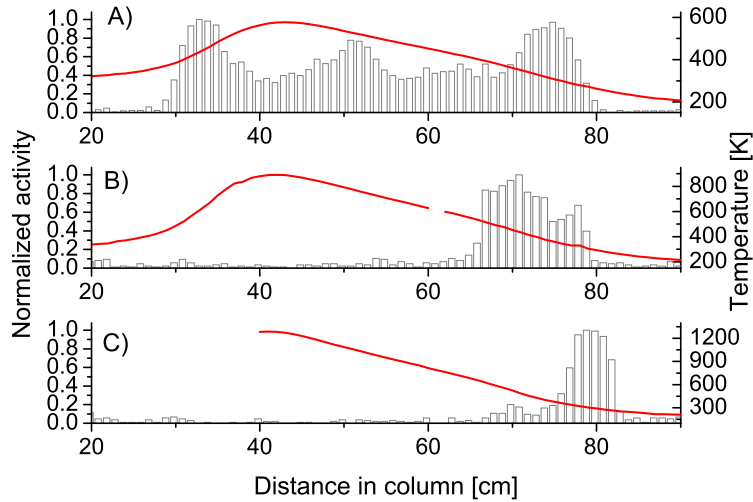


Figure 3.7: HfO_2 results from TC experiments. In the three figures the starting temperature (T_{max}) and thus the temperature gradient are different. Figure A) has a starting temperature of 573 K, figure B) has a starting temperatures of 873 K and finally in figure C) the experiment is performed with a starting temperature of 1273 K. The migration of the peaks in the column demonstrated that the adsorption temperatures stays the same.

Even though a multiple peak structure can be identified within the chromatograms it is difficult to separate the different adsorption sites. Fig. 3.8(a) and Fig. 3.8(b) show the resulting chromatograms from experiments with $T_{\text{start}} = 873$ K as starting temperature with the target gas (A) and with the CuO oven switched in to oxidize CO to CO_2 (B). In Fig. 3.8(a) A) only two peaks can be clearly fitted into the chromatogram while in B) three peaks are visible. Following the decay in Fig. 3.8(b) A) and B) the peak P1 is a mixture of ^{11}C and ^{13}N while P2 and P5 are clearly assigned to pure ^{11}C . P3, that is not seen in A), is dominated by ^{11}C and its quantity corresponds to the amplitude decrease from P2 to P5. Therefore $^{11}\text{CO}_2$ is assigned to P3 and ^{11}CO is assigned to P2 and P5. P3 and P4 are then due to NO_2 .

Table 3.3: Experimental data used for the thermodynamical calculations of the adsorption enthalpy on HfO_2 surfaces. Only the value for CO_2 has been calculated precisely. For the other molecules only a lower absolute value could be determined since most of the radio-labeled molecules pass through the column.

Molecule	T_{max} K	T_{dep} K	Local grad. K/cm	ΔS_{ads} $\frac{\text{J}}{\text{molK}}$	ΔH_{ads} $\frac{\text{kJ}}{\text{mol}}$	Comments
CO_2	700	600(40)	-17.6	-157(2)	-133(10)	
CO	380	300(30)	-12.0	-158(2)	-66(10)	
NO_2	600	450(40)	-17.6	-158(2)	-100(10)	

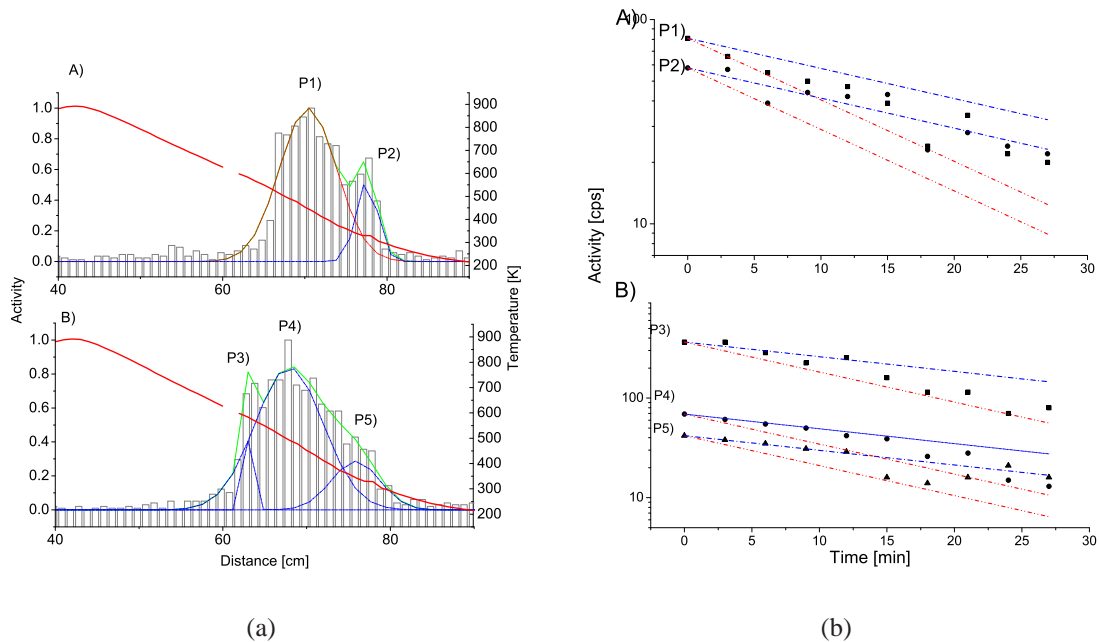


Figure 3.8: HfO_2 results from TC experiments. In the two figures the starting temperature is kept at T_{max} at 873 K. In Figure A) no oxidation prior to the TC column in figure B) the gas was oxidized in the CuO oven prior to experiments. In a) the red line is the temperature gradient associated with the left y-axis. The Gaussian fits of the adsorption peaks are plotted in each chromatogram and have been numbered 1-5, in blue the peaks corresponding to ^{11}C -molecules and in red the peaks corresponding to a ^{13}N -molecule. In b) the decay of the peaks is plotted with \blacksquare , \bullet and \blacktriangle . In B) the amplitude of the first peak (P3) was scaled by a factor five in the display. The red and blue dash-dotted and dash-dash-dotted thick lines are the comparison with the half-lives of ^{11}C and ^{13}N , respectively

3.2 Materials for the transfer line and source coating

SiO_2 and Al_2O_3 are no candidates for the production target material. At high temperatures they have a solid glass or ceramic like consistence, making the diffusion of the molecules out of the materials very long. As mentioned above C and N molecules may strongly react with hot metal surfaces that are frequently present in many ISOL target and ion source units. Instead solid SiO_2 (quartz) and Al_2O_3 are considered as rather inert materials withstanding high temperatures and are therefore suitable for the coating of the walls of the target container, the transfer line and, in some cases, the ion source. SiO_2 and Al_2O_3 are for example routinely used in plasma chambers of ECR (Electron Cyclotron Resonance) ion sources [62, 63, 64] providing a high secondary electron emission as beneficial side effect [65]. For the investigation of CO and CO_2 adsorption on SiO_2 and Al_2O_3 , plain and alumina coated quartz columns were used in the TC experiments performed. Different types of columns were used: either the columns were coated by mixing the Al_2O_3 or SiO_2 powder with alcohol which were used to cover the inner walls of a SiO_2 column (as described above), or a column filled with Al_2O_3 felt

was used. A SiO_2 column filled with SiO_2 splitters coated with SiO_2 powder was also used. Due to the expected low adsorption or chemisorption reaction enthalpies and therefore low adsorption temperatures, a cold TC set-up was used. The set-up, with a cold oven, consists of a copper tube inside of an insulating box; the entrance area is thermo-stated by methanol held at 233 K and the exit area is cooled by liquid N_2 (LN2) as above. The gas was passed through a column with the fixed temperature gradient of -4.0 K/cm. The set-up is described by T. Bartels-Rausch[34]. One experiment was also performed with the TC oven described in 2.2.1, with $T_{\text{start}} = 525$ K, while the downstream end was always cooled by LN2. The experiments were performed as explained in Chapter 3.2.3 using the set-up shown in Fig. 2.2. After the admission of labeled molecules was stopped, both ends of the TC column were sealed and the column quickly retrieved from the TC oven and immersed into a liquid nitrogen bath, to prevent migration of eventually desorbing molecules. The liquid nitrogen was covering the column during the whole scanning time.

3.2.1 Low temperature experiments on SiO_2

In the resulting chromatogram (Fig. 3.9(a)) from the experiment with a SiO_2 surface, the TC column was kept at temperatures below room temperature to reach retention times which are experimentally accessible (in the order of minutes) and thus to deduce the experimental adsorption enthalpies. At higher temperatures no absorption of ^{11}C and ^{13}N species was observed above background. The symmetric adsorption peaks are indicating that only reversible adsorption is observed in the low-temperature experiments and no chemical reaction. The adsorption spectrum was also simulated with a Monte Carlo method that gave good agreements. From Fig. 3.9(a) and 3.9(b) P1 and P2 are assigned to ^{13}N activities while P3 is coming from

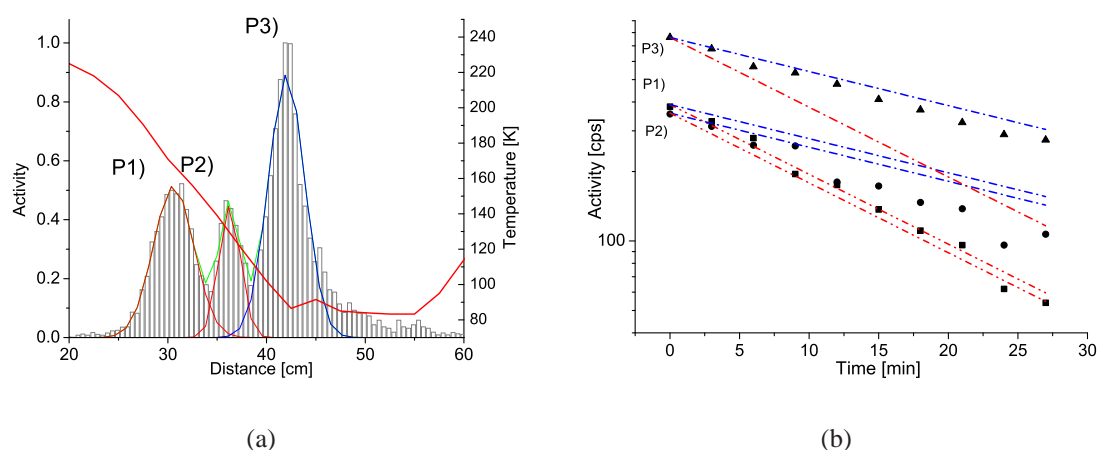


Figure 3.9: Thermo chromatography on SiO_2 powder coating inside a SiO_2 tube. In a) are the normalized adsorption peaks from the different molecules and the red line gives the temperature profile in the column. The measured individual half-lives are shown in b) together with the decay curves of pure ^{11}C or ^{13}N , respectively.

^{11}C . From the more advanced work on ^{13}N species on ice from T. Bartel-Rauch et al. in [34]

P1 can be assigned to HONO and P2 to NO_2 . From the complete experiments with SiO_2 (not shown) P3 can be assigned to $^{11}\text{CO}_2$.

3.2.2 NO_x and CO_x adsorption on Al_2O_3

In the experiment with an Al_2O_3 coated SiO_2 column, the adsorption peaks were observed at higher temperatures. An experiment was performed with the warm end of the TC column held at 525 K to cover a wider temperature range. The activity measured in the activated carbon trap after the TC column shows a mixture of ^{11}C and ^{13}N which means that most of the activity (of both ^{11}C and ^{13}N) goes through without significant retention in the column, likely in the form of NO and CO. From the analysis of the data with the CuO oven and/or KOH-trap in line with the TC-column the conclusion is that the adsorbed peaks come from $^{11}\text{CO}_2$, while ^{11}CO escaped through the column. On the other hand, the ^{13}N related activity comes likely from

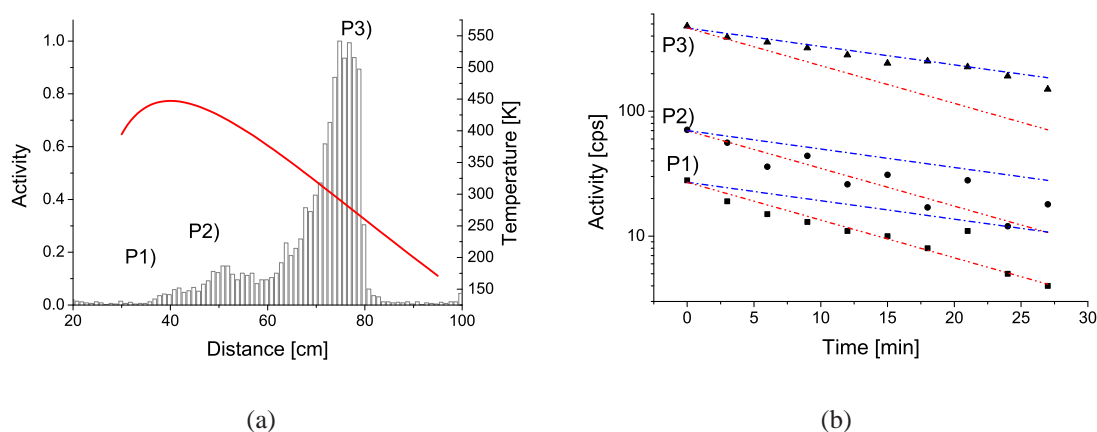


Figure 3.10: TC data from a run where the gas passed through an Al_2O_3 coated quartz tube. In a) are the normalized adsorption peaks from the different molecules and the red line gives the temperature profile in the column. The measured individual half-lives are shown in b) together with the decay curves of pure ^{11}C or ^{13}N , respectively.

NO_2 that has been oxidized from NO. NO_2 undergoes a chemisorption reaction with alumina [66] that may lead to the observed features at higher temperatures. Also the peak for CO_2 (P3) is now at higher temperature as compared to SiO_2 , consistent with the slightly more basic character of Al_2O_3 . The retention time of CO was not enough even at the lowest temperatures to be detected in our experiments. The Al_2O_3 experiments were also performed with fiber felt inserted into the quartz tube. In these experiments all radio-labeled molecules were detected in the activated carbon trap after the experiment. In spite of a higher surface to volume ratio the felt seemed less reactive for the adsorption than the powder coatings. This result probably means that there were channels within the column that the gas could pass through without diffusion through the fibre felt layer and the actual interacting surface was relatively small.

3.2.3 Discussion for SiO₂ and Al₂O₃ experiment

Table 3.4: A summary table of the experimental adsorption enthalpies on the different materials used in the experiments.

Surface	Molecule	T_s K	T_{dep} K	Local grad. K/cm	ΔH_{ads} $\frac{kJ}{molK}$	ΔS_{ads} $\frac{kJ}{mol}$
SiO ₂	CO ₂	200	100(20)	-6.5	-22(2)	-167(1)
SiO ₂	NO ₂	200	130(20)	-6.0	-29(2)	-167(1)
SiO ₂	HONO	200	170(20)	-6.0	-38(2)	-167(1)
Al ₂ O ₃	HONO	700	450	-1.0	-90(2)	-160(1)
Al ₂ O ₃	NO ₂	700	425	-7.5	-93(5)	-161(1)
Al ₂ O ₃	CO ₂	400	300	-5.0	-65(10)	-162(1)

A. Zecchina et al. [67] gave an estimate of around -21 kJ/mol for the chemisorption of CO on Al₂O₃ powder derived from infrared spectroscopy measurements. Their value agrees with the upper limit that we observed. Our result of CO₂ on Al₂O₃ agrees well with the theoretical study made by M. Casarin et al. [68], of -55 kJ/mol. C. Pazé et al. [69] investigated NO_x desorption from δ and γ Al₂O₃ surfaces. They did not quote an enthalpy value for NO_x on Al₂O₃ but their discussion is consistent with our results. TC experiments give results comparable with already established methods, for the adsorption properties at low concentration. It also has the advantage of providing information within a large temperature range within a limited time. The retention times for the materials treated in this last section are displayed in Fig. 3.11 compared to the average time it takes a ¹⁹C¹⁶O molecule to effuse one cm between two wall interactions. The retention time calculations of CO_x and NO_x molecules on surfaces of SiO₂ and Al₂O₃ was performed with Eq. 2.6. During the effusion of the molecules the species can "stick" to the wall for a certain time (τ_r) before desorbing. From this equation it is clear that the sticking time is longer for a higher absolute adsorption enthalpies. At room temperature the retention times of all studied species on quartz and of CO on alumina surfaces are negligible. However, for the CO₂ and the NO_x molecules on an Al₂O₃ surface the retention times become important below 670 K. In the example of CO₂ on CaO (a potential target material for the production of radioactive C and N isotopes discussed in detail in 3.1.2) the adsorption time at room temperature is extremely long so that for a significant reduction of the retention time for a rapid desorption from this material the temperature has to be kept well above 1000 K for the target.

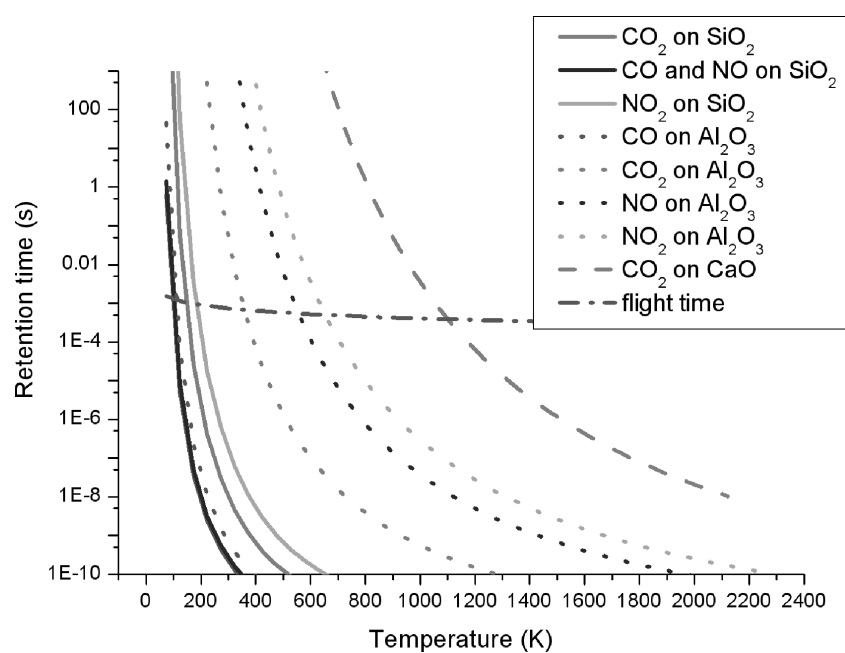


Figure 3.11: Average retention times for CO, CO₂, NO and NO₂ on SiO₂, Al₂O₃ surfaces, and CO₂ on a basic CaO surface compared with the average flight time over 10 mm for a ¹⁹C¹⁶O molecule at different temperatures.

4

On-line experiments

The importance of optimizing the materials in the target unit has been mentioned in the introduction chapter. The in-target production can be calculated when the cross-section of the production reaction is known. At ISOLDE the high energy protons lose only little energy when traversing a target and the excitation function is rather flat, i.e. the cross-sections do not show a strong energy dependence as e.g. in the case of fusion-evaporation reactions. Therefore to first order a "thin target approximation" is valid for an estimate of the in-target production as in Eq. 4.1:

$$P = I \cdot N \cdot \sigma \quad (4.1)$$

Here I is the intensity of the incoming proton beam (pps), N is the target density in number of atoms/cm² and σ is the average cross section (mbarn). To calculate the ion yield for the experiment, for each individual isotope, the efficiencies described with Eq 1.2 have to be considered together with Eq. 4.1 (cf. Chapter 1.5). When experimental cross-sections are not available one has to rely on calculated cross-sections. For our purpose we used two semi-empirical parameterizations that describe spallation and fragmentation cross-sections at high energies, namely the Silverberg and Tsao method described in [26] and the EPAX formula described in [27, 70]¹. With these two methods the theoretical production cross sections of carbon and nitrogen isotopes have been estimated for different target materials and are given in Fig. 1.7. In the figure the corrections for the different efficiencies discussed in Eq 1.2 have not been performed and the plotted values are theoretical, or best scenario values assuming loss-free release and ionization.

¹Brief description of EPAX and S&T

4.1 On-line experiment ISOLDE

To measure the yields and possible background at different masses for the production of radioactive short-lived carbon and nitrogen isotopes, an on-line experiment was performed with a standard ISOLDE target unit (cf. Fig. 1.2). From Fig. 1.3 it is clear that there are great losses in the production, it is now important to point out the areas where most of the losses occur for the construction of a more effective target. The target used was an ISOLDE MgO powder (supplier: Koch Light Industries) filled into a Re container and resulting in a target thickness of 2.7 g/cm^2 . The target was coupled to a FEBIAD ion source (see section 6.1.3) via a cold Cu transfer line. A calibrated gas leak² of $4.8 \times 10^{-6} \text{ mbar l/s}$ was connected to the transfer line directly after the target with two different gases: simple air and a pure nitrogen gas for comparison of the produced molecular sidebands. During the on-line run three different experiments were performed for the purpose of further TIS developments:

1. On-line yield measurements with the ISOLDE tape station,
2. Spectroscopy experiments with implantation and an on-line detector set-up
3. Collections for off-line diffusion measurements.

Experiment one and two were both for background identification and through the half-life dependency of the yield measurements identify different areas in the TIS unit that need to be developed for more efficient beam transport. The third method, where implantation of the beam and off-line measurements were performed is further described in chapter 5. The first yield measurements were performed with the ISOLDE tape station, yields for longer lived ($> 5 \text{ sec}$) isotopes were measured. The measurement was performed through β detection with a 4π plastic scintillator (sec. 4.2.2), the ISOLDE monitoring tape station is described by Lettry et al [71]. In the second experiment we used a spectroscopy setup on LA1 (Fig. 1.1) where the shorter-lived isotopes and the beta-delayed charged particles were measured. The ions were stopped in a thin carbon foil and the beta particles were detected by a 1 mm thick silicon detector and the alpha particles were detected in a $150 \mu\text{m}$ thick silicon detector. Each collection in the spectroscopy station was about ten minutes long. The on-line and off-line methods are described below.

4.2 Release time measurements

The measured release properties from the target unit is a collective release dependency of the diffusion, effusion and ionization. I.e. we cannot from this measurements alone find out what the different efficiencies of the different parts in the target unit is. The efficiency in the ion source can be measured off-line with similar conditions as the on-line experiments (Chapter 6.4).

²The gas leak was calibrated to N_2 with a pressure of 1.5 mbar.

4.2.1 Release measurements at ISOLDE

Every time a new target is put on the front end a yield estimation for the experiments is performed. This is a standard method for optimizing the individual settings for the target. A optimization of the release of the wanted isotopes with eventually suppression of contaminants can in some cases be performed. From the obtained release curves (as the one seen in Fig. 4.1 obtained from the MgO target) the release of the different isotopes, including activities of radioactive decay daughters can be fitted to find out the different release times. These release curves have been described in detail in many articles [72, 73, 74, 75, 76, 71, 6, 77], with the interpretation of the different parameters. Eq. 4.2 shows an empiric description of the observed release function [71]. At ISOLDE the proton beam is pulsed and the time between

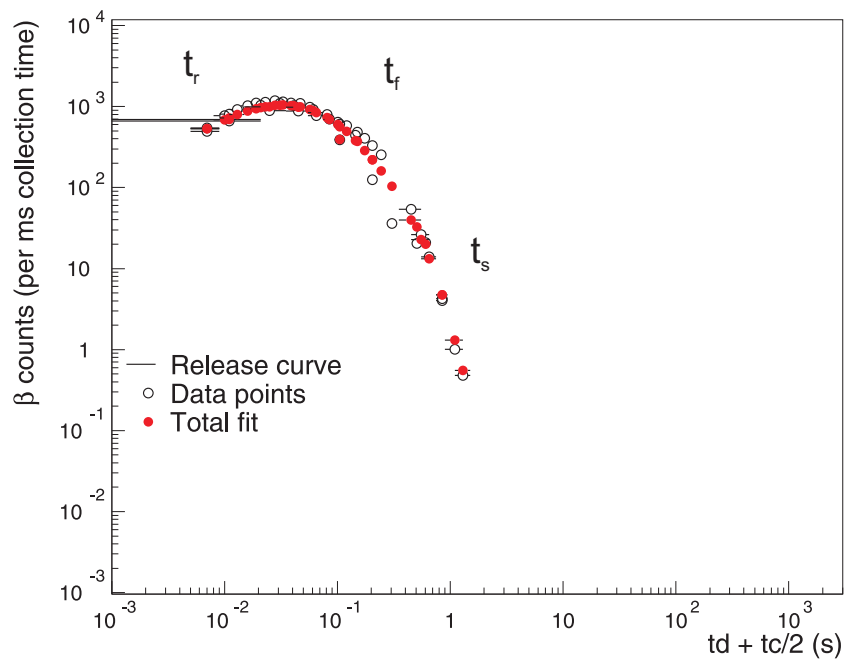


Figure 4.1: Release curve of ${}^6\text{He}$ ($T_{1/2}=806.7$ ms). The beam of ${}^6\text{He}$ is produced by having the proton beam onto the target for a time $t_d = 6$ ms, the beam gate is open for $t_c = 2$ ms where the beam is collected onto the tape. The tape is then transported to the detector and the beam is measured by the $4\pi\beta$ detector. The release is divided into three components, a rise time (t_r), corresponding to the effusion from the target to the ion source. The slow (t_s) and fast (t_f) decay times are each a convolution of diffusion out of the target and effusion to the ion source. In this case the best fit is as follow: $\alpha = 0.78(1)$, $t_r = 13.4(4)$ ms, $t_f = 52(2)$ ms and $t_s = 156(3)$ ms

each pulse can be controlled by the number of proton pulses per supercycle in the CERN PSB that are sent to ISOLDE. The yield measurements are performed by sending a proton pulse on to the target, the beam gate is thereafter opened and the isotopes can reach the tape station after a time t_d . During a time t_c , the beam is thereafter implanted onto the tape. The time t_d

can be varied as wanted between 0 ms and the time until the next proton pulse³.

$$R(t, \lambda_r, \lambda_f, \lambda_s) = A \cdot (1 - e^{-t\lambda_r})(\alpha e^{-t\lambda_f} + (1 - \alpha)e^{-t\lambda_s}) \quad (4.2)$$

A is a normalization to the measured intensity, λ_r is the characteristic rise time, λ_f is the decay component corresponding to the fast decay and then λ_s is the component describing the slow decaying tail. α is the relative contribution between the fast and slow component (λ_s and λ_f). In the case of He, which is a light noble gas the release time ought to be rather fast, as is the case in Fig. 4.1. In the case of carbon, which is a reactive element the release has been measured for CO. Since the CO molecule is volatile at room temperature and if there were no retention at the surfaces the release should be similar to the He release. We measured the release for the CO molecule (Figures 4.2 and 4.3) ^{10}CO with $T_{1/2}=19.25$ sec and ^{11}CO with $T_{1/2}=20.4$ min. In the comparison between the results in Fig. 4.1 with 4.2 and 4.3 it is clear that the release in the later one has a long lived tail. The expected similarity to the release of Helium is clearly not the case and the fitted release parameters shows that the release are rather long., and a retention due to diffusion or surface reactions within the target can be concluded. For the on-line studies, different mixtures of the carrier gas (air and oxygen) were used. No strong evidence was seen that one or the other would be more preferable for the formation of molecules or for the transport.

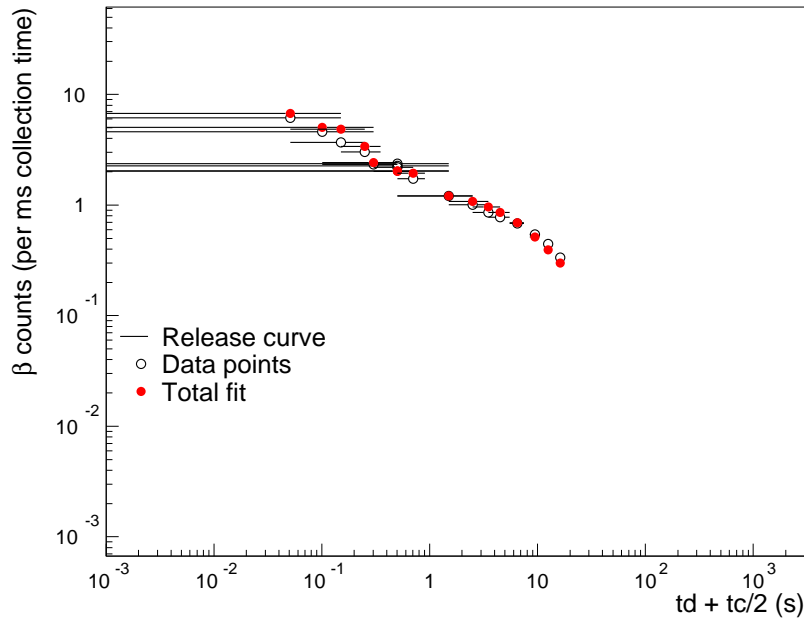


Figure 4.2: Release curve for ^{10}CO , $T_{1/2}=10.26$ sec. The fitted corresponding release parameters are $\alpha = 0.97$, $t_r = 25$ ms, $t_f = 57(6)$ ms and $t_s = 7.1(4)$ s. The release has a rather long slow decaying component compared to the ^6He decay, this is not due to a contaminant but to a slow release out of the target.

³The minimum time is 1.2 sec between the pulses. If a cycle of 12 destinations are used and one pulse of each cycle goes to the ISOLDE target station the time between two pulses is 14.4 sec.

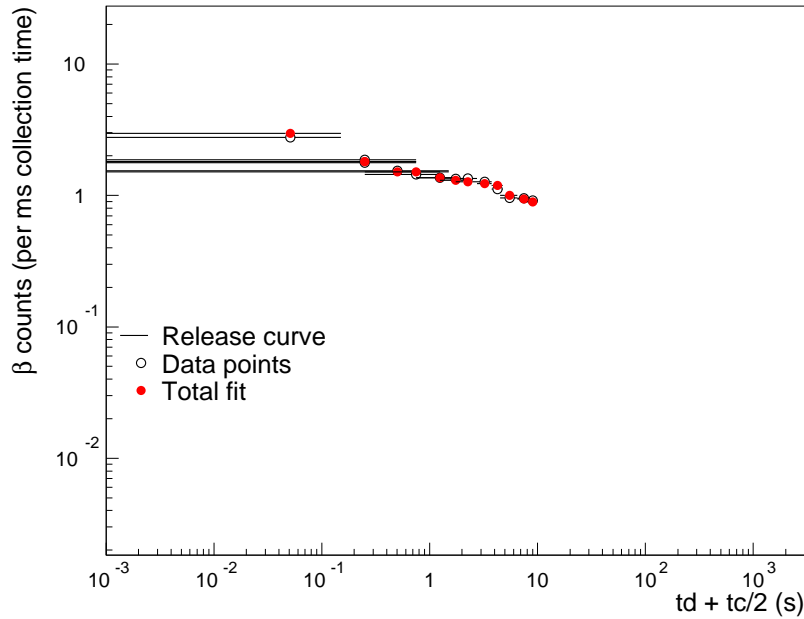


Figure 4.3: Release curve for ^{11}CO , $T_{1/2}=20.39$ min. The fitted corresponding release parameters are $\alpha = 0.74$, $t_r = 25$ ms, $t_f = 322(108)$ ms and $t_s = 18(5)$

4.2.2 Release calculations

We used three methods for release measurements. The first one is an on-line measurement and the two following consist of off-line measurements.

1. Implantations of a pulsed radioactive primary beam into the target. The produced secondary beam is detected (on-line) by following grow-in and decay of a characteristic gamma or beta decay. The curves are then fitted for determination of the release to known half-lives (as explained above).
2. A radioactive ion beam is implanted into a sample. The activity in the sample is then measured off-line. The sample is heated and the residual activity is measured. This method was used with ^{11}C implanted at ISOLDE with pressed metal oxide samples. Figure 4.4
3. RaBIT (Rapid p-Beam Irradiation Transport) irradiations, where a small quantity of a potential target material is directly irradiated with the proton beam. The sample is taken off-line and the produced isotopes are quantified through gamma spectrometry after thermal annealing. Figure 4.5

The most direct experiment for knowing the in-target productions is the RaBIT (Rapid p-Beam Irradiation Transport) measurements, this method gives information on the productions of isotopes that are generally not extracted from the target and are important in the development for new beams. An isotope with a relative long half-life, of the searched element is measured from samples at different temperatures. However, for the carbon and nitrogen, the only radio tracers with long enough half-life are the β^+ emitting ^{11}C and ^{13}N and the 511 keV line would not give us specific information for the production of one element at the time.

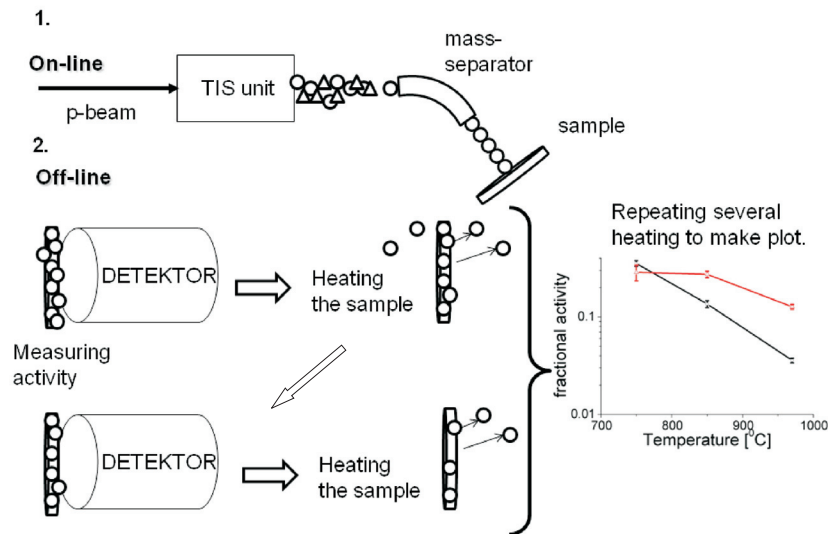


Figure 4.4: Release measurements off-line and on-line by implanting a radioactive beam into a stable target. A radioactive ion beam is implanted into a sample. The activity in the sample is then measured off-line. The sample is heated and the residual activity is measured. This method was used with ^{11}C implanted at ISOLDE with pressed metal oxide samples.

4.3 Background measurements

The background coming from the target was measured for different CO , CO_2 , NO and N_2 molecular masses. Detection and identification were performed analyzing the individual half-lives of the beta activity and by gamma-spectroscopy. The production of isotopes with $Z > 13$ is excluded with the choice of the target material. Therefore the effort has been put on identification of molecular beams with the same A/q ratio. An overview of the produced molecules in masses between 26 and 32 with possible background is listed below. Only the most common molecules are listed, i.e. when a radioactive isotope of carbon or nitrogen is bound to a stable isotope. Only the most abundant stable isotopes are considered for oxygen (^{16}O) and for nitrogen (^{14}N).

- Mass 26: $^{10}\text{C}^{16}\text{O}$ and/or $^{12}\text{N}^{14}\text{N}$ with $T_{1/2}$ of 19.3 s and 11.0 ms respectively. ^{10}C was clearly identified through its half-life and gamma lines. Nothing was seen of the fast decaying ^{12}N .
- Mass 27: $^{11}\text{C}^{16}\text{O}$ and/or $^{13}\text{N}^{14}\text{N}$ with $T_{1/2}$ of 20.4 min and 9.96 min respectively. They are both pure β^+ emitters and can only be separated through half-life measurements.
- Mass 28: Stable background of $^{12}\text{C}^{16}\text{O}$ and $^{14}\text{N}_2$. Production of $^{13}\text{O}^{12}\text{C}$ ($T_{1/2}=70.6$ s), ^{13}O decay via β^+ and can be detected through half-lives measurement with the tape station.
- Mass 29: Stable background of $^{13}\text{C}^{16}\text{O}$ and $^{15}\text{N}^{14}\text{N}$, same as for mass 28.

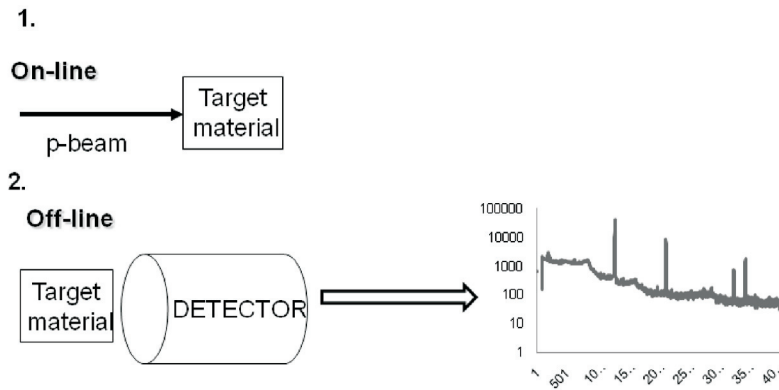


Figure 4.5: The most direct experiment for knowing the in-target production rates are so called RaBIT (Rapid p-Beam Irradiation Transport) measurements. A small quantity of target material is sent to the proton beam. After irradiation the diffusion out of the sample is measured.

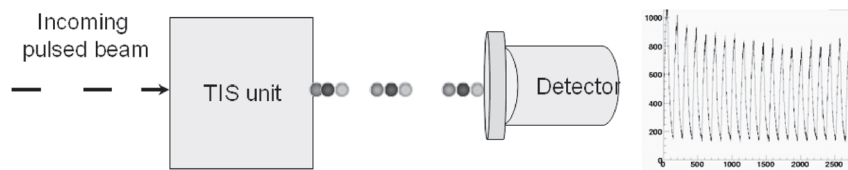


Figure 4.6: A stable primary beam is pulsed onto a target. The direct release with, grow-in (production) and decay (no beam on the target) can be measured through the characteristic gamma or beta decay. This method was used at GANIL.

- Mass 30: We detected a clear signal of $^{16}\text{N}^{14}\text{N}$ with half-life of 7.31 s and a characteristic gamma line at 6128.63keV. There is certainly also $^{14}\text{C}^{16}\text{O}$, but due to the long lifetime it was not detectable with our means.
- Mass 31: $^{15}\text{C}^{16}\text{O}$ and $^{17}\text{N}^{14}\text{N}$ with $T_{1/2}$ of 2.45 s and 4.17 s. ^{15}C can be identified and separated through characteristic γ -line at 5297.817 keV.
- Mass 32: Stable background of $^{16}\text{O}_2$. Radioactive $^{16}\text{C}^{16}\text{O}$ and $^{18}\text{N}^{14}\text{N}$ with $T_{1/2}$ of 747 ms and 630 ms respectively can not be separated with tape station through their half-lives but ^{18}N can be identified through the characteristic β delayed α spectrum.

During the on-line run with the MgO target at ISOLDE the most neutron rich isotopes detected were ^{16}C and ^{18}N . At this mass we could not identify the different isotopes with the use of the tape station only, therefore a spectroscopy station was set-up at LA1. At the spectroscopy station the $^{18}\text{N}^{14}\text{N}^+$ molecule could be clearly identify and quantified. Fig. 4.7 shows the β -delayed α -particle spectrum from ^{18}N taken during the run. ^{18}N is decaying to meta stable

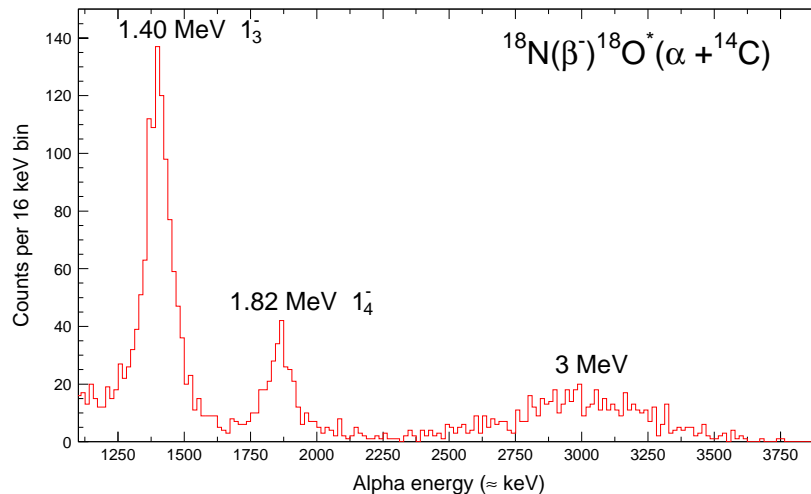


Figure 4.7: A spectrum of the $^{18}\text{N}^{14}\text{N}$ α -decay spectrum. Three α peaks are seen, 1.4, 1.82 and 3 MeV, the broad structure of the 3 MeV peak is from the physics point of view an interesting phenomena.

states of ^{18}O , which decays to ^{14}N via alpha emission as previously observed [22, 78] and more recently by [79, 80]. The spectrum in Fig. 4.7 is collected during only 10 min with a detection efficiency of 8%. This clearly shows the possibility to detect neutron rich nitrogen up to at least ^{18}N with a large stable background of O_2 and ^{16}CO . An overview of the decay properties of the carbon and the nitrogen isotopes is listed in Tables 9.4 and 9.5 in Appendix 9.1.

4.3.1 Results and conclusion

The actual experimental yields with the MgO-target are much lower than the calculated ones that are plotted for comparison in Fig. 4.8, (they are also listed in Table 4.1). The plotted

comparison shows directly measured and theoretical yields without taking into account the different efficiencies from Eq. 1.2.

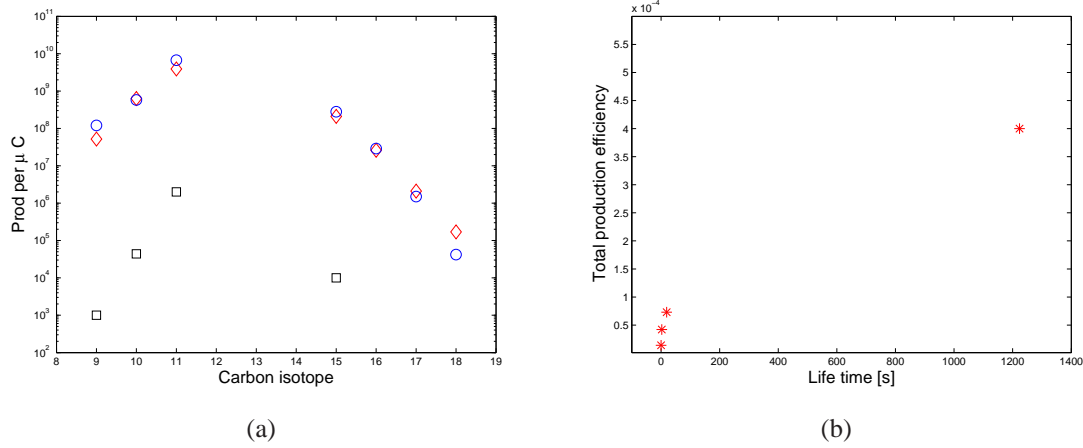


Figure 4.8: Calculated in-target production (atoms/ μC) and experimental carbon yields from a MgO mark 7 target with a cold transfer line of Ta and a Febiad plasma ion source. The carbon isotopes ($^9\text{--}^{11,15}\text{C}$) have half-lives of 126.5 ms, 19.3 s, 20.38 min and 2.45 s respectively. In figure [b] the total efficiency vs. the half life of the isotopes are plotted, a clear half-life dependency is seen.

Table 4.1: The production of carbon, neon and nitrogen in the experiment compared to the calculated estimations. The overall efficiency is calculate with the Silberberg and Tsao values.

Molecule	Mass	$T_{1/2}$ s	Measured yields [ions/ μC]	Comparison		Overall eff.
				S & T	EPAX	
^9CO	25	0.13	$1.0 \cdot 10^3$	$1.2 \cdot 10^8$	$5.2 \cdot 10^7$	1.4E-5
^{10}CO	26	19.3	$4.4 \cdot 10^4$	$5.8 \cdot 10^8$	$6.3 \cdot 10^8$	7.3E-5
^{11}CO	27	1223.4	$2.0 \cdot 10^6$	$6.7 \cdot 10^9$	$3.9 \cdot 10^9$	4.0E-4
^{15}CO	31	2.45	$1.0 \cdot 10^4$	$2.8 \cdot 10^8$	$2.1 \cdot 10^8$	4.2E-5
^{18}Ne	18	1.67	$3.2 \cdot 10^5$	$3.2 \cdot 10^7$	$3.1 \cdot 10^7$	1.0E-2
^{16}NN	30	7.13	$6.3 \cdot 10^5$	$1.2 \cdot 10^9$	$1.2 \cdot 10^9$	8.3E-3
^{17}NN	31	4.17	$7.0 \cdot 10^2$	$3.1 \cdot 10^8$	$2.5 \cdot 10^8$	3.6E-5

The losses are accumulating in the different steps of the production and transport and adding Eq. 1.2 and Eq. 4.1 we get the following equation:

$$Y = I \cdot N \cdot \sigma \cdot \epsilon_{\text{targ}} \cdot \epsilon_i \cdot \epsilon_t \cdot \epsilon_d \quad (4.3)$$

The overall efficiency ($\epsilon_{\text{targ}} \cdot \epsilon_i \cdot \epsilon_t \cdot \epsilon_d$) is not identical for all carbon and nitrogen isotopes, but depends strongly on the half-lives. We can first observe that even the noble gas isotope ^{18}Ne ,

that is not chemically reactive and will thus not suffer from losses due to adsorption has a relatively low overall efficiency. Since its release is relatively quick this can be mainly attributed to the low ionization efficiency of FEBIAD ion sources for elements with high ionization potential lighter than argon. In ref. [31] it was concluded that the ionization efficiency of a MK7 ion source for CO_2 to CO_2^+ is about six times higher than for Ne to Ne^+ . A similar ratio is expected for ionization of N_2 to N_2^+ . Thus, although the overall efficiencies are comparable for $^{11}\text{C}^{16}\text{O}$, $^{13}\text{N}^{14}\text{N}$ and ^{18}Ne , the release efficiencies for the former two are much lower. In the present target and ion source units at ISOLDE the effusing molecules can still come in direct contact with hot tantalum and graphite parts, namely the target container, the hot cathode of the ion source and the anode grid of the ion source. These surfaces can dissociate and getter irreversibly the radioactive carbon and nitrogen isotopes. The observed radioactive ion beam intensity is hence just the part that did not meet such surfaces on its random-walk effusion. The target container could be replaced by a chemically more inert material or coated/lined with such one as discussed in section 3.2.3. A modification of the FEBIAD source is more difficult since most high temperature electron emitters needed for an efficient cathode show the gettering effect. Therefore, for a major gain in release efficiency, a completely different type of ion source has to be considered, see below. The very promising results (^{18}N decay spectrum) under the present conditions that are far from optimum are already very encouraging for such a development. The significant drop of the overall efficiency for the $^{15}\text{C}^{16}\text{O}$ and $^{17}\text{N}^{14}\text{N}$ with respect to other isotopes of these elements with comparable half-lives cannot be explained by the half-life dependence of the release efficiency but is rather a sign of a systematic deficiency of the cross-section formulae to predict consistently the cross-sections for neutron-deficient and neutron-rich spallation products. Also the contribution of secondary reactions like $(n, \alpha xn)$ or (n, pxn) can lead to a relative enhancement of neutron-deficient isotope production in the thick target.

4.4 On-Line experiments at GANIL

The production yields and release efficiencies of short-lived carbon and nitrogen radioisotopes were measured on-line from several metal oxide targets at the ISOL separator SIRA (Séparateur d'Ion Radioactive) at GANIL (Grand Accélérateur National des Ions Lourds in Caen, France). Construction of a full size target for these tests is not only time and material

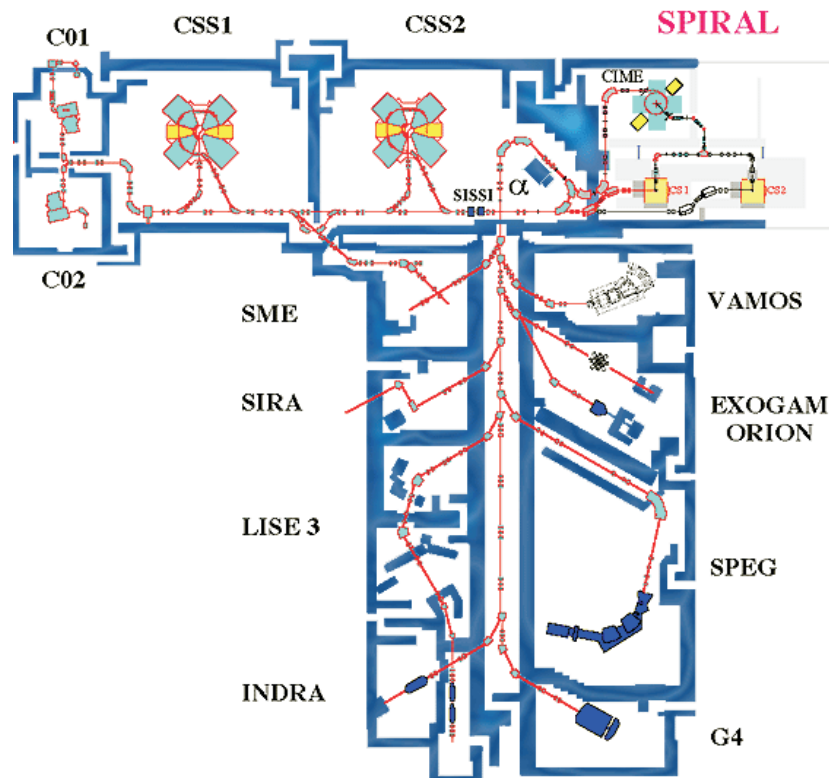


Figure 4.9: The accelerators and experimental areas at GANIL.

consuming but also the heavy target material are through fragmentation producing a multitude of long-lived radioisotopes which then is a concern for the storage of the target after the experiments. A target tester for the measurements of diffusion and release out of different targets was developed by F. Durantel during his diploma work [81] within the TARGISOL project. The target tester (Fig. 4.12) was installed at SIRA (Fig. 4.9). A projectile beam, produced at SISSI (Source d'Ions Secondaire à Supraconducteur Intense), was mass separated in the alpha spectrometer and sent to the ISOL target. The target tester consists of a target container wheel housing simultaneously up to twelve different targets. The target wheel was connected with an ECR (see section 6.2) ion source of type Mono 1000 (described by P. Jardin in reference [82]). A detection set-up consisting of a beta-detector (plastic scintillator) and a Ge detector for gamma detection is placed around a movable tape system behind the focal plane of a magnetic separator.

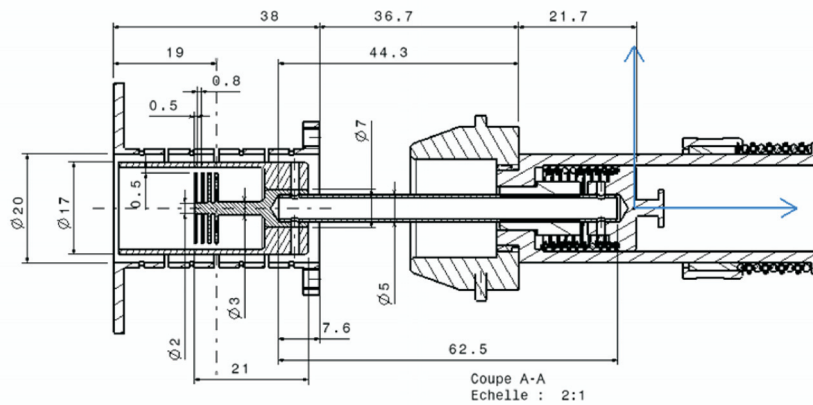


Figure 4.10: The standard target container used for the samples. In this figure the target is loaded with the GANIL carbon targets for tests. The target wheel and the TIS unit used at GANIL.

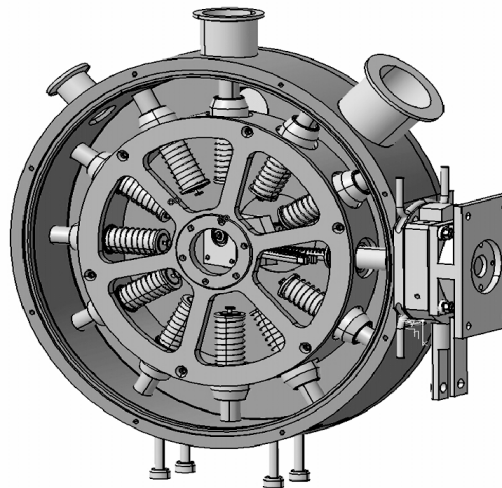


Figure 4.11: The GANIL target wheel with 12 positions for targets. One target is inserted into the heating oven at the right hand side of the wheel. The target is irradiated and the product is diffusing out the same way into the ion source.

4.5 Experiment

The goal of the experiment was mapping the on-line production intensities and release of carbon molecules from different target matrices and the temperature dependence of the release. The release time should decrease with rising temperature in the target unit due to faster diffusion and effusion, also the decay losses due to surface reactions or retentions should decrease with higher temperatures (Chapter 2). Four metal oxides were tested of two different types. Al_2O_3 , ZrO_2 and HfO_2 as fiber felts [31], HfO_2 and MgO were tested in the form of pills made out of pressed powder (the same type that was used in the ISOLDE diffusion measurements, the preparation of the pills are described in Appendix 9.1.1). All together five stations

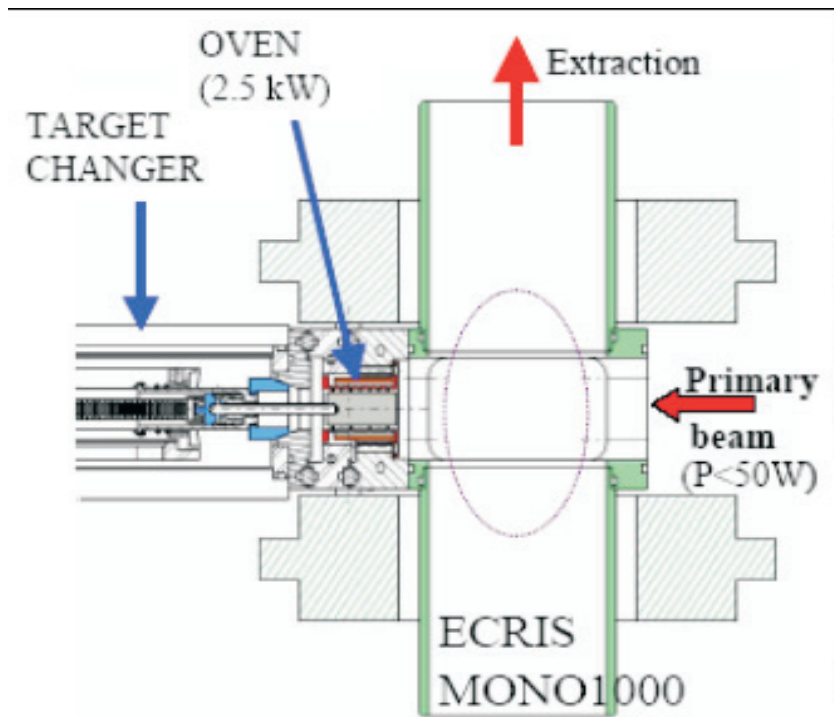


Figure 4.12: The GANIL target and ion source unit. On the left one of the targets, directly connected to the Mono1000 ion source at the right hand side of the figure. The beam is extracted orthogonally from the ion source.

out of twelve in the target wheel were dedicated to our experiment. The sample properties are listed in two tables: Table 4.2 is an overview over the five tested target materials and in Table 4.3 are listed the specifications of the fiber felts and the pills used in the targets. The standard

Table 4.2: Physical properties of the materials used during the on-line tests at GANIL. In the table the type of material used are listed together with the density of the material before and after sintering, the melting temperature (T_m), maximum temperature recommended during the experiments (T_{max}) and the characteristic sizes of the grains or fibres used.

Material	Type	Theor. density [g/cm ³]	Density after heating	T_m [K]	T_{max} [K]	Temp. 10 ⁻² mb [K]	Temp. 10 ⁻⁴ mb [K]	Size [μ m]
HfO ₂	Fibre	9.7	1.43	3050	2473	2575	2175	
Al ₂ O ₃	Fibre	4.0	0.41	2288	2173	2323	1200	
ZrO ₂	Fibre	5.7	0.58	2982	2473			6
HfO ₂	Pills	9.7	4.64	3047	2473	2575	2175	
MgO	Pills	3.6	1.86	3100	2273	1975	1575	

graphite target containers produced for the target wheel, were not suitable for our metal oxide

targets. Oxygen released from the target material would have reacted with the graphite and the container would become brittle and break during the manipulations. Therefore containers of molybdenum were specially constructed for this purpose. The target materials were all heated prior to the experiments for elimination of contaminants that would disturb the experiments and the stability of the ion source.

- MgO pills: The samples were sintered at 1490°C and 1700°C, no special remarks.
- HfO₂ pills: The samples were sintered at 1960°C and at 1700°C, no special remarks.
- Al₂O₃ felt samples: The samples were sintered at 1600°C.
- HfO₂ felt samples: Two heatings at 1600°C were performed.
- ZrO₂ felt samples: Two heatings at 1600°C were performed.

Table 4.3: The characteristics of the pressed pills of HfO₂ and MgO that were placed in the target holders for the tests

Material	Nr.	Radius [cm]	Volume [cm ³]	Mass [g]	Density [g/cm ³]
HfO ₂ pills:	1	0.58	1.04	1.298	1.25
	2	0.58	1.04	1.303	1.25
	3	0.58	1.06	1.364	1.29
	4	0.57	1.05	0.886	0.84
MgO pills:	1	0.52	0.83	0.237	0.28
	2	0.51	0.82	0.211	0.26
	3	0.51	0.81	0.149	0.18
	4	0.51	0.82	0.240	0.29
	5	0.51	0.81	0.248	0.30
	6	0.51	0.83	0.208	0.25
	7	0.51	0.81	0.228	0.28

A 25 MeV/nucleon ²²Ne beam was used as projectile during the tests. This relatively low beam energy had to be chosen for security reasons. The primary beam had to be stopped within the targets. Although the ¹⁰C had to be able to come out of the target. The different stopping ranges in the targets calculated with SRIM⁴ are shown in Table 4.4. The use of a heavier projectile like ³⁵Ar could produce contaminants at the masses that we were interested to measure and were therefore not a suitable alternative. A large range of elements were produced through fragmentation of both the projectile and the target materials. The fragmentation of the target materials produced heavier elements close to the metal and oxygen parts in the targets. The products were ionized and transported to the tape station for detection and identification. The release from the targets was measured at three different temperatures: 1200°C, 1500°C and 1800°C, with exception for the ZrO₂ target. Due to large out gassing from

⁴www.srim.org

Table 4.4: Stopping ranges of the 25 MeV/u ^{22}Ne and ^{10}C beam in the different fibre felt materials.

Material	Type	Density	Stopping range ^{22}Ne [mm]	Stopping range ^{10}C [mm]
HfO ₂	Fibre felt	1.43	5.9	7.2
Al ₂ O ₃	Fibre felt	0.41	12.8	16.0
ZrO ₂	Fibre felt	0.58	4.5	5.9

the target while heating, the ion source became unstable and the target temperature had to be limited to 1700°C. The intensities of $^{10,11,15,16}\text{C}$ beams were used to study the release through half-life dependencies, $^{10,15}\text{C}$ were identified through their characteristic gamma-lines following the beta decay. The release-time profile was studied with a pulsed primary beam. Carbon was dominantly found in the $^x\text{C}^{16}\text{O}^+$ sideband, which was about ten times stronger than the respective $^x\text{C}^+$ beams. Moreover we observed ion beams of short-lived nitrogen (mainly as $^x\text{N}^{14}\text{N}^+$ beams), neon and krypton isotopes.

4.5.1 Efficiencies

The ion source efficiency was measured by the means of continuous monitoring the current of $^{13}\text{CO}^+$ and $^{40}\text{Ar}^+$. The two gases were provided through a calibrated leak into the ion source during the experiment. The leak was calibrated for Ar flow with 7.2 μA . We calculated the $^{13}\text{CO}_2$ leak:

$$\Phi_{^{13}\text{CO}_2} = \Phi_{^{40}\text{Ar}} \sqrt{m_{[\text{Ar}]} / m_{[^{13}\text{CO}_2]}} = 6.8 \mu\text{A} \quad (4.4)$$

The ionization efficiency (ε_i) of the Mono 1000 [82] ion source varied between 18-33 % for CO^+ and was relatively stable around 39 % for Ar^+ . The total transport efficiency (ε_t) from the target to the Faraday cup before the tape station was 48 % and 27 % to the tape station, which gave a total efficiency of 5-9 % for the collections at the tape station. The detection efficiency as dependent on the energy, show both the efficiency when the collection is made directly onto the tape, Fig. 4.13, and using a "stopper plate" between the beam and the tape station, Fig. 4.14. The "stopper plate" was used to prevent the more intensive beams to damage the tape.

4.5.2 Results

The measured yields are listed in Tables 4.5, 4.6 and 4.7. An overview of the carbon and nitrogen production is given in Table 4.5. $^{10,11,15,16}\text{C}$ were observed in the $^x\text{C}^{16}\text{O}^+$ sideband, which was more than six times stronger than the respective $^x\text{C}^+$ beams. For the Al₂O₃ target the yield of molecular $^{10}\text{CO}^+$ compared to the elementary $^{10}\text{C}^+$ was observed to be more than 14-times higher. The large difference with the Al₂O₃ target is that larger part of the target was actually used for the production (Table 4.4), than in the heavier target materials as HfO₂ and

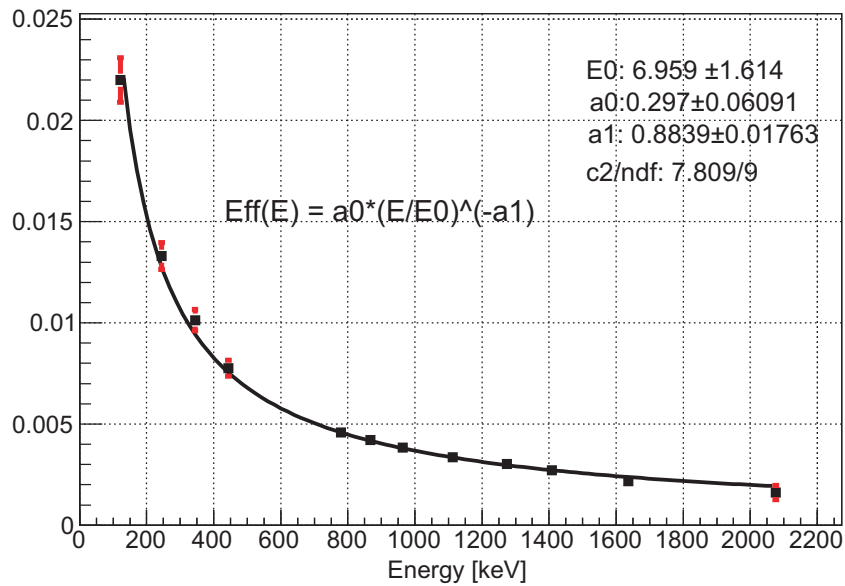


Figure 4.13: The efficiency of the Ge-detector used at the tape station

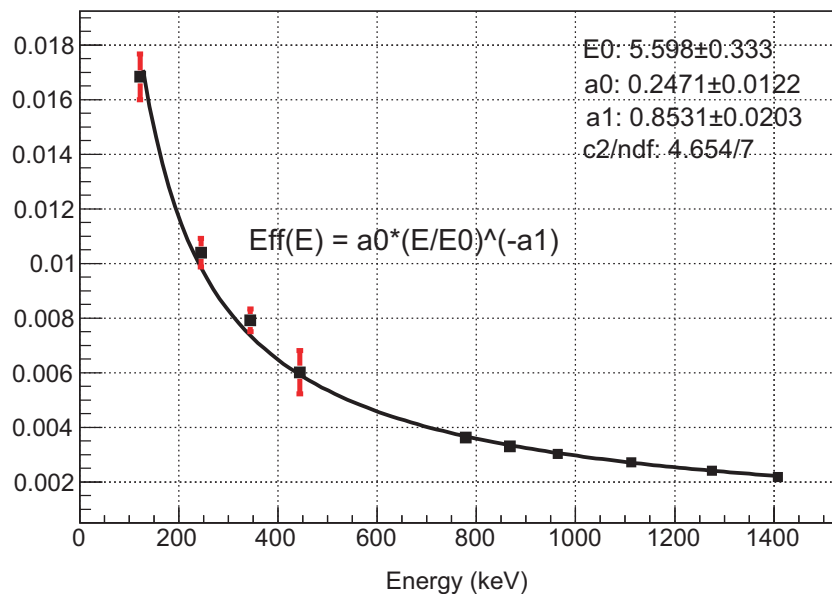


Figure 4.14: The efficiency of the Ge-detector used at the tape station using a stopper plate that reduces the intensity of the beam onto the tape

ZrO₂ where the primary beam was stopped rather early in the target. N₂ is only detected as ¹⁷N¹⁴N⁺ from the HfO₂ target with 67.8(17.8) part/s at 1200 °C, even ¹⁷NO is detected with 350(13) part/s with the same temperature and target. At T=1500°C the production actually went down for an unknown reason and 180(10) part/s is detected. At higher temperatures no nitrogen was detected from the HfO₂-target. The ion source was operated with a buffer gas of argon. At the beginning of the run residual nitrogen was present in the target and ion source unit. Due to continuous pumping the amount of available nitrogen dropped quickly

and with it the intensities of the observed ${}^x\text{N}^{14}\text{N}^+$ beams. Only in the very first experiment (HfO_2 at 1200°C) a ${}^{17}\text{N}^{14}\text{N}^+$ beam of measurable quantity was observed. Table 4.6 gives

Table 4.5: Production of carbon and nitrogen isotopes measured from different targets at different temperatures.

Target	Isotope	Yields [pps]		
		1200°C	1500°C	1800°C
HfO_2	${}^{10}\text{C}$	$7.98 \cdot 10^1$	$1.79(1.7) \cdot 10^1$	–
	${}^{10}\text{CO}$	$5.28(40) \cdot 10^2$	$1.26(18) \cdot 10^2$	–
	${}^{11}\text{CO}$	$5.64(71) \cdot 10^2$	$7.04(1.72) \cdot 10^2$	–
	${}^{15}\text{CO}$	$8.27(20) \cdot 10^2$	$5.54(23) \cdot 10^2$	$2.66(19) \cdot 10^2$
	${}^{17}\text{N}^{14}\text{N}$	67.8(17.8)	–	–
	${}^{17}\text{N}^{16}\text{O}$	$3.50 \cdot 10^2(12)$	$1.80 \cdot 10^2(9.76)$	–
ZrO_2	${}^{10}\text{C}$	$8.28(2.00) \cdot 10^1$	$1.16(27) \cdot 10^2$	–
	${}^{10}\text{CO}$	$5.92(49) \cdot 10^2$	$7.68(46) \cdot 10^2$	–
	${}^{10}\text{CO}_2$	–	$3.65(1.67) \cdot 10^1$	–
	${}^{11}\text{CO}$	$2.14(15) \cdot 10^3$	–	–
	${}^{15}\text{C}$	–	$1.38(8) \cdot 10^2$	–
	${}^{15}\text{CO}$	$1.04(2) \cdot 10^3$	$5.55(20) \cdot 10^2$	–
Al_2O_3	${}^{10}\text{C}$	$5.68(1.4) \cdot 10^1$	$3.45(1.31) \cdot 10^1$	–
	${}^{10}\text{CO}$	$8.46(39) \cdot 10^2$	–	–
	${}^{15}\text{CO}$	–	$8.09(18) \cdot 10^2$	–

an overview of most other isotopes produced except krypton that is listed in Table 4.7. We looked for Na, Ne and F production. Na is usually produced with a surface ion source due to the low ionization potential although Ne and F have rather high ionization potential (see further Chapter 6.4). The production of elementary fluorine is limited due to the high reactivity. The krypton isotopes are produced by fragmentation of the zirconium in the felt material. ${}^{75}\text{Br}$ was produced together with ${}^{75}\text{Kr}$ and due to the half-life of 96.7 min it was also clearly detected in the collections that followed. A major increase in the release was expected when the target was heated which was not observed. This means that the release from fiber felt samples is fast and the retention is negligible even at the lower (1200°C) temperature used for the targets during the test (as also been observed in chapter 2). The production rate of carbon from the different target materials is similar. This is probably due to a major carbon production from the ${}^{16}\text{O}$ atoms in the target. From the MgO and HfO_2 target pills release was negligible, probably due to the dense appearance due to sintering during the heating of the tablets. While using the ZrO_2 target, the ion-source became unstable, most likely due to major outgassing of the target. Therefore the temperature was limited to 1700°C for the experiments with the ZrO_2 target. When the source became stable the conditions had changed and the source efficiency went down, leading to a drop in intensity at the higher temperatures. The release of ${}^{15}\text{CO}$ and ${}^{16}\text{CO}$ (Fig. 4.17) was fitted to the decay curve achieved through gating on the detected beta energies.

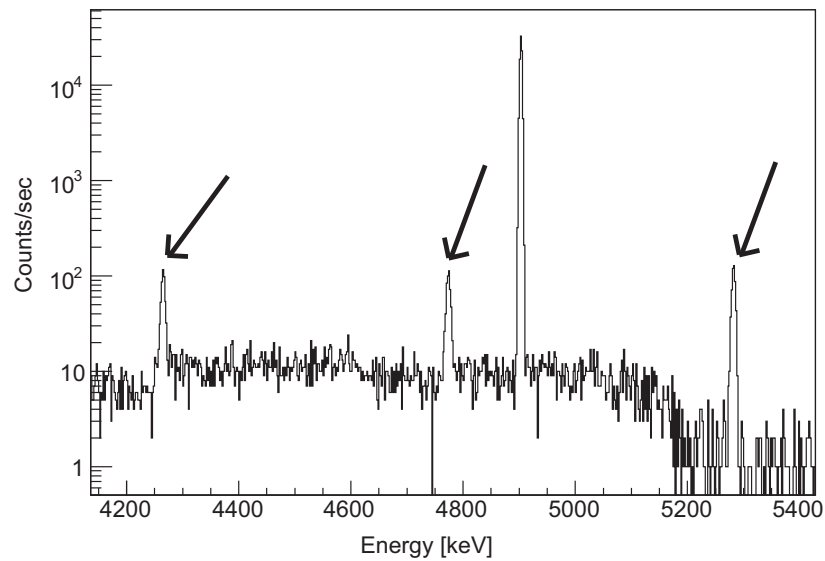


Figure 4.15: Gamma-spectrum for ^{15}CO from HfO_2 target at 1500°C after 28 minutes measuring. The characteristic gamma-line at 5298 keV with the two single and double escape peaks.

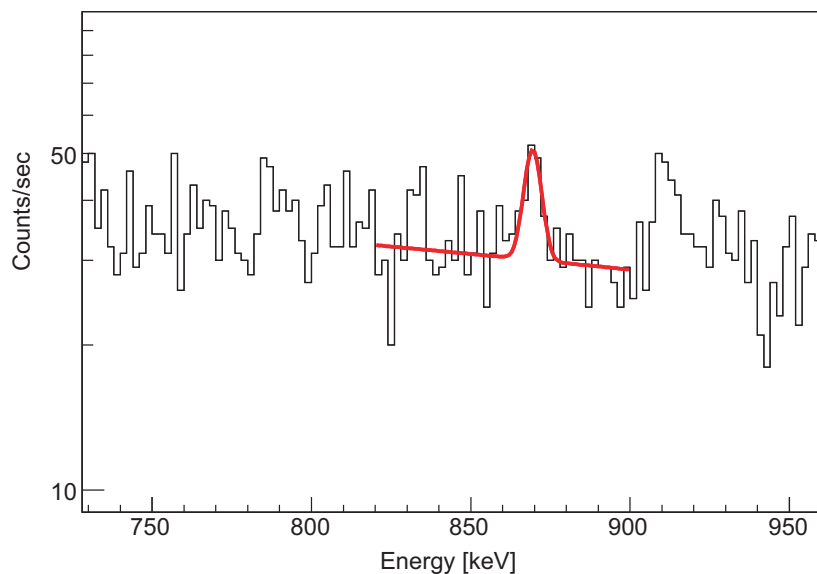


Figure 4.16: Gamma-spectrum for ^{17}NN from HfO_2 target at 1500°C after 28 minutes measuring. The 871 keV gamma-line from ^{17}N are fitted

4.6 Release measured with the GANIL targets

The release effects of the effusion vs. diffusion in the target was measured at GANIL where the ion source efficiency (ϵ_i) and the transport efficiency (ϵ_t) are well known. The large uncertainty in this case is the extrapolated production rate for a larger target in the future since the projectile beam energy during the tests was rather low (25 MeV). In this energy regime the

Table 4.6: Production of sodium, neon and fluorine isotopes measured from different targets at different temperature.

Target	Isotope	Yields [pps]		
		Temperature °C		
		1200	1500	1800 (1700 for ZrO ₂)
HfO ₂	²¹ Na		$1.0(6) \cdot 10^3$	
	²⁶ Na	$7.4(1.14) \cdot 10^1$		
	²³ Ne	$6.1(7) \cdot 10^5$	$6.8(6) \cdot 10^5$	$4.76 \cdot 10^4 (1.41 \cdot 10^2)$
	²⁰ F		$1.4(14) \cdot 10^2$	
	²¹ F			$2.37(5.60) \cdot 10^1$
ZrO ₂	²⁶ Na	$8.34 (7.5)$		
	¹⁹ Ne		$2.06(97) \cdot 10^3$	
	²³ Ne	$6.50(3) \cdot 10^5$	$5.46(5) \cdot 10^5$	$1.63(5) \cdot 10^4$
	²¹ F	$1.04(33) \cdot 10^2$		
Al ₂ O ₃	¹⁸ Ne	$2.11(2) \cdot 10^3$		
	²³ Ne	$2.10(6) \cdot 10^5$	$3.11(3) \cdot 10^5$	

Table 4.7: Production of krypton isotopes from the ZrO₂ target at 1500 °C.

Isotope	Yields [pps]
⁷⁵ Kr	$7.8 \cdot 10^1 ()$
^{79m} Kr	$8.03(16) \cdot 10^3$
^{81m} Kr	$8.80(14) \cdot 10^3$

semi-empirical predictions of fragmentation cross-section (EPAX-code) are no longer valid. The production of isotopes in mass regions far from target and projectile drops while the production of isotopes close in mass may even increase (through transfer reactions). The production yields achieved was anyway extrapolated to a full size target. If effusion would be the major reason for losses through retention in the target, the release extrapolation to a full size target, would not be correct due to the larger distances and surface to volume ratio. In Fig. 4.19 the release measurements of the beginning when the projectile hits the target is compared with the release after 50 minutes to see how the release from the target changes with time. No obvious difference in the release is seen except that the latter seems to have higher intensity which is due to an increasing background and not directly related to the release of the carbon molecule.

4.7 Discussion

The production was initially quite similar from the three different fibre targets although for the light elements the Al₂O₃ was more efficient. This is most probably due to that a larger part

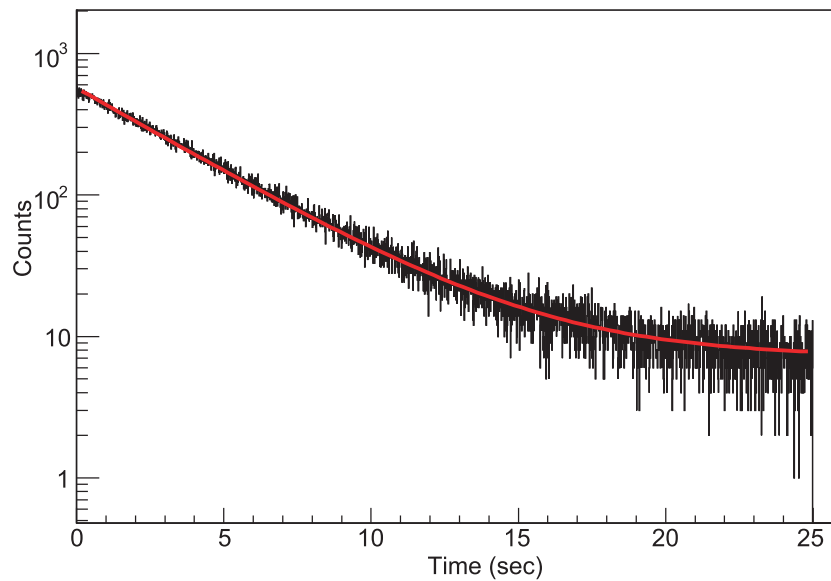


Figure 4.17: The fitted half-lives of ^{15}C with $T_{(1/2)} = 2.45$ s, produced, ionized and transported as $^{x}\text{CO}^{+}$

of the target that was used for the production. The other surprising result, a decrease in the production yield with higher temperatures, is most probably due to a decrease in the efficient target material with time. The targets used for the tests are miniatures of the targets that would be used for a large scale experiment. It is seen that for the fiber felts we have fast effusion of the products and we cannot detect a difference in the release time between a CO molecule and a noble gas as in the powder targets used previously at ISOLDE (Fig. 4.1 and 4.2 and 4.3). This means that the use of a ZrO_2 or a HfO_2 fibre felt target at ISOLDE would not only increase the production of the neutron rich carbon isotopes but also provide a more efficient effusion out of the target and therefore less losses for the relatively short-lived isotopes. At GANIL where the current interest is more for the Kr beams the use of a full size oxide fiber target at SPIRAL would allow to boost the beam intensities observed at SIRa by about two orders of magnitude: above a factor ten for higher effective target thickness when going to 95 MeV/nucl. Instead of 25 MeV/nucl. and a factor around ten for higher primary beam intensity. The target fragmentation of a ZrO_2 fiber target bombarded with ^{12}C would moreover provide higher intensities for neutron-deficient Kr beams than available today from ^{78}Kr projectile fragmentation.

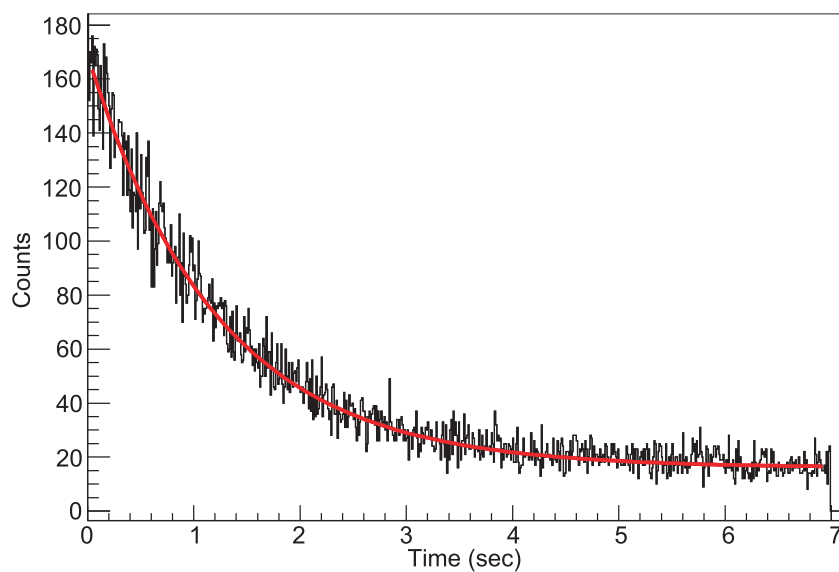


Figure 4.18: The fitted half-life of ^{16}C with $T_{(1/2)} = 747$ ms, produced, ionized and transported as $^{x}\text{CO}^{+}$.

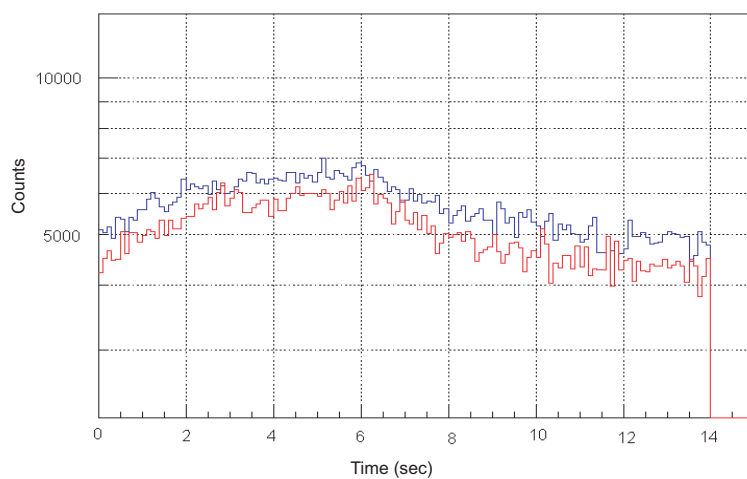


Figure 4.19: Comparison of the release out of a target. The comparison is done between the first release measurements out of a target and the release measurements taken at a later time from the same target. The measurements were performed with ^{19}Ne .

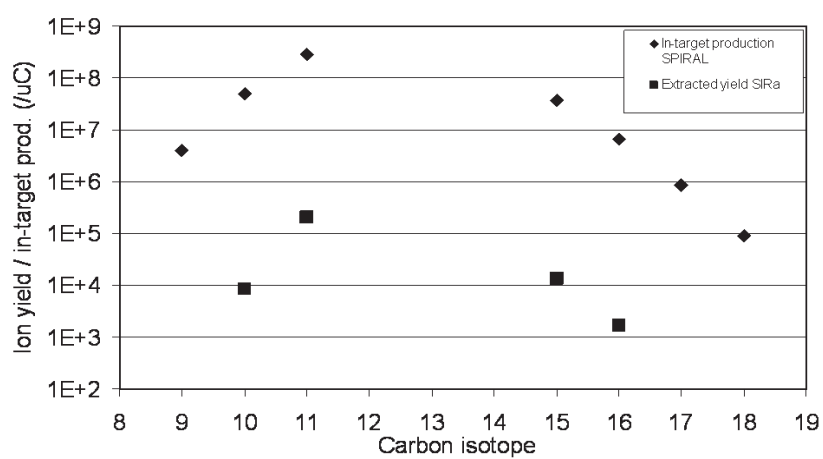


Figure 4.20: Comparison between in-target production SIRa test and calculated yields from a upscaled GANIL full size target. This is showing the possibilities of carbon production in a future facility

5

Diffusion measurements

When the isotopes have been produced within the target material it needs to diffuse out into the target container, to optimize the experimental ion yields it is necessary to investigate the diffusion out of different potential target materials in order to choose the most suitable one. On-line experiments as described above gives information of the general functioning of the TIS unit. The off-line measurements described here gives a signature of the diffusion out from the different target material itself. For this purpose implantations into different target materials were performed. The materials used was: MgO, TiO₂ and HfO₂ pressed powder samples and a fibre felt sample of HfO₂. Due to the natural background of ThO₂ and UO₂ these materials could not be studied without causing an excessive background. The diffusion of an element out of a structure is element dependent and not isotope dependent. Therefore these off-line measurements are performed with isotopes with a half-life of several minutes. For our purpose our only possible choice is ¹¹C with T_{1/2} = 20.4 min. It was produced and separated as ¹¹CO⁺ at the general purpose separator at ISOLDE. The preparation of the pills are described in Appendix 9.1.1. Details of the samples are given in Table 5.1.

Table 5.1: Characteristics for the pressed powder pills and fibre targets used for the implantations of ¹¹CO. For all materials a Ta boat was used for the heating.

Material	Structure (K)	Melting point g/cm ³	Density	Supplier
MgO	Powder	3098	3.6	Alpha Aesar
TiO ₂	Powder	2116	4.17	Fluka AG Buchs SG
HfO ₂	Powder	3073	9.68	Alfa Aesar
HfO ₂	square felt	3073		
HfO ₂	felt	3073		

Implantation method

There are three implantation stations available at ISOLDE. Two of the stations GLM (general low mass) and GHM (general high mass) are placed after the GPS separator (general purpose separator) and are used for implantation energies up to 60 keV. The third implantation station, situated at a high voltage platform are for implantation energies up to 260 keV. The high voltage platform can be reached with beams from both GPS and HRS (high resolution separator). At the implantation points the beam is primarily sent through a collimator for focusing onto the sample, the sample size is in general 1 cm². The stations are opened up to atmosphere for manually insertion of a sample holder with a capacity of up to ten different samples, the chamber is then closed and pumped to a pressure of 10⁻⁶ mbar. The ions produced, ionized and separation are implanted into one samples at the time, several samples on the holder can be used for implantation one after the other if wanted. The holder is then taken out and transported to an off-line spectroscopy lab for measurements. The implantation profile of the ions into the sample depends on the energy and the mass of the ion. The Gaussian distribution of the carbon molecules into the different samples has been simulated with the TRIM program¹ (Fig. 5.1 – 5.2). When the ¹¹C-molecules reach the surface, the molecule breaks up and the energy with which the carbon isotope will penetrate into the sample is calculated according to total ion energy × mass ratio and will therefore be 24.4 keV for the collections at 60 keV and 106 keV for the collections performed at 260 keV. The implantation takes place right under the surface of the samples, and therefore it is mostly the surface reactions that are important in this case. The different implantation energies give information about the diffusion in the target since the surface desorption do not change .

5.1 Measurements

After the implantation the activity in the samples was measured before it was demounted and transported to the off-line spectroscopy laboratory. Since ¹¹C is a beta emitter the activity in the sample was measured with γ -spectroscopy on the 511 keV line. The sample was thereafter heated and remeasured. The fractional activity (Eq. 5.1) was measured before and after diffusion annealing. While repeating this step we could retrieve information about the release at different temperatures.

$$F(t) = A_i(t)/A_0(t) \quad (5.1)$$

The samples were heated in steps until most of the activity had diffused or decayed out of the samples. The samples was heated within a Balzer chamber allowing to heat the samples under a pressure of 10⁻⁶ mbar, to ensure a homogeneous temperature of the pills during heating they were positioned inside a closed Re boat. The temperature calibration was performed with an optical pyrometer (± 10 °C). These heating conditions are similar to the conditions when the target is on line. The time between the measurements was no longer than one hour including pumping, 10 min heating and cooling down of the sample. The decay loss during this time was accounted for. The fractional activity give information of the diffusion properties in the materials.

¹<http://www.srim.org>

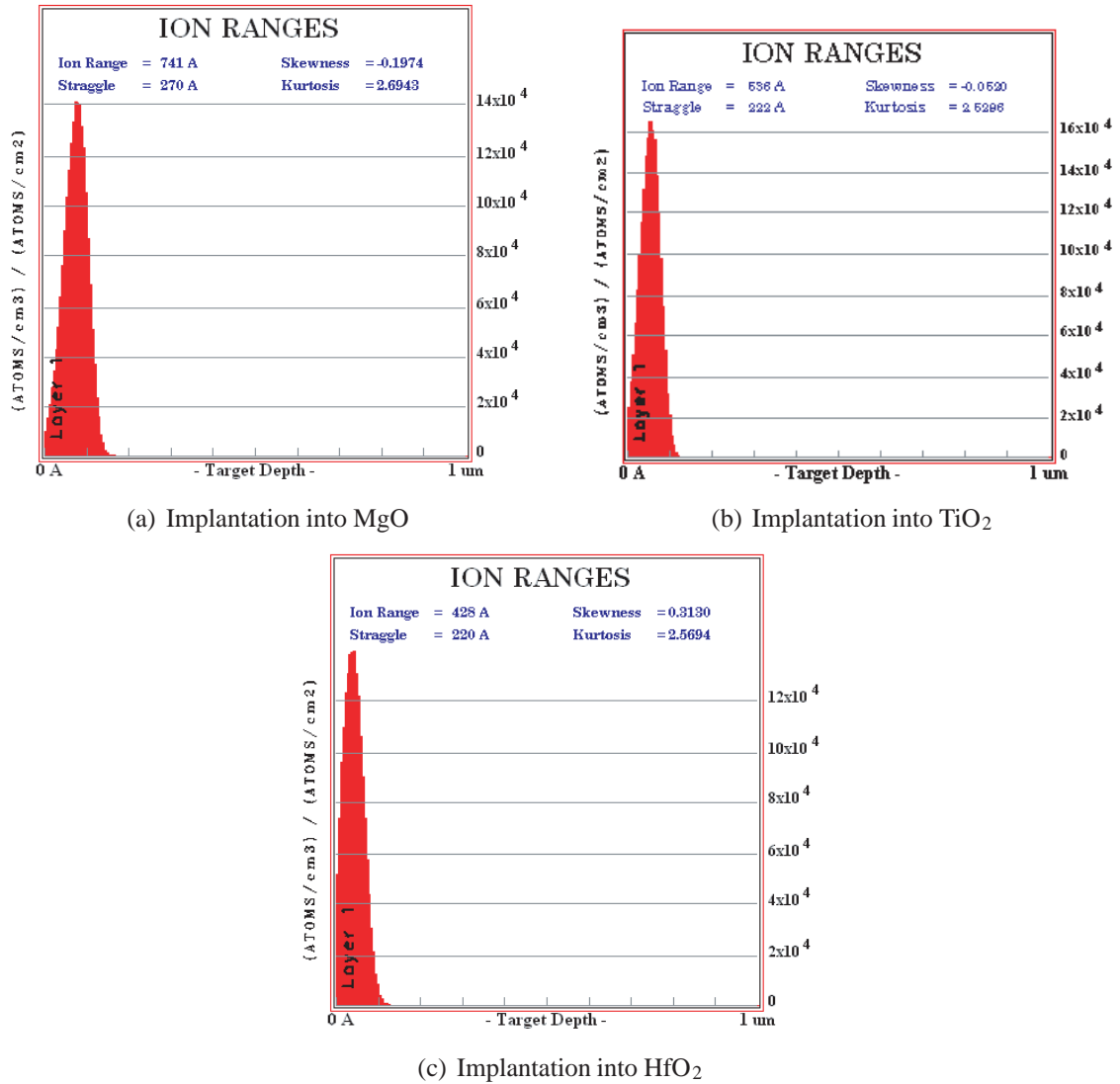


Figure 5.1: The implantation depths and the ion distribution in the samples at 60 keV. The ion ranges is the implantation depths, the negative skewness is a measure on the tail on the entrance side. The kurtosis around three on all samples is a sign on a relatively gaussian shaped peak.

The diffusion of the element in a material is described by the two equations of Fick. The diffusion was measured and then simulated with the RIBO code [83]. The code is calculating the diffusion starting with Fick's law:

$$J_n = -D(C, T) \cdot \left(\frac{\partial X}{\partial \hat{n}} \right) \quad (5.2)$$

Where J_n is the flux of atoms in \hat{n} direction, C is concentration of atoms in the sample [$1/\text{cm}^3$] and D is the diffusion coefficient [cm^2/s]. The diffusion D is strongly dependent on the temperature as coming from the Arrhenius equation (1.1). Diffusion in solids can be calculated

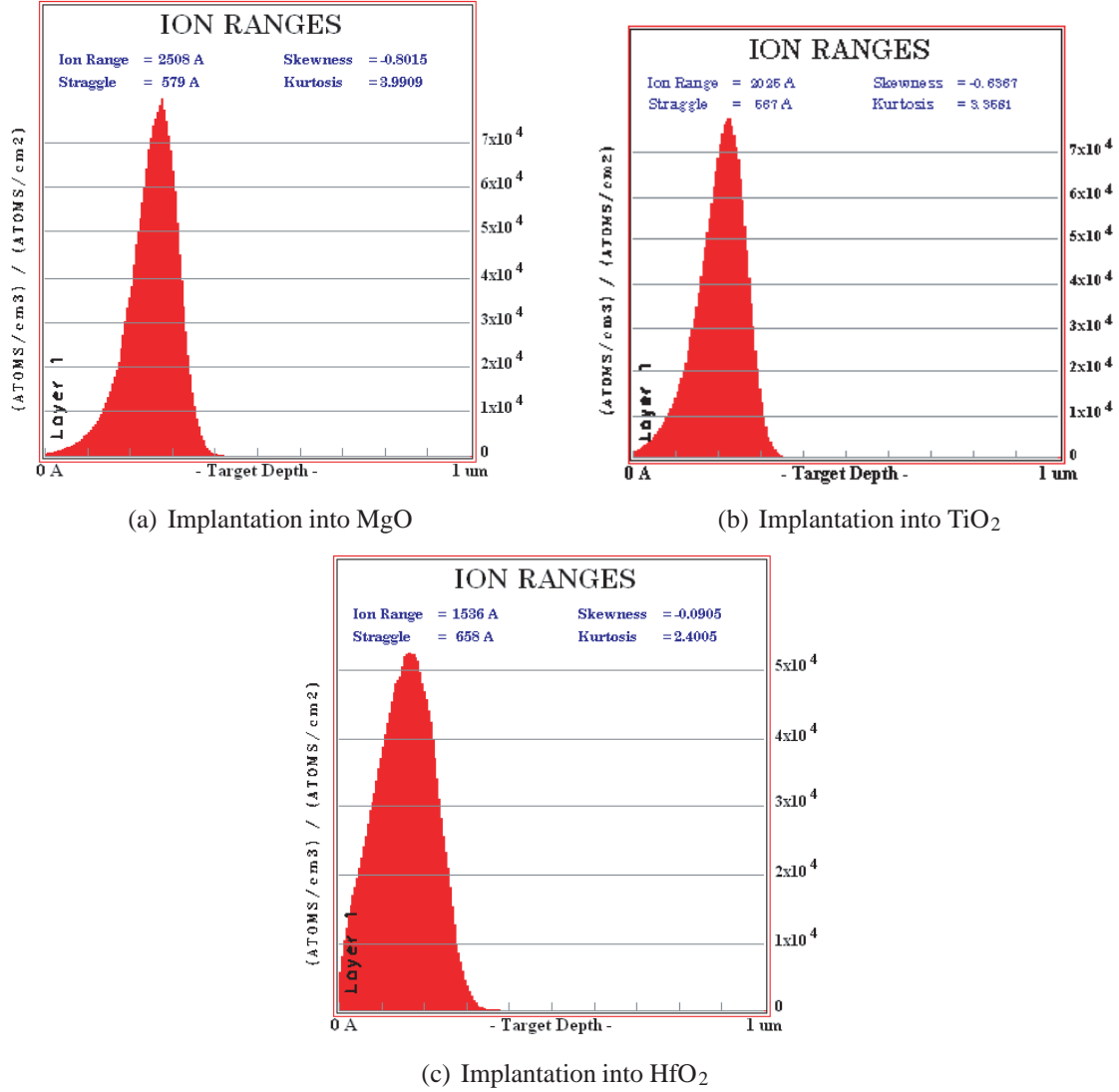


Figure 5.2: The implantation depths and the ion distribution in the samples at 260 keV. The ion ranges is the implantation depths, the negative skewness is a measure on the tail on the entrance side. The kurtosis around three on all samples is a sign on a relatively gaussian shaped peak.

with Fick's second law:

$$D \cdot \left(\frac{\partial C(\vec{r}, t)}{\partial \hat{n}} \right) = k \cdot C_s \quad (5.3)$$

$$\frac{\partial C(\vec{r}, t)}{\partial t} = D \Delta^2 C(\vec{r}, t) \quad (5.4)$$

$$F(t_c) = \frac{2n}{\pi^2} \sum_m c_m^{-1} e^{-c_m t_c} \quad (5.5)$$

5.1.1 Results

In Fig. 5.3(a)–5.3(c) the results of the implantation in MgO, TiO₂ and HfO₂ pressed powder pills are represented, the open markers are the results for implantations at 60 keV and the filled for implantations performed at 260 keV. The results show a clear difference in the released fraction vs. implantation depths. This means that the deeper in the samples that the carbon is created the longer will it take for it to diffuse out and be released. There are no resulting graphs for the fibre samples, the reason is the very fast release of the CO making the method too slow for this kind of experiment. Even at the lowest temperature accessible with our setup the remaining activity in the felt samples was negligible. For MgO and TiO₂ temperature up to 1200°C is enough for the release of 90% of the initial activity in the sample. For HfO₂ temperatures around 1600-2000°C are necessary for a similar efficiency. These results also give an idea of the required operational temperature of the target. Although from the results obtained for the fast release in the GANIL experiments with fibre felt targets and the thermo–chromatography experiments the use of pressed powder targets are no longer of a great interest. For the neutron deficient carbon isotopes a Al₂O₃ fibre felt target could be used instead of the standard powder CaO or MgO targets.

Table 5.2: Temperature needed for 10 % of the fractional activity in the samples to remain.

Material	Energy [keV]	Temp. [°C]
MgO	60	1150
MgO	260	1300
TiO ²	60	900
TiO ²	260	1150
HfO ²	60	1300
HfO ²	260	1500

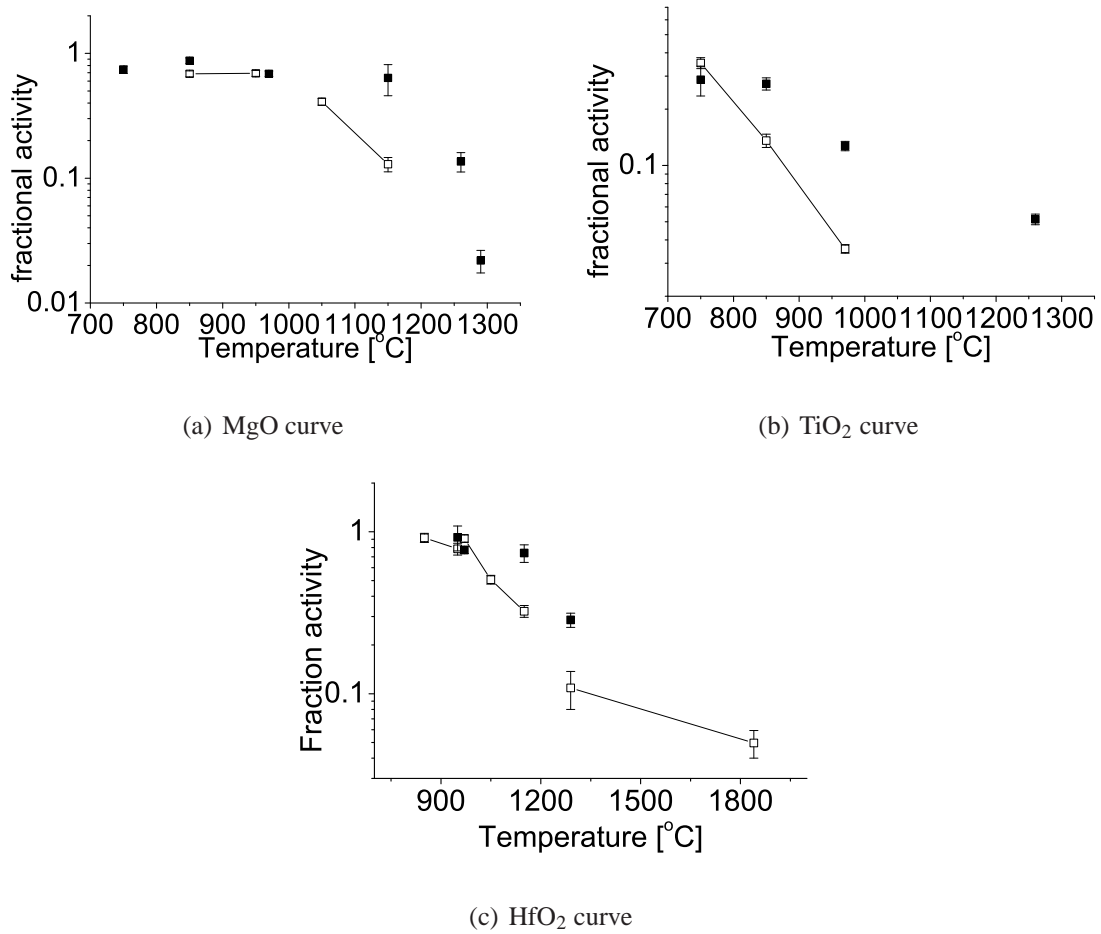


Figure 5.3: Release from the different metal oxides; A) MgO, B) TiO₂, C) HfO₂. The open markers are the results for implantations at 60 keV and the filled for implantations performed at 260 keV.

6

Ion sources

Working with ions is essential to do beam purifications with magnets, radio frequency coolers (RFQ), trapping and post-acceleration of the beam. At ISOLDE three ion-sources are routinely used in the TIS unit: a surface ion source, a Resonance Ionization Laser Ion Source (RILIS) and a Forced Electron Beam Induced Arc Discharge (FEBIAD) plasma ion source [76]. Understanding the processes in the ion source unit is of utmost importance for the optimization of the beam intensity, purity and emittance. Below is a short description of the existing ion sources and their individual advantages. As noted before CO_x , N_2 and NO_x with relatively low chemical reactivity and high volatility allow minimizing the temperature of the transfer line which gives an improvement of the beam purity by retention of the possible contaminating radioactive nuclei. As discussed in chapter 2 the reactivity of these molecules with heated metal surfaces restricts the choice of ion source. The ionization potentials (IP) for carbon and nitrogen in elementary- respectively molecular form are listed in Table 6.1, the values are taken from the works by Brescansin et al. and Moddemann et al. [84, 85].

Table 6.1: Ionization potential for carbon and nitrogen.

Element / Molecule	Ionization potential [eV]
C	11.26
CO	14.01
CO ₂	13.8
N	14.53
N ₂	15.6

6.1.2 Laser Ion Source

A chemically selective Resonance Ionization Laser Ion Source (RILIS) [86, 71, 87] is in use at ISOLDE. The method is efficient for elements with intermediate potentials ($\approx 6\text{--}10$ eV), that cannot be efficiently surface ionized and that would occur with a rather large isobaric background in a plasma ion source. The chemical selectivity makes RILIS the purest ion source at ISOLDE. Today 26 elements are available from RILIS [88, 89, 90] at ISOLDE, and more excitation schemes are being developed.

6.1.3 Plasma ion source

The commonly used, plasma ion source used at ISOLDE is a modified version of a FEBIAD ion source described in the references [91] and [73]. There are many types of plasma and/or electron discharge sources, an overview can be found in reference [92]. Common characteristics for the FEBIAD ion sources are their stable operation over long times in pressure regions of $3 \cdot 10^{-5}$ mbar to $5 \cdot 10^{-4}$ mbar. An electrode grid (typically graphite) is used as anode for the continuous extraction of fast electrons from a heated cathode surface. The plasma chamber is surrounded by magnet coils for better confinement of the plasma. Due to their high ionization potentials neither surface nor laser ion source allow an efficient ionization of C and N compounds. Another type of plasma ion source is the Electron Cyclotron Resonance Ion Source (ECRIS) that will be described in detail below. The ECR ion source would be complementing the FEBIAD plasma ion source and would provide a broader spectrum of possible elements for ionization. For elements like C, N, O, F the ionization efficiency has been $< 0.1\%$ with the FEBIAD ion source at ISOLDE. As mentioned previously the hot surface of the cathode is devastating for some of the elements. The molecular beams like N_2 , NO_x , CO_x , etc, would benefit from an ion source without any hot surfaces as the MiniMono ECR, or any other plasma ion source, using an RF-field to generate the plasma.

6.2 Electron Cyclotron Resonance Ion Source

The Electron Cyclotron Resonance ion source is a plasma ion source but with the advantage of not having hot surfaces inside the plasma chamber (therefore sometimes referred to as a "cold ion source"). The plasma in the ion source is created by the excited electrons from a buffer-gas injected into the source. A RF wave is exciting the electrons in the gas and creating a plasma. The magnets around the plasma chamber are having a minimum B field in the middle creating a well for the electrons that will gyrate around the magnetic field lines and stay confined in the ion source where the electron cyclotron resonance condition is fulfilled.

$$\omega_{\text{RF}} = \omega_c = \frac{qB}{m} \quad (6.1)$$

The radioactive atoms are then ionized in the plasma by collisions with the excited electrons and will then be extracted from the source. There exist several different types of ECR ion sources for different applications. Multi-charge ion sources can be used for the secondary acceleration of ion beams, while the 1^+ ion source is used for beam handling in experimental

areas. ECR ion sources are outstanding when it comes to ionization of noble gases and significant development work has been done. At GANIL a careful optimization of the design for the 1^+ ECR source, aiming for high efficiency and fast ionization, has been performed by P. Jardin et al. [93] and one of their achievements is the Mono1000 [82] that was used in the experiment described in the Chapter 4.4. A smaller version of a 1^+ ECR source has been adapted to an ISOLDE target, the MiniMono ECR ion source described by Gaubert et al. [94] (that is used in this work) which is a 2.45 GHz ion source. The adaptation to an ISOLDE on-line target system (see Fig. 6.2) has been described by Wenander et al. [95].

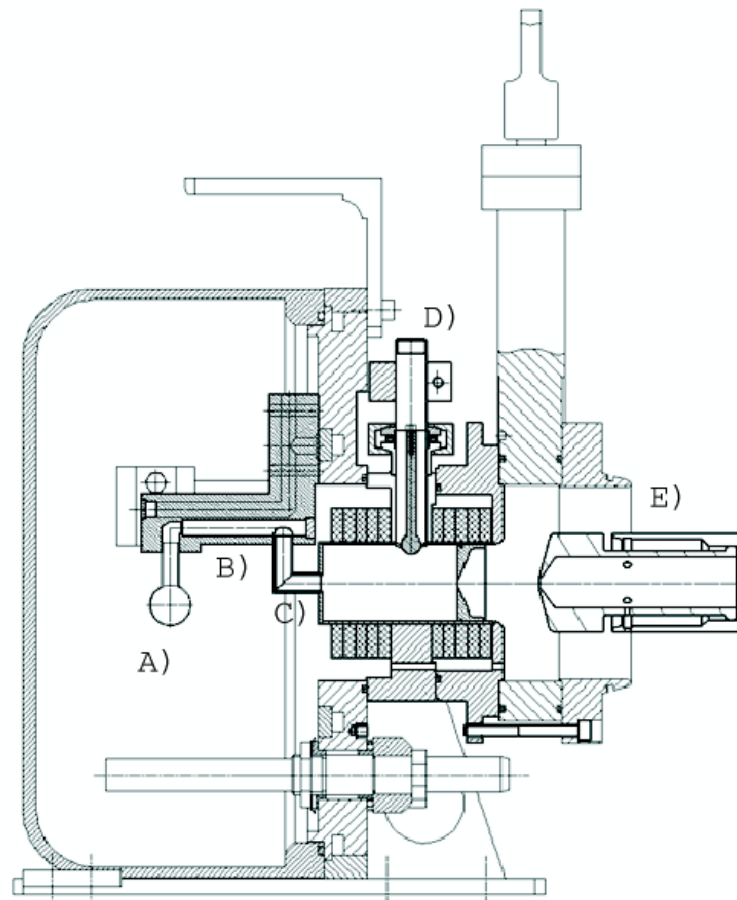


Figure 6.2: MiniMono target and ion source setup. A) ISOLDE target, B) Transfer-line, C) Plasma chamber with the two permanent magnets around, D) Antenna providing the Radio Frequency wave, E) Extraction electrode.

6.3 Off-line experiments with the MiniMono ECR 1⁺ ion source.

The MiniMono ECR (1⁺) is constructed with mirror symmetry of two permanent magnet around the plasma chamber, C) in Fig. 6.2. The antenna (D) is positioned in between the magnets for the coupling of a microwave frequency of 2.45 GHz for ionization of the buffer gas. The only adjustable parameters in this source are the power of the RF wave and the flow of the buffer gas into the ion source. The ISOLDE off-line separator was used for the development tests. The off-line separator consists of a front-end identical to the one at the on-line target stations. The ions are extracted at an energy of 30 keV. Four deflectors are installed for the beam steering, two horizontal and two vertical, a steering einzel lens and a 60° bending magnet. There are two Faraday cups for the read-out of the current in the line before and after the separator magnet. The transmission efficiency (ϵ_t) is achieved by comparison between the total current coming out directly from the source with the summed up current from the measured peaks after the separator magnet. In some experiments a slit was inserted after the magnet for improved resolution (see below). Two MiniMono ECR ion sources have been constructed for ISOLDE, the first with a CaO powder target has been tested on-line at the ISOLDE GPS target station (see Fig. 1.1) [95] for production of noble gases. The second ion source is built without target for off-line tests of ionization efficiencies for noble gases and other elements. Both sources are constructed with a calibrated gas leak in the transfer-line. The ionization efficiencies for He, N₂ and CO₂ were measured for different buffer gases. An overview of the buffer gases is presented in Table 6.2. Due to a possible large natural back-

Table 6.2: The buffer gases used during the test with the MiniMono ion source

Buffer gases:	Purity %	Company
Ar	(99.996 %)	Carbagas
Air		Open line
Ne	99.999 %	
Ar/Xe	95%/5%	
Xe	99	
N ₂	99.8	CarbaGaz

ground of the above mentioned molecules, gases enriched with the un-common isotopes ¹³C and ¹⁵N respectively were used for the tests. Their characteristics are presented in Table 6.3.

6.3.1 Experiment

During the tests a pressure $< 5 \cdot 10^{-6}$ mbar in the target and separator section next to the ion source was maintained. A continuous inlet of buffer gas to the source ensured stable conditions for the plasma. To test the ionization efficiencies an isotopically enriched gas was

6.3. OFF-LINE EXPERIMENTS WITH THE MINIMONO ECR 1⁺ ION SOURCE⁷⁵

Table 6.3: The isotopically enriched gases and their contaminations.

Gas	Isotopic contents	Contaminations
¹⁵ N ₂	¹⁴ N:1.8% ¹⁵ N:98.2%	N ₂ O:34ppm Ar/O ₂ :1650ppm CO ₂ :15ppm THC < 30ppm
¹³ C ¹⁸ O ₂	¹² C:0.97% ¹⁶ O:1.65% ¹³ C:99.03% ¹⁷ O:0.67% ¹⁸ O:97.68%	N ₂ O:15ppm O ₂ :184ppm

added through a calibrated leak. The RF power needed to ignite the plasma is dependent on the buffer gas, although the source was generally easily ignited at RF powers between 150-300 mV of a typical buffer gas pressure of $1 \cdot 10^{-6}$ mbar l/s. A total ion current varying from 80 to 160 μ A was obtained depending on the working conditions of the ion source (e.g. a large flow of buffer gas gave higher current). The extraction of the beam was optimized with a distance of 43 mm between the extraction electrode and the source for stable operation ².

6.3.1.1 Source behavior

A stable operation condition of the plasma was obtained one hour after ignition of the plasma. As expected, higher ionization efficiencies were achieved with lower concentrations of the buffer gas in the source. The efficiency of the source was optimal just at the limit of buffer gas starvation ³ in the plasma. With low RF powers (30 W) the best ionization of the molecules CO₂ and the N₂ was obtained. At higher RF powers, close to 60 W, the efficiency of the ionized molecules went down due to molecular break-up inside the plasma. For He, with IP=24.5 eV, a higher RF power (70 W) improved the ionization efficiency. RF power > 70 W resulted in a magnetic metal powder deposited inside the source. The magnetic powder most probably comes from a too intense plasma colliding with the walls of the plasma chamber.

6.3.2 Results

The tests with the different buffer gases showed that the source was easier ignited with argon and xenon than with N₂ or neon as buffer gases. Argon and xenon have ionization potentials of 15.8 and 12.1 eV respectively while neon has 21.5 eV. Therefore argon and xenon have larger ionization cross sections and are more likely to be stripped by electrons. For argon we

²If the extraction electrode comes too close to the source, sparking will be a problem for a stable run, but if the extractor is too far away the beam will be lost if diverging before the deflectors.

³as low flow as possible without turning off the plasma

noted up to 4^+ and for xenon up to 5^+ charged ions⁴, with efficiencies as:

$$\frac{\epsilon_{Ar1+}}{\epsilon_{Ar2+}} = 5 \quad (6.2)$$

$$\frac{\epsilon_{Ar1+}}{\epsilon_{Ar3+}} = 150 - 200 \quad (6.3)$$

$$\frac{\epsilon_{Ar1+}}{\epsilon_{Ar4+}} = 5000 - 10000 \quad (6.4)$$

The intensity of the observed Ar^+ peak at $A/q=40$ forced us to use a slit in front of the Faraday cup to be able to separate the peaks and measure $^{13}C^{18}O_2^+$ with $A/q = 49$. The mixture of Ar/Xe gas and the pure xenon gas gave too large background in the mass spectrum at the multi-charge states of xenon to be used for measurements. N_2 gave a clean background but with a strong peak at $A/q=28$ it was not possible to measure the molecules formed as $^{14}N^{15}N^+$ and $^{13}C^{16}O^+$ at $A/q=29$. The most suitable buffer gas was therefore found to be Ar, since it give a low background for A/q between 20 and 40. The results are shown in Table 6.4 and are calculated after the equation:

$$\epsilon_{ion} = \frac{I_{ion}}{\epsilon_t \cdot \frac{A_{leak} \cdot P}{k_B \cdot T} \cdot q \cdot \sqrt{\frac{28}{A_{ion}}}} \quad (6.5)$$

Table 6.4: Retrieved ionization efficiencies using argon as buffer gas in the MiniMono ion source.

Leak	Ion	Mass	I_{tot} μA	rf power mV	P_s	P_t	ϵ_t %	ϵ_i %
He	$^4He^{2+}$	2	170	730	$2 \cdot 10^{-6}$	$1.8 \cdot 10^{-6}$	80	5.4
He	$^4He^+$	4	170	730	$2 \cdot 10^{-6}$	$1.8 \cdot 10^{-6}$	80	3
CO	$^{13}C^{16}O^+$	29	80	300	$1.8 \cdot 10^{-6}$	$1.4 \cdot 10^{-6}$	25.5	14.4
CO ₂	$^{13}C^{18}O^+$	31	80	300	$1.8 \cdot 10^{-6}$	$1.4 \cdot 10^{-6}$	25.5	not seen
CO ₂	$^{13}C^{18}O_2^+$	49	110	300	$1.9 \cdot 10^{-6}$	$1.9 \cdot 10^{-6}$	23	3.7
N ₂	$^{14}N^{15}N^+$	29	100	300	$6.1 \cdot 10^{-7}$	$1.1 \cdot 10^{-6}$	26.5	11.5
N ₂	$^{15}N^{15}N^+$	30	100	300	$6.1 \cdot 10^{-7}$	$1.1 \cdot 10^{-6}$	26.5	5.1

6.4 Discussion

From the results seen in Table 6.4 we can draw several conclusions. The first conclusion is that the molecules break up within the plasma chamber when the RF power goes up. The CO₂ molecules seem too break up into O₂ and C whereof C rebinds with O in the target forming

⁴Ar¹⁺, Ar²⁺, Ar³⁺ and Ar⁴⁺ with A/q of 40, 20, 13.3 and 10 respectively was used for the A/q calibration of the mass spectra

$^{13}\text{C}^{16}\text{O}$ rather than $^{13}\text{C}^{18}\text{O}$ since it is not seen in even low currents (<1 nA). Further on the N_2 molecule injected in form of $^{15}\text{N}^{15}\text{N}$ seems to break up easily to and form $^{14}\text{N}^{15}\text{N}$ which is seen more than the enriched. These results probably depend strongly on a small leak of air somewhere in the ion source providing ^{16}O and ^{14}N . So far we only discussed the application for ISOL ion sources (1^+ or n^+) which are directly connected to the target, but there are also possible applications to $1^+ \rightarrow n^+$ ECRIS charge breeders [96]. Given the low efficiency for direct capture of CO^+ beams in the plasma of an $1^+ \rightarrow n^+$ charge breeder ECRIS [97] a quartz or a sapphire line inserted into the plasma chamber might help to enhance the recycling efficiency of CO and, hence, lead to a higher overall efficiency for the dissociation and charge breeding of CO_x or N_2 beams. [98, 65].

7

Summary and Outlook

The ideal construction of a target and ion source unit for the production of intensive ion beams of short lived carbon isotopes at an ISOL facility has been investigated. Carbon is reacting strongly with metals at high temperature. So far the yields obtained are up to five or six orders of magnitude lower than predicted. The low efficiency for the carbon production has been shown to be life-time dependent. There are three main areas that have been investigated:

- production: different target materials and their structures were tested
- transport: adsorption enthalpies onto target material, target container and transfer line were retrieved.
- ionization: the ionization efficiencies in an ECR ion source were measured.

The diffusion in a material and ionization in a source are two processes which are element dependent. They should not give a significant half-life dependent signal. Since the half life of ^{11}C is relatively long ($T_{1/2}=20.4$ min), the decay losses during transport can be neglected. Using materials for the transfer line and target holder that were shown to be inert for surface reactions, should therefore give same release efficiencies for the shorter lived isotopes. Considering gaining additionally two orders of magnitude on the ionization efficiency using an ECRIS rather than a FEBIAD the overall efficiencies would come up to four orders of magnitude higher for the short lived isotopes.

This can be accomplished by forming molecules of the reactive elements, minimizing the surface retention during transport of the products out of the target and in to the ion source. Target materials as MgO and HfO_2 with fibre felt structures are chosen for their short diffusion time and low surface adsorption enthalpies. For the ionization of carbon off-line ionization efficiencies were measured with a MiniMono ECR ion source constructed to fit onto an ISOLDE TIS unit. These measurements showed high liability of the ion source. The ion source should preferably be used with a buffer gas of argon not to produce ions on similar mass-to-charge

ratios as the CO and CO₂ ions. The ionization efficiencies using an ECR ion source are between 30 and 100 times higher than the use of a classical FEBIAD ion source. However the total throughput of the ion source (ie the sum of the ion currents for all isotopes and charge states) is still a challenge at ISOLDE. If the Mini Mono ECRIS is to be used in the future at ISOLDE a heat shield should be used between the target and the ion source to preserve the magnet.

Several experiments have been performed at ISOLDE for the production of carbon, using a CaO target coupled to a FEBIAD plasma ion source through a metal transfer line that was kept cold. The measured yield in these repeated experiments are lower than the one when a MgO target was used. The measured yield of $5.3 \cdot 10^5$ for production of ¹⁰C with a CaO target stated in the ISOLDE yield data base has never been repeated. Although the production cross section is higher for a CaO target than a MgO target, the higher adsorption enthalpy for the CaO than for the MgO retrieved in this work can explain the losses. The approach reported here can be used for other elements, that are from a chemical point of view difficult to produce, such as fluorine or boron isotopes.

At GANIL where the current interest is more focussed on the production of intense Kr beams the use of a full size oxide fiber target at SPIRAL would allow to boost the beam intensities observed at SIRa by about two orders of magnitude: above a factor ten for higher effective target thickness when going to 95 MeV/u instead of 25 MeV/u and a factor around ten for higher primary beam intensity. The target fragmentation of a ZrO₂ fiber target bombarded with ¹²C would moreover provide higher intensities for neutron-deficient Kr beams than available today from ⁷⁸Kr projectile fragmentation.

8

Abbreviations

Table 8.1: Explanation of abbreviations and symbols used in the chapter.

Symbol	Definition	
ISOL	Isotope Separation On Line	
RIB	Radioactive Ion Beam	
IF	In-Flight	
CERN	European Organization for Nuclear Research	
HRS	High Resolution Separator	
GPS	General Purpose Separator	
TIS	Target and Ion Source unit	
Z	proton number in nucleus	
D	Diffusion coefficient	m^2/s
D_0	Maximum diffusion coefficient	m^2/s
E_a	Activation energy	kJ/mol
R	Gas constant	$\text{J}/(\text{K mol})$
T	Temperature	K
t_r	residence time	sec.
ϵ_{targ}	overall target efficiency	%
ϵ_t	transmission efficiency	%
ϵ_d	detector efficiency	%
Y	ion yield	$\text{ions}/\mu\text{C}$
P	Production	$\text{atoms}/\mu\text{C}$
t	time	s
τ_r	rise time	ms
τ_f	fast decay time	s

Continued on Next Page...

Table 8.1 – Continued

Symbol	Definition	
τ_s	slow decay time	s
α	weighting parameter	
λ		
$\rho(t)$		
δ_{Mg}	Density of Mg. in target	g/cm ²
M_{Mg}	Atomic weight	g/mol
N_A	Avogadro's constant	mol ⁻¹
σ_x	Cross section	mb
N_i	Number of ions	
P	production per proton puls	
GANIL	Grand Accelérateur National des Ion Lourds	
SIRa	Séparation d'Ion Radioactive	
SISSI	Source d'Ions Secondaire à Supraconducteur Intense	
ECR	Electron Cyclotron Resonance	
SRIM	Stopping Range of Ions in Matter	
DC	Direct Current	
RaBIT	Rapid p-Beam Irradiation Transport	
T_R	release time	
FEBIAD	Forced Electron Beam Induced Arc Discharge	
RILIS	Resonance Ionization Laser Ion Source	
ECRIS	Electron Cyclotron Resonant Ion source	
CVL	Copper Vapor Laser	
RFQ	Radio Frequency Cooler	
IP	Ionization potential	eV
Φ	Work function, energy required to remove one electron	
RF	Radio Frequency	
I_{fc}	Intensity in Faraday cup	nA
I_{tot}	total current from the source	μ A
P_s	Pressure in the separator part	mbar
P_t	Pressure in the extraction area after the TIS unit	mbar
ε_i	Ionization efficiency	%
ΔH_{ads}	Adsorption enthalpy	J/mol
ΔS	Adsorption Entropy	J/(mol K)
R	Ideal gas constant	
T_0	Standard temperature	K
T_{dep}	Deposition temperature	K
T_{max}	Maximum temperature	K
T_{start}	Starting temperature	K
g	Temperature gradient	K/m

Continued on Next Page...

Table 8.1 – Continued

Symbol	Definition	
u_0	Initial velocity of gas	cm^3/min
t_e	Experimental time	min
A/V	Standard volume to surface area	cm^{-1}
a	Surface area of investigated material	cm^2
v	Volume of the open column	cm^3
ν_B	Vibrational frequency	s^{-1}
k_B	Boltzmann constant	J/K
m	Molar mass of adsorbed molecule	kg/mol
τ_r	Retention time	s

9

Appendix

9.1 Appendix Target production

9.1.1 Preparation of pressed powder pills

The pressed powder pills have a size of 14 mm in diameter and are 1–3 mm thick. The tablets are prepared by pressing a few milligrams of the specific metal oxide powder. The powder is inserted into a holder and pressed with 50-100 bars with in a hydraulic press to form dense pills, solid enough for the experiments. The pills was then heated for sintering in a Balzer chamber. The Balzer chamber allowed to heat the samples to temperatures above 2000 °C remaining a pressure of ($p < 5 \times 10^{-5}$ mbar). The diffusion out of the pills then will be dependent on the density of the final pills. For the experiments described herein the pills and the fiber samples were outgassed under vacuum for 30 min at temperatures around 1000 °C.

9.1.2 Cross-section tables

Table 9.1: Calculated cross-sections for the MgO target used in the on-line experiments performed at ISOLDE, see chapter 4. The calculations are performed with the EPAX and the Silberberg and Tsao method.

Molecule	S & T		In-target production rate per μC	EPAX		total per μC
	O mb	Mg mb		O mb	Mg mb	
^9CO	$1.0 \cdot 10^{-1}$	$1.8 \cdot 10^{-1}$	$1.2 \cdot 10^8$	$7.4 \cdot 10^{-2}$	$5.0 \cdot 10^{-2}$	$5.2 \cdot 10^7$
^{10}CO	$5.2 \cdot 10^{-1}$	$8.7 \cdot 10^{-1}$	$5.8 \cdot 10^8$	$9.2 \cdot 10^{-1}$	$6.0 \cdot 10^{-1}$	$6.3 \cdot 10^8$
^{11}CO	1.1	5.5	$6.7 \cdot 10^9$	5.3	4.0	$3.9 \cdot 10^9$

Continued on Next Page. . .

Table 9.1 – Continued

^{15}CO	$1.2 \cdot 10^{-2}$	$6.6 \cdot 10^{-1}$	$2.8 \cdot 10^8$	$4.6 \cdot 10^{-3}$	$5.0 \cdot 10^{-1}$	$2.1 \cdot 10^8$
^{16}CO	$1.5 \cdot 10^{-3}$	$6.7 \cdot 10^{-2}$	$2.9 \cdot 10^7$	$1.2 \cdot 10^{-3}$	$6.0 \cdot 10^{-2}$	$2.6 \cdot 10^7$
^{17}CO		$3.6 \cdot 10^{-3}$	$1.5 \cdot 10^6$	$5.0 \cdot 10^{-3}$		$2.1 \cdot 10^6$
^{18}CO		$1.0 \cdot 10^{-4}$	$4.2 \cdot 10^4$	$4.0 \cdot 10^{-4}$		$1.7 \cdot 10^5$
^{18}Ne		1.8	$7.5 \cdot 10^8$		$7.2 \cdot 10^{-1}$	$3.0 \cdot 10^8$
^{12}NN	$6.5 \cdot 10^{-1}$	1.1	$7.3 \cdot 10^8$	$9.9 \cdot 10^{-1}$	$7.0 \cdot 10^{-1}$	$7.0 \cdot 10^8$
^{13}NN	3.6	1.9	$2.3 \cdot 10^9$	5.9	4.1	$4.2 \cdot 10^9$
^{16}NN	$3.4 \cdot 10^{-2}$	2.9	$1.2 \cdot 10^9$		3.0	$1.2 \cdot 10^9$
^{17}NN	$4.7 \cdot 10^{-2}$	$7.1 \cdot 10^{-1}$	$3.1 \cdot 10^8$		$5.9 \cdot 10^{-1}$	$2.5 \cdot 10^8$
^{18}NN		$7.0 \cdot 10^{-2}$	$2.9 \cdot 10^7$		$7.5 \cdot 10^{-2}$	$3.1 \cdot 10^7$
^{19}NN		$4.5 \cdot 10^{-4}$	$1.9 \cdot 10$		$6.3 \cdot 10^{-3}$	$2.6 \cdot 10^6$
^{20}NN		$1.2 \cdot 10^{-4}$	$4.9 \cdot 10^4$			

Table 9.2: Results from the yield and release measurements and calculations from the ISOLDE tape station. ϵ_t and β_{eff} is assumed to be 90 % in all cases.

File	$\frac{N}{\text{pulse}}$	α	τ_r ms	τ_f ms	τ_s ms	$T_{1/2}$ ms	YIELD $\frac{\text{atoms}}{\mu\text{C}}$	Rel.
^6He	$6.12 \cdot 10^5$	0.78	13.41	51.7	155.87	806.7	$2.62 \cdot 10^5$	0.88
^8He	$8.89 \cdot 10^3$	0.78	13.41	51.7	155.87	806.7	$2.62 \cdot 10^5$	0.88
^{10}CO	$1.57 \cdot 10^4$	0.98	25	16.65	893.93	19300	$1.00 \cdot 10^3$	0.52
^{10}CO	$4.43 \cdot 10^4$	0.93	25	56.96	7114.49	19300	$7.36 \cdot 10^3$	0.75
^{11}CO	$1.96 \cdot 10^6$	0.74	25	322.45	18302.55	1222800	$6.67 \cdot 10^5$	0.99
^{15}CO	$9.88 \cdot 10^3$	0.75	25	55.25	2958.62	2450	$1.01 \cdot 10^3$	0.47
^{16}NN	$6.59 \cdot 10^5$	0.82	1519.49	409.99	16152.57	7130	$3.92 \cdot 10^4$	0.27
^{18}Ne	$8.84 \cdot 10^5$	0.91	14.35	273.74	4026.8	1670	$9.96 \cdot 10^4$	0.51
^{18}Ne	$9.54 \cdot 10^4$	0.86	18.99	201.33	1048.71	1670	$4.43 \cdot 10^4$	0.75
^{19}Ne	$3.71 \cdot 10^6$	0.96	16.23	285.51	10171.27	17296	$1.77 \cdot 10^6$	0.77
^{23}Ne	$1.33 \cdot 10^6$	0.8	18.68	273.25	5826.37	37200	$2.55 \cdot 10^5$	0.88
^{24}Ne	$5.69 \cdot 10^5$	0.8	18.68	273.25	5826.37	202800		

9.1.3 Release figures

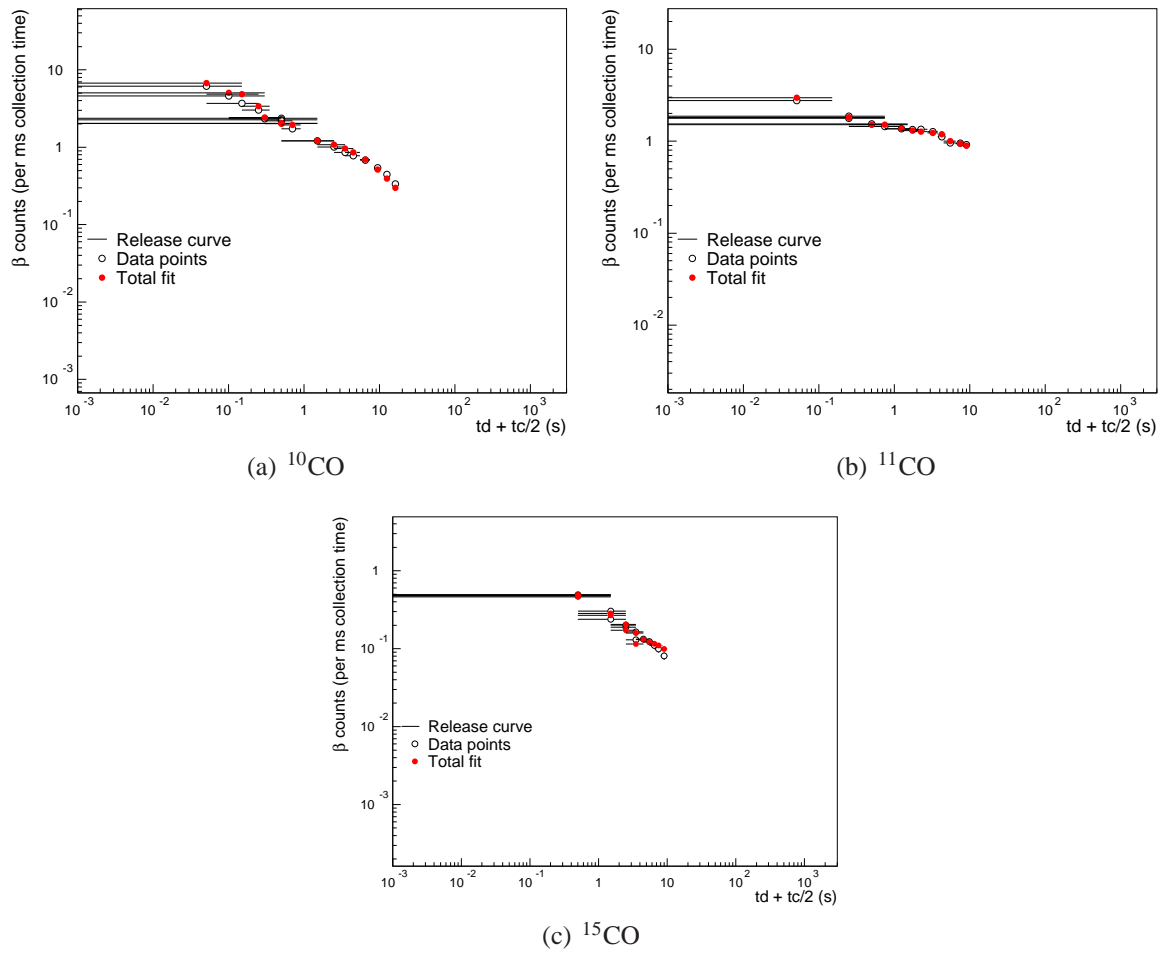


Figure 9.1: Release curves for CO molecules.

Table 9.3: Overview of the isotopes and molecules investigated during the experiments with the timing used

Isotopes	Mass	$T_{1/2}$ ms	Beam gate ms	Protons	Intensity	Comments
^{17}Ne	17	109.2	open	1 ppsc		
^6He	6	806.7	open	1 ppsc		
^6He	6	806.7	100/10	1 ppsc		
^8He	8	119	open	1 ppsc		
$^{15}\text{C}^{15}\text{O}$	30	2.45s, 2.03m	}open	1 ppsc		
$^{13}\text{N}^{17}\text{N}$		9.96m 4.17s				
$^{15}\text{C}^{15}\text{O}$	30	2.45 s, 2.03m	} 1/2000	1 ppsc		
$^{13}\text{N}^{17}\text{N}$		9.96m 4.17s				

Continued on Next Page...

Table 9.3 – Continued

$^{16}\text{N}^{14}\text{N}$	30	7130	1/2000	1 ppsc		
$^{16}\text{N}^{14}\text{N}$	30	7130	open	8/8 ppsc		
$^9\text{C}^{16}\text{O}$	25	126.5	1ms/200ms	8/8 ppsc		
$^9\text{C}^{16}\text{O}$	25	126.5	open	8/8 ppsc		
$^{18}\text{N}^{14}\text{N}$	32	630	open	8/8 ppsc		
$^{18}\text{N}^{14}\text{N}$	32	630	1ms/400ms	8/8 ppsc		
$^{12}\text{N}^{14}\text{N}$	26	11	1ms/50ms	8/8 ppsc		
$^9\text{C}^{16}\text{O}$	25	126.5	1ms/200ms	12/12 ppsc		
$^{18}\text{N}^{14}\text{N}$	32	630	open	12/12 ppsc		
$^{16}\text{N}^{14}\text{N}$	30	7130		12/12 ppsc	$3.3 \cdot 10^{13}$	
$^{16}\text{N}^{14}\text{N}$	30	7130		12/12 ppsc		
$^{12}\text{N}^{14}\text{N}$	26	11	1ms/50ms	12/12 ppsc		

Table 9.4: Decay mode of the carbon isotopes, energies are stated in intensity scale from strongest to lowest. Ref. [99] for ^{17}C

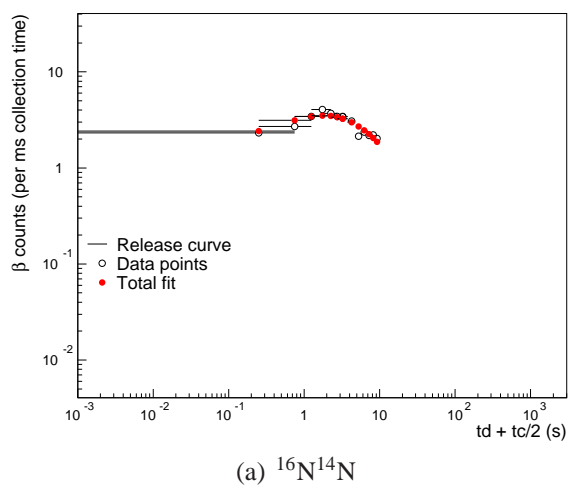
Isotope	$T_{1/2}$ s	β [MeV]	βt	Decay mode			
				$\beta\alpha$	βn [MeV]	$\beta 2n$	$\beta 3n$
^9C	0.1265(9)	16.4948(24)	8.24, 10.92				
^{10}C	19.290(12)	3.64795(12)	718, 1022				
^{11}C	1239(2)	1.9824(9)					
^{15}C	2.449(5)	9.771,7(8)	4.5, 9.8				
^{16}C	0.747(8)	8.010(4)			0.79, 1.72		
^{17}C	0.193(5)	13.167(23)	3.069(17)	2.052(17)	7.284(18)	4.795(17)	
^{18}C	0.092(2)	11.810(40)	0.11(3)	–	8.980(30)	3.103(30)	0.615(30)
^{19}C	0.0462(23)	16.56(10)	3.8(1)		11.23 (10)	8.4(1)	2.5(1)
^{20}C	.016(3)	15.79(25)	1.57(24)	–	13.62(24)	8.30(24)	5.48(24)
^{22}C	0.0062(13)	21.2(9)	5.9(9)	–	20.0(9)	15.4(9)	13.2(9)

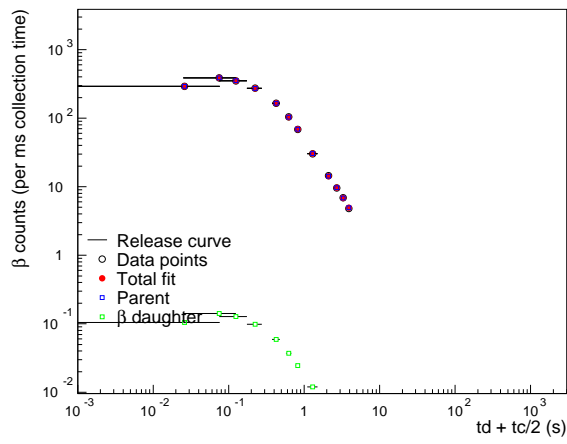
Table 9.5: Decay mode of the nitrogen isotopes, energies are stated in intensity scale from strongest to lowest.

Isotope	$T_{1/2}$ s	Decay mode				
		γ	β	βt	$\beta\alpha$	βn
^{12}N	0.011000(16)	4439	17.338(1)		0.2	
^{13}N	597.90(24)		2.2205(3)			
^{16}N	7.13(2)	6129, 7115	10.421(3)		1.76	

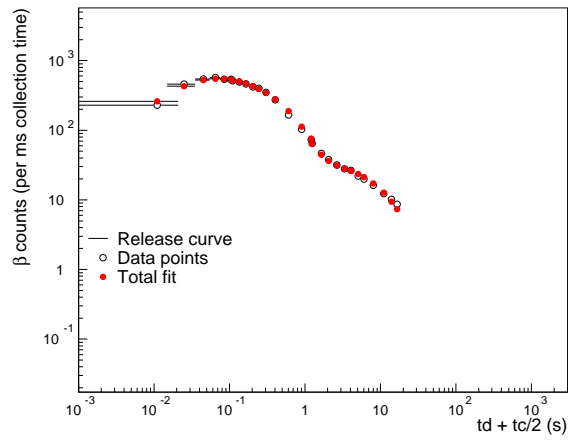
Continued on Next Page...

Isotope	$T_{1/2}$ s	Decay mode				
		γ	β	βt	$\beta\alpha$	βn
Table 9.5 – Continued						
^{17}N	4.173(4)	871, 2184	8.680(15)		1.25, 1.41	4.537(15)
^{18}N	0.622(9)	1982, 822	13.896(19)	1.08, 1.41		5.852(19)
^{19}N	0.271(8)	96, 3138, 709	12.827(17)	unknown		8.572(16)
^{20}N	0.130(7)		17.97(6)			10.36(6)
^{21}N	0.087(6)		17.19(10)			13.38(10)
^{22}N	0.0139(14)		22.75(20)	unknown		15.90(19)

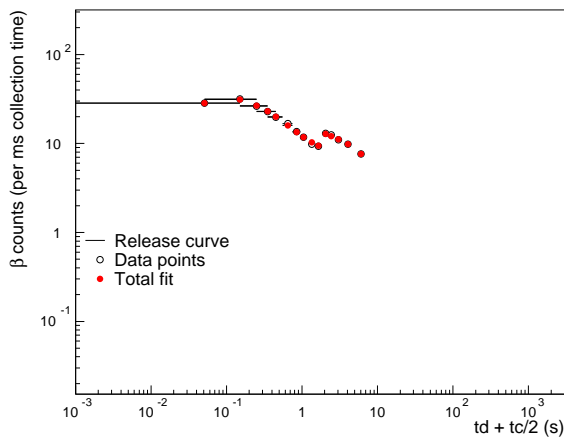
Figure 9.2: Release curve taken for N_2 molecule.



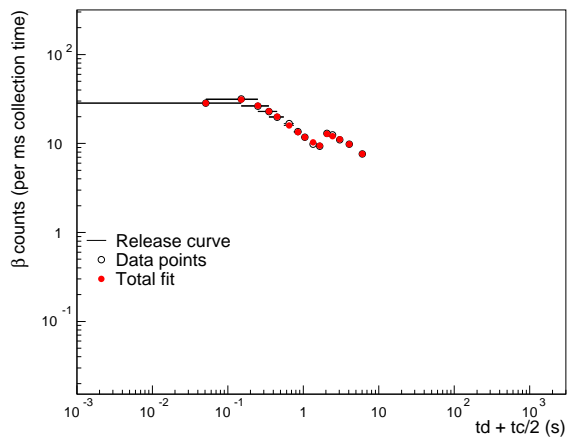
(a) ^{18}Ne



(b) ^{19}Ne

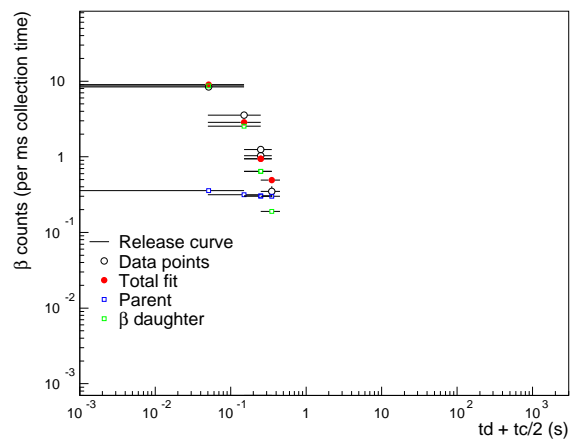


(c) ^{23}Ne



(d) ^{24}Ne

Figure 9.3: Release curves taken for Ne isotopes.



(a)

Figure 9.4: Release curve for ^8He

Bibliography

- [1] H. Becqueuel. Par les radiations emises par phosphorescence. *Comptes rendu hebdomaires*, T122:420, 1896.
- [2] B. Jonson. Present and future RNB facilities in Europe. *Nucl. Phys. A*, 701:35–42, 2002.
- [3] P. Van Duppen. Technological challenges of new radioactive beam facilities. *Nucl. Instr. Meth. B*, 204:9–16, 2003.
- [4] B. Jonson. Light dripline nuclei. *Phys. Rep.*, 389:1–59, 2004.
- [5] J. Liouville. Note sur la théorie de la variation des constantes arbitraires. *J. Math. pures et appl.*, 3:342, 1838.
- [6] U. Köster. ISOLDE target and ion source chemistry. *Radiochimica Acta*, 89:749–756, 2001.
- [7] U. Köster. How to Produce Intense and Pure ISOL Beams. *Prog. Part. Nucl. Phys.*, 46:411–412, 2001.
- [8] F. M. Marqués, E. Liegard, N. A. Orr, J. C. Angélique, L. Axelsson, G. Bizard, W. N. Catford, N. M. Clarke, G. Costa, M. Freer, S. Grévy, D. Guillemaud-Mueller, G. J. Gyapong, F. Hanappe, P. G. Hansen, B. Heusch, B. Jonson, C. Le Brun, F. R. Lecolley, F. Lefebvres, M. Lewitowicz, G. Martínez, A. C. Mueller, T. Nilsson, A. Ninane, G. Nyman, B. Petersen, F. Pougheon, K. Riisager, M. G. Saint-Laurent, Y. Schytz, M. Smedberg, O. Sorlin, L. Stuggé, and D. D. Warner. Neutrons from the breakup of ^{19}C . *Phys. Lett B*, 381:407–412, 1996.
- [9] T. Baumann, M. J. G. Borge, H. Geissel, H. Lenske, K. Markenroth, W. Schwab, M. H. Smedberg, T. Aumann, L. Axelsson, U. Bergmann, D. Cortina-Gil, L. Fraile, M. Hellström, M. Ivanov, N. Iwasa, R. Janik, B. Jonson, G. Münzenberg, F. Nickel, T. Nilsson, A. Ozawa, A. Richter, K. Riisager, C. Scheidenberger, G. Schreider, H. Simon, B. Sitar, P. Strmen, K. Sümmerer, T. Suzuki, M. Winkler, H. Wollnik, and M.V. Zhukov. Longitudinal momentum distributions of $^{16,18}\text{C}$ fragments after one-neutron removal from $^{17,19}\text{C}$. *Phys. Lett B*, 439:256–261, 1998.
- [10] V. Maddalena, T. Aumann, D. Bazin, B. A. Brown, J. A. Caggiano, B. Davis, T. Glasmacher, P. G. Hansen, R. W. Ibbotson, A. Navin, B. V. Pritychenko, H. Scheit, B. M. Sherrill, M. Steiner, J. A. Tostevin, and J. Yurkon. Single-neutron knockout reactions: Application to the spectroscopy of $^{16,17,19}\text{C}$. *Phys. Rev. C*, 63(024613), 2001.

- [11] A. Ozawa, O. Bochkarev, L. Chulkov, D. Cortina, H. Geissel, M. Hellström, M. Ivanov, R. Janik, K. Kimura, T. Kobayashi, A. A. Korshennikov, G. Münzenberg, F. Nickel, Y. Ogawa, A. A. Ogloblin, M. Pfützner, V. Pribora, H. Simon, B. Sitár, P. Strmen, K. Summerer, T. Suzuki, I. Tanihata, M. Winkler, and K. Yoshida. Measurements of interaction cross sections for light neutron-rich nuclei at relativistic energies and determination of effective matter radii. *Nucl. Phys. A*, 691:599–617, 2001.
- [12] R. Kanungo, I. Tanihata, Y. Ogawa, H. Toki, and A. Ozawa. Halo structure in ^{19}C . *Nucl. Phys. A*, 701:378c–382c, 2002.
- [13] K. Yoneda, N. Aoi, H. Iwasaki, H. Sakurai, H. Ogawa, T. Nakamura, W.-D. Schmidt-Ott, M. Schäfer, M. Notani, N. Fukuda, E. Ideguchi, T. Kishida, S. S. Yamamoto, and M. Ishihara. β -decay half-lives and β -delayed neutron multiplicities of the neutron drip-line nuclei ^{19}B , ^{22}C and ^{23}N . *Phys. Rev. C*, 67:014316, 2003.
- [14] M.J.G. Borge, Y. Prezado, U.C. Bergmann, R. Boutami, J. Cederkäll, C. Aa. Diget, L. M. Fraile, H. O. U. Fynbo, Y. Jading, H. Jeppesen, B. Jonson, I. Martel, M. Meister, T. Nilsson, G. Nyman, K. Riisager, H. Simon, O. Tengblad, L. Weissman, F. Wenander, and K. Wilhelmsen. Asymmetry in the super-allowed β -transition of the $A=9$ isobars. *Nucl. Phys. A*, 738:206–210, 2004.
- [15] M. Stanoiu, F. Azaiez, F. Becker, M. Belleguic, C. Borcea, C. Bourgeois, B. A. Brown, Z. Dlouký, Z. Dombrádi, Z. Fülöp, H. Grawe, S. Grévy, F. Ibrahim, A. Kerek, A. Krasznahorkay, M. Lewitowicz, S. Lukyanov, H. van der Marel, P. Mayet, J. Mrázek, S. Mandal, D. Guillemaud-Mueller, F. Negoita, Y. E. Penionzhkevich, Z. Podolyák, P. Roussel-Chomaz, M. G. Saint Laurent, H. Savajols, O. Sorlin, G. Sletten, D. Sohler, J. Timár, C. Timis, and A. Yamamoto. Study of drip line nuclei through two-step fragmentation. *Eur. Phys. J. A*, 20:95–96, 2004.
- [16] Z. Elekes, Zs. Dombrádi, R. Kanungo, H. Baba, Zs. Fülöp, J. Gibelin, Á. Horváth, E. Ideguchi, Y. Ichikawa, N. Iwasa, H. Iwasaki, S. Kanno, S. Kawai, Y. Kondo, T. Motobayashi, M. Notani, T. Ohnishi, A. Ozawa, H. Sakurai, S. Shimoura, E. Takeshita, S. Takeuchi, I. Tanihata, Y. Togano, C. Wu, Y. Yamaguchi, Y. Yanagisawa, A. Yoshida, and K. Yoshida. Low-lying excited states in $^{17,19}\text{C}$. *Phys. Lett B*, 614.
- [17] R. K. Gupta, S. Kumar, M. Balasubramaniam, G. Münzenberg, and W. Scheid. The cluster-core model for the halo structure of light nuclei at the drip lines. *J. Phys. G: Nucl. Part. Phys.*, 28:699–712, 2002.
- [18] J. C. Hardy and I. S. Towner. New Limits on Fundamental Weak-Interaction Parameters from Super-allowed β Decay. *Phys. Rev. Lett.*, 94:092502, 2005.
- [19] Q. Li, Y. Furusawa, M. Kanazawa, T. Kanai, A. Kitagawa, M. Aoki, E. Urakabe, S. Sato, and Z. Wei. Enhanced biological effect induced by a radioactive ^9C -ion beam at the depth around its Bragg peak. *Nucl. Instr. Meth. B*, 245:302–305, 2006.
- [20] S. Hojo, T. Honma, Y. Sakamoto, and S. Yamada. Production of ^{11}C -beam for particle therapy. *Nucl. Instr. Meth. B*, 240:75–78, 2005.

- [21] G. Audi, O. Bersillon, J. Blachot, and A. H. Wapstra. The NUBASE evaluation of nuclear and decay properties. *Nucl. Phys. A*, 729:3–128, 2003.
- [22] R.H. France III, Z. Zhao, and M. Gai. Absolute branching ratio of β -delayed γ -ray emission of ^{18}N . *Phys. Rev. C*, 68:057302, 2003.
- [23] G.C. Ball, W.G. Davies, J.S. Forster, H.R. Andrews, D. Horn, and W. McLatchie. The use of exotic heavy ion transfer reactions to study light neutron rich nuclei. *Nucl. Phys. A*, 32:305–316, 1979.
- [24] C. J. Densham, C. Thwaites, and J. R. J. Bennett. Critical parameters for the delay time of a RIB target. *Nucl. Instr. Meth. B*, 126:154–159, 1997.
- [25] G. J. Beyer, E. Hagebo, A. F. Novgorodov, H. L. Ravn, and the ISOLDE collaboration. The role of diffusion in ISOL targets for the production of radioactive ion beams. *Nucl. Instr. Meth. B*, 204:225–234, 2003.
- [26] R. Silverberg and C. H. Tsao. *Astrophys. J. Suppl. Series No.*, 25(220(I)), 1973.
- [27] K. Sümmerer, W. Bröchle, D. J. Morrissey, M. Schädel, B. Szweryn, and Y. Weifan. Target fragmentation of Au and Th by 2.6 GeV protons. *Phys. Rev. C*, 42(6):2546–2561, 1990.
- [28] I. Dostrovsky, R. Davis, A. M. Poskanzer, and P.L. Reeder. Cross sections for the production of Li^9 , C^{16} and N^{17} in irradiations with GeV-energy protons. *Phys. Rev.*, 139(6B):1513–1524, 1965.
- [29] I. Dostrovsky, H. Gauvin, and M. Lefort. (p,xp) and (p,xpy α) Reactions of 156-MeV Protons with light targets (A=11 to A=27). *Phys. Rev.*, 169(4):836–841, 1968.
- [30] J. B. Cumming, J. Hudis, A. M. Poskanzer, and S. Kaufman. $\text{Al}^{27}(\text{p},3\text{pn})\text{Na}^{24}/\text{C}^{12}(\text{p},\text{pn})\text{C}^{11}$ Cross-Section ratio in the GeV region. *Phys. Rev.*, 128(5), 1962.
- [31] U. Köster and the ISOLDE collaboration. Oxide fiber targets at ISOLDE. *Nucl. Instr. Meth. B*, 204:303–313, 2003.
- [32] G. Schaub, D. Unruh, J. Wang, and T. Turek. Kinetic analysis of selective catalytic NO_x reduction (SCR) in a catalytic filter. *Chem. Eng. Proc.*, 42, 2003.
- [33] I. Zvara. Thermochromatographic Method of Separation of Chemical Elements in nuclear and Radiochemistry. *Isotopenpraxis*, 26(6):251–258, 1990.
- [34] T. Bartel-Rausch, B. Eichler, P. Zimmermann, H W. Gäggeler, and M. Ammann. The adsorption enthalpy of nitrogen oxides on crystalline ice. *Atmos. Chem. Phys.*, 2:235–247, 2002.
- [35] A. Hohn, R. Eichler, and B. Eichler. Investigations on adsorption and transport behavior of carrier-free silver, gold and platinum in quartz columns under vacuum conditions. *Radiochimica Acta*, 92:513–516, 2004.

- [36] R. Eichler, B. Eichler, H.W. Gäggeler, D.T. Jost, R. Dressler, and A. Türlér. The Gas Phase Oxide and Oxyhydroxide Chemistry of Trace Amounts of Rhenium. *Radiochimica Acta*, 87:151–159, 1999.
- [37] G. Rudstam and B. Grapengiesser. Use of thermochromatography for rapid chemical separation. *Radiochimica Acta*, 20:97–107, 1973.
- [38] G. Gimond, A. Gizon, D. Barnérou, J. Blachot, J. Genevey, R. Guglielmini, J. Inchaouh, G. Margotton, and J. L. VieuxRochaz. Present status of singly charged ion ECR sources at the SARA on-line separator. *Nucl. Instr. Meth. B*, 70:118–124, 1992.
- [39] D. V. Filossofov, N. A. Lebedev, A. F. Novgorodov, G. D. Bontchev, and G. Y. Starodub. Production, concentration and deep purification of ^{111}In radiochemicals. *App. Rad. Isot.*, 55:293–295, 2001.
- [40] B. Eichler and I. Zvara. Evaluation of the Enthalpy of Adsorption from Thermochromatographical Data. *Radiochimica Acta*, 30:233–238, 1982.
- [41] I. Zvara. Simulation of thermochromatographic processes by the Monte Carlo method. *Radiochimica Acta*, 38(2):95–101, 1985.
- [42] M. Ammann. Using ^{13}N as tracer in heterogeneous atmospheric chemistry experiments. *Radiochimica Acta*, 89:831–838, 2001.
- [43] H. Kobayashi and M. Yamaguchi. Ab initio MO study of adsorption of CO molecule on TiO_2 surfaces. *Surface Science*, 214:466–476, 1989.
- [44] J. Li, L. Wu, and Y. Zhang. Theoretical study of adsorbed–decomposition of NO, CO and CH_2O on $\text{TiO}_2(110)(1 \times 1)$ defect surface. *Chem. Phys. Lett.*, 342:249–258, 2001.
- [45] J. Abad, O. Böhme, and E. Roman. Dissociative adsorption of NO on $\text{TiO}_2(110)$ argon ion bombarded surfaces. *Surface Science*, 549:134–142, 2004.
- [46] F. Boccuzzi, E. Guglielminotti, and G. Spoto. Vibrational and electronic effects of NO chemisorption on TiO_2 and Ru/TiO_2 . *Surface Science*, 251/252:1069–1074, 1991.
- [47] K. Mendelssohn. *Cryophysics*. Interscience Publishers Inc., 1960.
- [48] T. Bartel-Rausch, Thomas Huthwelker, Heinz W. Gäggeler, and M. Ammann. Atmospheric Pressure Coated-Wall Flow-Tube Study of Acetone Adsorption on Ice. *J. Phys. Chem. A*, 109:4531–4539, 2005.
- [49] D.D. Beck, J. M. White, and C.T. Ratcliffe. Catalytic Reduction of CO with Hydrogen Sulfide. 2 Adsorption of H_2O and H_2S on Anatase and Rutile. *J. Phys. Chem.*, 90:3123–3131, 1986.
- [50] D.D. Beck, J. M. White, and C.T. Ratcliffe. Catalytic Reduction of CO with Hydrogen Sulfide. 3 Study of Adsorption of O_2 , CO, and CO Coadsorbed with H_2S on Anatase and Rutile Using Auger Electron Spectroscopy and Temperature-Programmed Desorption. *J. Phys. Chem.*, 90:3132–3136, 1986.

- [51] W. Göpel, G. Rocker, and R. Feierabend. Intrinsic defects of $\text{TiO}_2(110)$: Interaction with chemisorbed O_2 , H_2 , CO and CO_2 . *Phys. Rev. B*, 29:3427–3438, 1983.
- [52] G.B. Raupp and J.A. Dumesic. Adsorption of CO , CO_2 , H_2 , and H_2O on titania surfaces with different oxidation states. *J. Phys. Chem.*, 89:5240–5246, 1985.
- [53] A. Auroux and Gervasini A. Microcalorimetric study of the acidity and basicity of metal oxide surfaces. *J. Phys. Chem.*, 94:6371–6379, 1990.
- [54] J. A. Rodriguez, T. Jirsak, G. Liu, J. Hrbek, J. Dvorak, and A. Maiti. Chemistry of NO_2 on oxide surfaces: Formation of NO_3 on $\text{TiO}_2(110)$ and $\text{NO}_2 \leftrightarrow \text{O}$ vacancy interactions. *J. Am. Chem. Soc.*, 123:9597–9605, 2001.
- [55] D. C. Sorescu and Jr. J. T. Yates. Adsorption of CO on the $\text{TiO}_2(110)$ surface: A theoretical study. *J. Phys. Chem. B*, 102:4556–4565, 1998.
- [56] J. Ahdjoudj, A. Markovits, and C. Minot. Hartree-Fock periodic study of the chemisorption of small molecules on TiO_2 and MgO surfaces. *Catalysis Today*, 50:541–551, 1999.
- [57] P. A. Redhead. Thermal desorption of gases. *Vacuum*, 12:203–211, 1963.
- [58] David A. King. Thermal desorption from metal surfaces: a review. *Surface Science*, 47:384–402, 1975.
- [59] H. Frånberg, M. Ammann, H. W. Gäggeler, and U. Köster. Chemical investigations of isotope separation on line target units for carbon and nitrogen beams. *Rev. Sci. Instrum.*, 77:03A708, 2006.
- [60] C. Ronchi and M. Sheindlin. Melting point of mgo. *J. Appl. Phys.*, 90:3325, 2001.
- [61] K. Tanabe and Y. Fukuda. Basic properties of alkaline earth metal oxides and their catalytic activity in the decomposition of diacetone alcohol. *Reac. Kin. Cat. Lett.*, 1(1):21–24, 1974.
- [62] R. Geller. Electron cyclotron resonance sources: Historical review and future prospects. *Rev. Sci. Instrum.*, 69:1302–1310, 1998.
- [63] Z. Xie, C. M. Lyneis, R. S. Lam, and S. Lundgren. Enhanced ECR ion source performance with an electron gun. *Rev. Sci. Instrum.*, 62:775–778, 1991.
- [64] T. Nakagawa, T. Kageyama, M. Kase, A. Goto, and Y. Yano. Upgrade of RIKEN 10 GHz Electron Cyclotron Resonance Ion Source Using Plasma Cathode Method. *Jap. J. Appl. Phys.*, 32:1335–1338, 1993.
- [65] L. Schächter, K. E. Siebing, S. Dobrescu, Al. I. Badescu-Singureanu, S. Runkel, O. Hohn, L. Schmidt, A. Schempp, and H. Schmidt-Böcking. Influence of the secondary electrons emitted by a cylindrical metaldielectric structure on the Frankfurt 14 GHz electron cyclotron resonance ion source performances. *Rev. Sci. Instrum.*, 71, 2000.

- [66] G.M. Underwood and T.M. Miller. Transmission FT-IR and Knudsen Cell Study of the Heterogeneous Reactivity of Gaseous Nitrogen Dioxide on Mineral Oxide Particles. *J. Phys. Chem. A*, 103:6184–6190, 1999.
- [67] A. Zecchina, E. Escalona Platero, and C. Otero Areán. Low temperature CO adsorption on alum-derived active alumina: An infrared investigation. *J. Catal*, 107(1):244–247, 1987.
- [68] M. Casarin, D. Falcomer, A. Glisenti, and A. Vittadini. Experimental and Theoretical Study of the Interaction of CO₂ with alpha-Al₂O₃. *Inorg. Chem.*, 42:436–445, 2003.
- [69] C. Pazé, G. Gubitosa, S. Orso Giaccone, G. Spoto, F.X. Llabrés i Xamena, and A. Zecchina. An XRD, FTIR and TPD investigation of NO₂ surface adsorption sites of delta, gamma Al₂O₃ and barium supported delta, gamma Al₂O₃. *Top. Cat.*, 30/31:169–175, 2004.
- [70] K. Sümmerer and B. Blank. Modified empirical parametrization of fragmentation cross sections. *Phys. Rev. C*, 61:034607, 2000.
- [71] J. Lettry, R. Catherall, P. Drumm, P. Van Duppen, A. H. M. Evensen, G. J. Focker, A. Jokinen, O. C. Jonsson, E. Kugler, H. Ravn, and ISOLDE Collaboration. Pulse shape of the ISOLDE radioactive ion beams. *Nucl. Instr. Meth. B*, 126:130–134, 1997.
- [72] T. Björnstad, E. Hagebo, P. Hoff, O. C. Jonsson, E. Kugler, H. L. Ravn, S. Sundell, B. Vosicki, and ISOLDE collaboration. Methods for Production of Intense Beams of Unstable Nuclei: New Developments at ISOLDE. *Phys. Scr.*, 34:578–590, 1986.
- [73] L. C. Carraz, I. R. Haldorsen, H. L. Ravn, M. Skarestad, and L. Westgaard. Fast release of nuclear reaction products from refractory matrices. *Nucl. Instr. Meth.*, 148:217–230, 1978.
- [74] L. C. Carraz, H. L. Ravn, M. Skarestad, S. Sundell, and L. Westgaard. Fast release of nuclear reaction products from refractory matrices. *Nucl. Instr. Meth.*, 148:217–230, 1978.
- [75] P. Hoff, O. C. Jonsson, E. Kugler, and H. L. Ravn. Release of nuclear reaction products from refractory compounds. *Nucl. Instr. and Meth.*, 221:313–329, 1984.
- [76] S. Sundell, H. Ravn, and the ISOLDE Collaboration. Ion source with combined cathode and transfer line heating. *Nucl. Instr. Meth. B*, 70:160–164, 1992.
- [77] K. Peräjärvi, U. C. Bergmann, V. N. Fedoseyev, A. Joinet, U. Köster, C. Lau, J. Lettry, H. Ravn, M. Santana-Leitner, and The Isolde Collaboration. Studies of release properties of ISOLDE targets. *Nucl. Instr. Meth. B*, 204:272–277, 2003.
- [78] Z. Zhao, M. Gai, B.J. Lund, S.L. Rugari, D. Mikolas, B.A. Brown, J.A. Nolen Jr., and M. Samuel. Beta decay of ¹⁸N to alpha particle emitting states in ¹⁸O and a proposed search for parity violation in ¹⁸O. *Phys. Rev. C*, 39(5):1985–1991, 1989.

- [79] J.L. Lou, Z.H. Li, Y.L. Ye, H. Hua, D.X. Jiang, L.H. Lv, Z. Kong, Y.M. Zhang, F.R. Xu, T. Zheng, X.Q. Li, Y.C. Ge, C. Wu, G.L. Zhang, Z.Q. Chen, C. Li, D.Y. Pang, H.S. Xu, Z.Y. Sun, L.M. Duan, Z.G. Hu, R.J. Hu, H.G. Xu, R.S. Mao, Y. Wang, X.H. Yuan, H. Gao, L.J. Wu, H.R. Qi, T.H. Huang, F. Fu, F. Jia, Q. Gao, X.L. Ding, J.L. Han, and X.Y. Zhang. Observation of a new transition in the β -delayed neutron decay of ^{18}N . *Phys. Rev. C*, 75:057302, 2007.
- [80] L. Buchmann, J. D'Auria, M. Dombisky, U. Giesen, K. P. Jackson, P. McNeely, J. Powell, and A. Volya. β -delayed α emission of ^{18}N : Broad $J^\pi = 1^-$ states in the $^{14}\text{C} + \alpha$ system. *Phys. Rev. C*, 75:012804(R), 2007.
- [81] F. Durantel. R04 02. Master's thesis, CNAM, GANIL, 2004.
- [82] P. Jardin, C. Barue, C. Canet, M. Dupuis, J.-L. Flambart, G. Gaubert, N. Lecesne, P. Leherissier, F. Lemagnen, R. Leroy, J. Y. Pacquet, F. Pellemoine, J.-P. Rataud, M.G. Saint Laurent, and A. C. C. Villari. Mono 1000: A simple and efficient 2.45 GHz electron cyclotron resonance ion source using a new magnetic structure concept. *Rev. Sci. Instrum.*, 73(2):789–791, 2002.
- [83] M. Santana Leitner. *A Monte Carlo code to optimize the production of radioactive ion beams by the ISOL technique*. PhD thesis, Technical University of Catalonia, 2005. CERN-THESIS-2005-049.
- [84] L. M. Brescansin, J. R. Leite, and L. G. Ferreira. A study of the ground states and ionization energies of H_2 , C_2 , N_2 , F_2 and CO molecules by the variational cellular method. *J. Chem. Phys.*, 71(12):4923–4930, 1979.
- [85] W. E. Moddeman, T. A. Carlsson, M. O. Krause, and B. P. Pullen. Determination of the K-LL Auger Spectra of N_2 , O_2 , CO , NO , H_2O , CO_2 . *J. Chem. Phys.*, 55(5):2317–2336, 1971.
- [86] V.I. Mishin, V. N. Fedoseyev, H.-J. Kluge, V. S. Letokhov, H. L. Ravn, F. Scheerer, Y. Shirakabe, S. Sundell, O. Tengblad, and the ISOLDE Collaboration. Chemically selective laser ion-source for the CERN-ISOLDE on-line mass separator facility. *Nucl. Instr. Meth. B*, 73:550–560, 1993.
- [87] V. N. Fedoseyev, G. Huber, U. Köster, J. Lettry, V. I. Mishin, H. Ravn, V. Sebastian, and the ISOLDE Collaboration. The ISOLDE laser ion source for exotic nuclei. *Hyperfine Interactions*, 127:409–416, 2000.
- [88] U. Köster, V. N. Fedoseyev, A. N. Andreyev, U. C. Bergmann, R. Catherall, J. Cederkäll, M. Dietrich, H. De Witte, D. V. Fedorov, L. Fraile, S. Franchoo, H. Fynbo, U. Georg, T. Giles, M. Gorska, M. Hannawald, M. Huyse, A. Joinet, O. C. Jonsson, K. L. Kratz, K. Krugolov, Ch. Lau, J. Lettry, V. I. Mishin, M. Oinonen, K. Partes, K. Peräjärvi, B. Pfeiffer, H. L. Ravn, M. D. Seliverstov, P. Thierolf, K. Van der Vel, P. Van Duppen, J. Van Roosboeck, I. Weissman, IS365, IS387, IS393, and the ISOLDE collaboration. On-line yields obtained with the ISOLDE RILIS. *Nucl. Instr. Meth. B*, 204:347–352, 2003.

BIBLIOGRAPHY

- [89] V. N. Fedoseyev, D. V. Fedorov, R. Horn, G. Huber, U. Köster, J. Lassen, V. I. Mishin, M. D. Seliverstov, L. Weissman, K. Wendt, and the ISOLDE Collaboration. Atomic spectroscopy studies of short-lived isotopes and nuclear isomer separation with the ISOLDE RILIS. *Nucl. Instr. Meth. B*, 204:353–358, 2003.
- [90] V. N. Fedoseyev, B. A. Marsh, D. V. Fedorov, U. Köster, and E. Tengborn. Ionization Scheme Development at the ISOLDE RILIS. *Hyperfine Interactions*, 162(1–4):15–27, 2005.
- [91] R. Kirchner. On the thermoionization in hot cavities. *Nucl. Instr. Meth. A*, 292:203–208, 1990.
- [92] R. Kirchner. Progress in ion source development for on-line separators. *Nucl. Instr. Meth.*, 186:275–293, 1981.
- [93] P. Jardin, W. Farabolini, G. Gaubert, J. Y. Pacquet, T. Drobert, J. Cornell, C. Barue, C. Canet, M. Dupuis, J.-L. Flambart, N. Lecesne, P. Leherissier, F. Lemagnen, and R. Leroy. Optimization of ECR singly-charged ion source for the radioactive ion beam production. *Nucl. Instr. Meth. B*, 204:377–381, 2003.
- [94] G. Gaubert, C. Baru, C. Canet, J. Cornell, M. Dupuis, W. Farabolini, J. L. Flambard, P. Gorel, P. Jardin, N. Lecesne, P. Leherissier, F. Lamagnen, R. Leroy, J. Y. Pacquet, M. G. Saint-Laurent, and A. C. C. Villari. Minimono: An ultracompact permanent magnet ion source for singly charged ions. *Rev. Sci. Instrum.*, 74(2):956–960, 2003.
- [95] F. Wenander, W. Farabolini, G. Gaubert, P. Jardin, and J. Lettry. First ECR-ionized noble gas radioisotopes at ISOLDE. *Nucl. Phys. A*, 746:659c–662c, 2004.
- [96] T. Lamy, J.L. Bouly, J.C. Curdy, R. Geller, A. Lacoste, P. Sole, P. Sortais ad T. Thuillier, J.L. Vieux-Rochaz, K. Jayamanna, M. Olivo, P. Schmor, and D. Yuan. Charge state breeding applications with the ECR PHOENIX source: From low to high current production. *Rev. Sci. Instrum.*, 73:717–719, 2002.
- [97] T. Fritioff, J. Cederkäll, L. Weissman, C.J. Barton, K.A. Connell, D. Duniec, O. Kester, T. Lamy, T. Nilsson, P. Jardin, P Sortais, and G. Tranströmer. Purification of radioactive neutron-rich argon beams using an ion source in charge breeding mode. *Nucl. Instr. Meth. A*, 556:31–37, 2006.
- [98] A. G. Drentje. Techniques and mechanisms applied in electron cyclotron resonance sources for highly charged ions. *Rev. Sci. Instrum.*, 74(5), 2003.
- [99] K. W. Scheller, J. Görres, S. Vouzoukas, M. Wiescher, B. Pfeiffer, K.L. Kratz, D. J. Morrissey, B. M. Scherrill, M. Steiner, M. Hellström, and J. A. Winger. Study of the β -delayed neutron decay of ^{17}C and ^{18}C . *Nucl. Phys. A*, 582, 1995.

Curriculum Vitae

Personal Information

Name Hanna Frånberg
Citizenship Swedish
Date of Birth 24.07.1978
Place of Birth Sweden

Education

Mar 2003 – Mar 2007 50 % doctoral student contract with the Paul Scherrer Institute, Villigen
Oct 2003 – Dec 2006 50 % doctoral student contract with CERN.
Aug 1998 – Dec 2002 Master of Science Arts, Göteborgs Universitet, Sweden. Main field: Physics.
Aug 1994 – Jun 1997 Wargentin Secondary school, Östersund, Sweden of technical/nature science. Specialization: Computer science.

Professional Experience

Jan 2007 – Nov 2008 Fellow contract with the Accelerator and Beam department at CERN. In the Operational group of ISOLDE.
2004 – 2005 Assistant lecturer during radiochemistry practicum. University of Bern, Switzerland.
Jun 2002 – Sep. 2002 Summer student at ISOLDE, CERN, Geneva, Switzerland.
Aug 2000 – May 2001 Supply teacher in physics, chemistry, mathematics, French and English for ages 13-15. Angered, Sweden.
Sep 1997 – Jun 1998 Voluntary work at convent of Dominiquaine des Tourelles, St. Genis des Tréviars, France.
Jun 1996 – Sep 2001 (June to September every summer). Hostel manager at STF youth hostel in Östersund, Sweden. Task: Economy, planning, employer.

List of Publications

1. Volatile Elements Production Rates in a 1.4 GeV Proton-Irradiated Molten Lead-Bismuth Target. *AIP Conf. Proc.:* 769 (2005) pp.1525-1528. L. Zanini, M. Andersson, P. Everaerts, M. Fallot, H. Frånberg, F. Gröschel, C. Jost, T. Kirchner, Y. Kojima, U. Köster, J. Lebenhaft, E. Manfrin, E. Pitcher, H. Ravn, Y. Tall, W. Wagner, M. Wohlmuther
2. Chemical Investigations of ISOL target units for carbon and nitrogen beams. *Rev. Sci. Instrum.:* 77(2006) H. Frånberg, M. Ammann, H.W. Gäggeler, U. Köster.
3. (Im)-possible ISOL beams. *Eur. Phys. J. Special Topics* 150, 285-291 (2007) U. Köster, P. Carbonez, A. Dorsival, J. Dvorak, R. Eichler, S. Fernandes, H. Frånberg, J. Neuhausen, Z. Novackova, R. Wilfinger, and A. Yakushev
4. Off-line commissioning and installation of ISCOOL at ISOLDE. *Nucl. Instr. Meth. B. In press* H. Frånberg, P. Delahaye, J. Billowes, K. Blaum, R. Catherall, F. Duval, O. Gianfrancesco, T. Giles, A. Jokinen, e, M. Lindroos, D. Lunney, E. Mane and I. Podadera
5. Progress in ISOL target^Uion source systems. *Nucl. Instr. Meth. B. In press* U. Köster, O. Arndt, E. Bouquerel, V.N. Fedoseyev, H. Frånberg, A. Joinet, C. Jost, I.S.K. Kerkinen, R. Kirchner, The TARGISOL Collaboration
6. Measurement of the Ar diffusion coefficient in graphite at high temperature by the ISOL method *Nucl. Instr. Meth. B. In press* C. Eléon, P. Jardin, J.C. Thomas, M.G. Saint-Laurent, C. Huet-Equilbec, R. Alvès-Condé, J.C. Angélique, D. Boilley, J. Cornell, M. Dubois, H. Frånberg, G. Gaubert, B. Jacquot, U. Köster, R. Leroy, L. Mournoury, N. Orr, J.Y. Pacquet, F. Pellemoine, C. Stodel, M. Turrion
7. Thermo chromatography investigations of TiO₂ surfaces. *Radiochimica Acta* H. Frånberg, et al., under preparation.